

Study of X-ray emission from nearby normal galaxies using eROSITA All-Sky Survey data

Master's Thesis in Physics and Astronomy

Vorgelegt von
Roman Laktionov
21. Februar 2024

Astronomisches Institut Dr. Karl Remeis-Sternwarte
Friedrich-Alexander-Universität Erlangen-Nürnberg



Supervisor: Prof. Dr. Manami Sasaki

Abstract

Normal galaxies are the main sites of star formation in the Universe. Diffuse X-ray emission, produced in superbubbles of hot, ionized gas, plays a key role in the study of star formation history and the evolution of galaxies. The recently launched eROSITA mission (extended ROentgen Survey with an Imaging Telescope Array) aims to conduct the most detailed X-ray All-Sky Survey to date. Due to its high sensitivity in the soft X-ray band, it provides the perfect instrument for studies of the diffuse X-ray emission from the hot phase interstellar medium (ISM).

Within this work, *A Catalog of Neighboring Galaxies*, presented by Karachentsev et al., 2013, was used to acquire the coordinates and properties of 869 galaxies in our local Universe. From this data, a sample of 72 galaxies has been selected and sorted into groups of high, medium and low star formation rates (SFRs). An eROSITA X-ray image catalog, displayed in chapter 8, visualizes the diffuse X-ray emission and point sources within the galaxies. Spectra were extracted with SRCTOOL after the exclusion of point sources with an eROSITA source detection algorithm. The X-ray emission of the galaxies NGC 5128, NGC 5236, NGC 6744, NGC 1291, NGC 300, NGC 1313, NGC 4594, NGC 4945, NGC 4826 and NGC 5068 has been successfully modelled in Xspec with a five-component background model and a VNEI source component for three values of the ionization timescale $\tau = 10^{11}, 10^{12}, 10^{13} \text{ s cm}^{-2}$. The results are more consistent and better constrained for $\tau = 10^{12}, 10^{13} \text{ s cm}^{-2}$, indicating that the gas is in collisional ionization equilibrium. 8 out of 10 galaxies exhibit a cooler, diffuse component at plasma temperatures of $\sim 0.2 - 0.3 \text{ keV}$, whereas NGC 1291 and NGC 4945 contain a hotter plasma component at temperatures of 0.47 keV and 0.63 keV. For the remaining galaxies, the spectra had to be stacked due to low photon statistics. As a result, we acquired average spectra for the high, medium and low SFR galaxies. The spectra were used to determine the X-ray luminosities L_X of the diffuse gas. Furthermore, L_X/SFR scaling factors have been derived and compared to the literature.

Contents

List of Figures	III
List of Tables	V
1 Introduction	1
2 Galaxies	3
2.1 Formation	3
2.2 Types of Galaxies	3
2.3 Star Formation	7
3 X-ray Sources and Observations	9
3.1 X-ray Observations of Galaxies	9
3.2 X-ray Point Sources	10
3.3 Diffuse X-ray Emission	12
3.4 N_{H} map	15
4 The eROSITA Mission	16
5 Source Selection	19
5.1 The Nearby Galaxy Catalog	19
5.2 The eROSITA Pipeline	19
5.3 List of Parameters	20
5.4 X-ray and Optical Images	24
6 Analysis of eROSITA Data	27
6.1 Extracting Spectra	27
6.2 Background Model	27
6.3 Source Model	31
6.4 Spectral Analysis	33
6.5 Single Spectra	35
6.6 Star Formation Rates	58
6.7 The Ionization Timescale	61
6.8 Stacked Spectra	62
6.9 Properties and Distribution of Galaxies	67
6.10 Fluxes and Luminosities	69
6.11 $L_{\text{X}} - \text{SFR}$ Relation	74
7 Summary and Conclusion	77
8 Appendix	79
Bibliography	88

List of Figures

2.1	Galaxy morphology diagram.	3
2.2	Images of the Whirlpool galaxy and NGC 1672.	4
2.3	Composite image of Centaurus A.	5
2.4	Optical image of IC 1101.	7
3.1	Chandra ACIS X-ray image of Messier 83.	9
3.2	Illustrations of LMXBs.	11
4.1	The eROSITA X-ray telescope.	16
4.2	eROSITA sky map.	17
4.3	German and Russian side of the eROSITA sky.	18
5.1	X-ray and optical images of NGC 55.	24
6.1	Schematic of the emission components towards the eFEDS field.	28
6.2	The diffuse emission observed by eROSITA in the eFEDS field.	30
6.3	X-ray and optical images of NGC 5128.	36
6.4	X-ray spectrum of NGC 5128.	37
6.5	X-ray and optical images of NGC 5236.	38
6.6	X-ray spectrum of NGC 5236.	39
6.7	X-ray and optical images of NGC 6744.	40
6.8	X-ray spectrum of NGC 6744.	41
6.9	X-ray and optical images of NGC 1291.	42
6.10	X-ray spectrum of NGC 1291.	43
6.11	X-ray and optical images of NGC 300.	45
6.12	X-ray spectrum of NGC 300.	46
6.13	X-ray and optical images of NGC 1313.	47
6.14	X-ray spectrum of NGC 1313.	48
6.15	X-ray and optical images of NGC 4594.	49
6.16	X-ray spectrum of NGC 4594.	50
6.17	X-ray and optical images of NGC 4945.	51
6.18	X-ray spectrum of NGC 4945.	52
6.19	X-ray and optical images of NGC 4826.	54
6.20	X-ray spectrum of NGC 4826.	55
6.21	X-ray and optical images of NGC 5068.	56
6.22	X-ray spectrum of NGC 5068.	57
6.23	kT over SFR plot.	61
6.24	Stacked X-ray spectrum of high SFR galaxies.	64
6.25	Stacked X-ray spectrum of medium SFR galaxies.	66
6.26	Stacked X-ray spectrum of low SFR galaxies.	66
6.27	SFR over distance plot.	67
6.28	Counts over distance plot.	67

6.29	Mass over distance plot.	68
6.30	Diameter over distance plot.	68
6.31	SFR/ M over distance plot.	68
6.32	SFR over mass plot.	68
6.33	High SFR particle background.	70
6.34	Medium SFR particle background.	70
6.35	Low SFR particle background.	70
6.36	Total flux over distance plot.	72
6.37	Total luminosity over distance plot.	72
6.38	High SFR VNEI component.	73
6.39	Medium SFR VNEI component.	73
6.40	Low SFR VNEI component.	73
6.41	VNEI flux over distance plot.	74
6.42	VNEI luminosity over distance plot.	74
6.43	Total luminosity over SFR plot.	75
6.44	VNEI luminosity over SFR plot.	75

List of Tables

5.1	X-ray energy bands.	20
5.2	Galaxy parameter list for luminous galaxies.	21
5.3	Galaxy parameter list for diffuse galaxies.. . . .	23
6.1	Fit parameters of NGC 5128, NGC 5236, NGC 6744, NGC 1291, NGC 300, NGC 1313, NGC 4594, NGC 4945, NGC 4826 and NGC 5068. . . .	35
6.2	Galaxy SFR grouping.	58
6.3	Data of high SFR galaxies.	59
6.4	Data of medium SFR galaxies.	59
6.5	Data of low SFR galaxies.	60
6.6	kT results for different ionization timescales.	62
6.7	Fit parameters for stacked spectra.	65
6.8	Fluxes of NGC 5128, NGC 5236, NGC 6744, NGC 1291, NGC 300, NGC 1313, NGC 4594, NGC 4945, NGC 4826 and NGC 5068.	69
6.9	Fluxes of stacked spectra.	71

1 Introduction

Diffuse X-ray emission originates from hot, thermal plasma at temperatures of $T \sim 10^6 - 10^7$ K. In star-forming galaxies, the ISM is heated via shock waves that are produced by massive stars. The combined effects of stellar winds and supernova explosions can lead to the formation of giant supershells that contain hot, ionized gas with particle densities of $n < 0.01 \text{ cm}^{-3}$. The presence of supershells is indicative for an abundance of massive stars, which point towards recent star-forming activity due to their short lifespan. Since stars are responsible for the enrichment and distribution of heavy elements, understanding the interplay of star formation with the ISM plays a key role for the understanding of galactic evolution.

Star formation mainly takes place along the spiral arms of young galaxies, where the abundance of cold, molecular gas is the highest. It eventually ceases, when all star-forming gas is exhausted. The accretion of matter through tidal interactions with satellite galaxies can replenish the supply of cold gas and re-ignite star-forming activity. A merger event can disrupt the galaxy's morphology by heating and dispersing the gas, possibly producing complex and unique structures. Often, intense starbursts are initiated with SFRs reaching up to $\sim 10^3 M_{\odot} \text{ yr}^{-1}$. In some galaxies, gas is heated via feedback from the active galactic nucleus (AGN). Galactic cores often contain X-ray point sources, as the high stellar density in the bulge provides favorable conditions for the formation of X-ray binaries; mostly binary systems composed of a Main Sequence star and a neutron star.

While cooling, the gas will persist in the galaxy for millions of years and produce diffuse X-ray emission, predominantly in the soft 0.3 – 1 keV energy band. By studying the diffuse X-ray emission of galaxies, we can determine the distribution and characteristics of the hot, ionized gas, shedding light on the galaxy's star formation history and evolution.

A Catalog of Neighboring Galaxies is an all-sky catalog of 869 galaxies with distance estimates up to ~ 17 Mpc, providing parameters such as the coordinates, sizes and masses. A sample of 72 galaxies has been selected from this catalog for a study of diffuse X-ray emission, as seen with the eROSITA telescope.

With the mission to conduct the most detailed X-ray All-Sky Survey to date, eROSITA completed 4 scans of the X-ray sky (eRASS1 - eRASS4) since its launch in 2019. The telescope is highly sensitive in the $\sim 0.2 - 8$ keV energy range, making it the perfect instrument to capture diffuse X-ray emission in nearby galaxies. However, the eROSITA photon statistics drastically worsen with increasing distance to an extended source. From the selected sample, 10 galaxies at distances $d < 9.3$ Mpc produced sufficient X-ray emission for a spectral analysis. By analyzing the spectra of the diffuse gas, we can constrain physical parameters such as the plasma temperature and the ionization timescale. Moreover, in the X-ray images taken with eROSITA, we can inspect the hot gas distribution within the galaxies. An RGB X-ray image catalog has been created from the eRASS1 - eRASS4 surveys (see chapter 8), showing emission in the high, medium and soft X-ray bands.

Emission in these energy ranges is highly contaminated by the local X-ray background. Hot gas within the Milky Way, e.g. the circum-Galactic medium and the Galactic corona, produce their own diffuse X-ray emission. The Sun expels hot plasma and charged particles into the surroundings, which interact with the ISM. Unresolved point-sources from

the cosmic X-ray background further contribute to the spectrum. In order to analyze the X-ray emission of nearby galaxies, these effects need to be corrected. They can be taken into account by implementing a realistic model for the background emission.

In addition, the soft X-ray spectrum is strongly affected by photoelectric absorption through baryonic particles in the ISM of our galaxy. In 2016, The HI4PI Collaboration (HI4PI, 2016) published the HI4PI survey, which quantifies the total number of H I hydrogen atoms in the vicinity of the Milky Way. These H I maps are used throughout the spectral analysis to correct the spectra for Galactic absorption.

A spectral analysis has been conducted for the galaxies NGC 5128, NGC 5236, NGC 6744, NGC 1291, NGC 300, NGC 1313, NGC 4594, NGC 4945, NGC 4826 and NGC 5068. Although the remaining galaxies are too faint for a spectral analysis on their own, their counts will be stacked in order to acquire average spectra for the high, medium and low-SFR galaxies.

Mineo et al., 2014, found a linear $L_X - \text{SFR}$ relation for galaxies. To check whether this is in agreement with the eROSITA data, we will determine the X-ray luminosities L_X of the selected galaxies.

2 Galaxies

2.1 Formation

Galaxy formation is a hierarchical process, initiated by the collapse of gravitationally unstable regions in the early Universe. Shortly after the Big Bang, cosmic inflation stretched quantum fluctuations to macroscopic scales, creating over-densities in the dark matter distribution; now observable via the Cosmic Microwave Background Radiation. These over-densities lead to the formation of dark matter minihalos, which then accumulated baryons and collected to filaments. Matter moving along those filaments, e.g. clouds of gas and dark matter, is accreted and mixed with the rest of the ISM. This accretion flow provides cold gas, which effectively fuels star formation and drives the growth of the galaxy. The second accretion mode is comprised of tidal interactions and major mergers with other galaxies, providing a source of hot gas that will eventually contribute to star formation after it has cooled. While accretion flow drives star formation and galaxy growth at a relatively steady rate, mergers are rare and have the potential to initiate a starburst with a considerably higher SFR (Silk et al., 2013).

2.2 Types of Galaxies

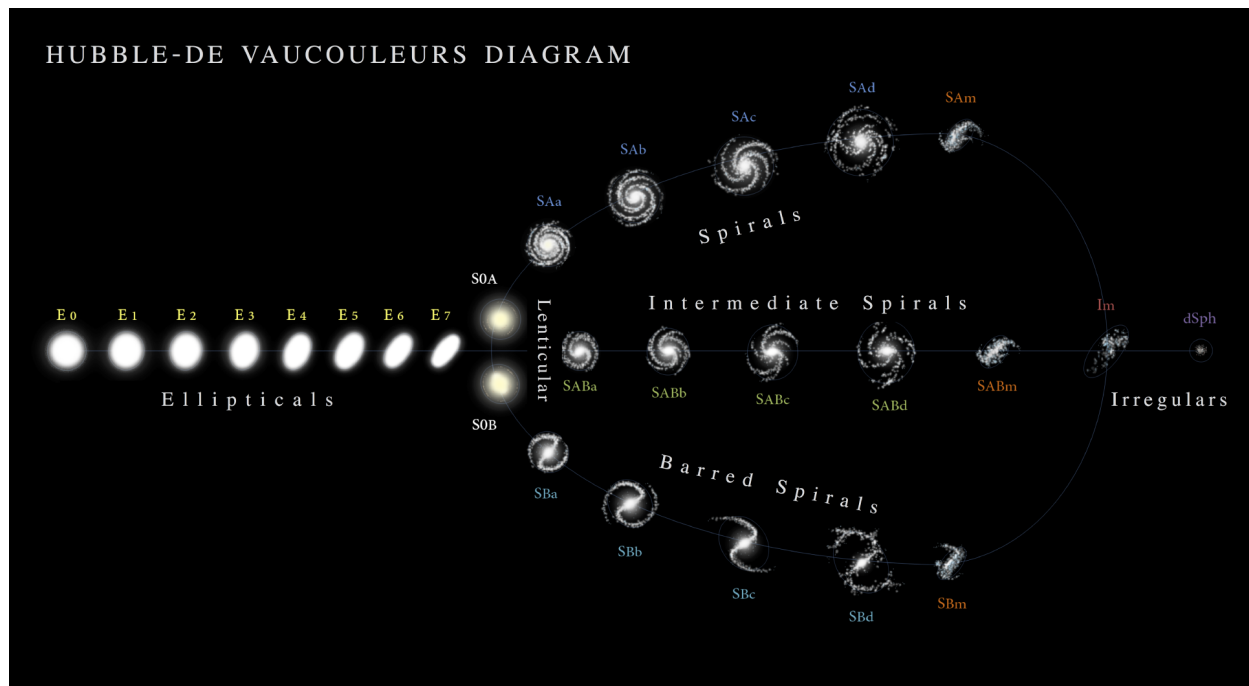


Fig. 2.1: The Hubble - de Vaucouleurs galaxy morphology diagram. It features barred and unbarred spirals, lenticulars, ellipticals and irregular galaxies (Ciccolella, 2011).

Galaxies are complex systems with numerous components and a large variety of morphologies. Formation histories are shaped by past mergers and interactions, equipping galaxies with unique features such as rings and bars, or possibly a lack of structure altogether. Depending on the type, history and age, they can have vastly different sizes, masses and chemical compositions (Kiar et al., 2017). It was therefore necessary to establish a method of classification for different types and evolutionary stages of galaxies. This was first done by Hubble, 1926, who categorized "extra-galactic nebulae" into two main groups based on their morphological characteristics: spiral galaxies with a significant disc component (late-type) and elliptical galaxies with a dominant bulge component (early-type). The spiral galaxies are further distinguished into barred and unbarred systems. Galaxies, which don't fit into either category, are considered to be irregular galaxies. This so-called "Hubble Sequence" further arranges the galaxies into intermediate types between spiral and elliptical galaxies, which can be interpreted as different evolutionary stages. The structural and intrinsic properties of galaxies undergo significant evolution during their lifetime. Across cosmic timescales, galaxies typically evolve from small but luminous, star-forming spirals to large but diffuse, depleted ellipticals. The transition from a spiral to an elliptical galaxy is induced when two spiral galaxies merge, disrupting their disc structure and generating a spherical shape. The Hubble Sequence was later extended by Vaucouleurs, 1959, who added important features of spiral galaxies such as half-bars, rings and lenses. The Hubble - de Vaucouleurs galaxy morphology diagram is displayed in Figure 2.1.

In the following, the different types of galaxies will be explored in more detail.

Spiral Galaxies

Spiral galaxies are made up of three main components:

- a flat and rotating disc, rich in stars, gas and dust,
- the bulge, a spherical concentration of stars in the center,
- the halo, a spherical low-density environment surrounding the disc.



Fig. 2.2: Left side: Optical image of the Whirlpool galaxy (Type SAbc; Beckwith et al., 2005). Right side: Optical image of NGC 1672 (Type SBbc; NASA/ESA, 2007). Both images were taken with the Hubble Space Telescope.

The galactic disc is relatively thin (e.g. 1.35 kpc for the Milky Way; Rix et al., 2013) and displays an eye-catching structure of spiral arms. Galactic discs are believed to have formed due to the conservation of angular momentum associated with collapsing gas clouds in dark matter halos (Silk et al., 2013). The material in the disc exhibits circular orbits around the central bulge. The spiral arms are overdensities of stars, gas and dust, as predicted by the density wave theory, and are much brighter than the inter-arm regions. This is a result of high star-forming activity in the spiral arms and consequently, a higher concentration of luminous OB stars (Silva-Villa et al., 2012b, and references therein). Moreover, many spiral galaxies exhibit a bar-like structure that connects the central bulge to the spiral arms. In the Hubble Sequence, they are therefore divided into barred (Type SB), unbarred (Type SA), and intermediate (Type SAB) spiral galaxies. Figure 2.2 displays an optical image of the unbarred Whirlpool galaxy (Type SAbc, left side) and an optical image of the barred NGC 1672 galaxy (Type SBbc, right side), both taken with the Hubble Space Telescope. Further classification was established based on the angle of the spiral arms and the brightness of the bulge. Young spiral galaxies (Type Sd and Sc) exhibit a small, faint bulge and loosely wound arms. As a consequence of long-lasting evolution and accretion of matter, the bulge becomes larger and brighter, while the arms become more tightly wound (Type Sb and Sa). So-called Magellanic spirals (Type SAm and SBm) are spiral galaxies resembling the Large Magellanic Cloud, a satellite galaxy of the Milky Way, with only one spiral arm.



Fig. 2.3: Composite image of Centaurus A, taken with LABOCA on APEX (submillimetre wavelengths, in orange), the Chandra X-ray Observatory (blue) and the Wide Field Imager on the MPG/ESO 2.2 m telescope (optical wavelengths, in true color). Credit: ESO/WFI (Optical); MPIfR/ESO/APEX/A.Weiss et al. (Submillimetre); NASA/CXC/CfA/R.Kraft et al. (X-ray; ESO-Images, 2009).

Although the stellar population in the disc contains young, blue stars, this is typically not the case for the bulge. Chemical abundance studies of the Milky Way have shown that halo and bulge stars are relatively old and metal-poor (e.g. Fulbright, 2000). In addition,

many bulges are believed to host supermassive black holes, some of which are categorized as AGNs.

AGNs have been observed to emit large amounts of energy from radio wavelengths up to gamma rays. This emission is not of stellar origin, and instead is produced by an ongoing accretion of matter onto the central supermassive black hole. AGNs have been categorized into many subclasses, with the most common one being the Seyfert 2 AGN, characterized by strong, highly ionized emission lines. Some AGNs produce feedback, e.g. in the form of jets, which can lead to very complex structures within the galaxy. One example of an active galaxy with jets is Centaurus A (see Figure 2.3). It will be part of our analysis later on (in section 6.5).

The galactic halo extends much further into space. However, it has a significantly lower density than the galactic plane and is therefore very faint. It is made up of three components:

- the stellar halo,
- the galactic corona,
- the dark matter halo.

The stellar halo contains old, metal-poor stars that have drifted away from the disc (e.g. through tidal interactions), but are still gravitationally bound to the galaxy. Furthermore, it is the natural habitat of globular clusters (GCs), spherical conglomerations of up to $\sim 10^6$ stars. A study of the X-ray emission of the Milky Way's GC population, as seen with the eROSITA telescope, has been conducted in a previous thesis (Laktionov, 2021).

The galactic corona contains all gas that is still gravitationally bound to the galaxy, and resembles an important component of the local X-ray background, which will be discussed in section 6.2. The dark matter halo extends far beyond the visible components and greatly increases the gravitational potential of the galaxy. It governs dynamical interactions and increases the flow of accretion. Moreover, it is responsible for the flat rotation curves of galaxies.

Elliptical Galaxies

In contrast to spiral galaxies, ellipticals tend to be relatively faint and featureless. The star-forming gas has been depleted during their lifetime and star formation has mostly seized. Although many bright, massive stars decorated the galaxies magnificent past, the current stellar population is old and diffuse. However, short periods of star formation can occur when the galaxy's gas supply is replenished during a merger event. Elliptical galaxies have typically undergone numerous merger events in the past, which lead to the formation of their elliptical shape and a hierarchical growth in mass. Their high mass naturally attracts further galaxies and often places them in the centers of galaxy clusters. In addition, they are typically surrounded by large numbers of GCs and the stripped cores of devoured galaxies. Although elliptical galaxies are not the dominant type of galaxies in the Universe, they are the most massive ones. An image of Messier 87, a supergiant elliptical galaxy in the Virgo constellation, is shown in Figure 2.4.

According to the Hubble-Sequence, elliptical galaxies are categorized into 7 types, E0 - E7,

depending on their ellipticity (see Figure 2.1). Ellipticals of class E0 are nearly circular, whereas E7 galaxies are relatively flat.

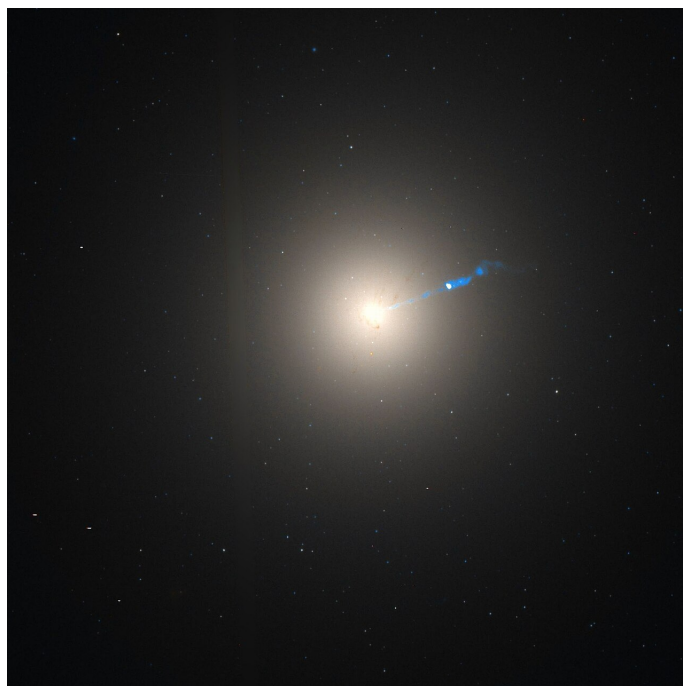


Fig. 2.4: Composite optical/infrared image of the supergiant elliptical galaxy Messier 87, taken with the Hubble Space Telescope (NASA, 2009).

Other Galaxies

Another group of galaxies are the so-called lenticular galaxies (Type S0). They embody an intermediate type of galaxies between spirals and ellipticals. Lenticular galaxies typically have a large disc, but not much star forming activity, as they have exhausted most of their star-forming gas. The galactic disc does therefore not display prominent spiral arms. Similar to spiral galaxies, lenticular galaxies are split into groups of barred (Type S0A) and unbarred lenticulars (Type S0B).

Galaxies, which exhibit no disk-like or ellipsoidal structure, are called irregular galaxies (denoted Irr or Im in the Hubble-Sequence). One example for an irregular galaxy in the Local Group is the Small Magellanic Cloud. As it only contains a few hundred million stars and exhibits a mass of only 7 billion solar masses (Bekki et al., 2009), it is considered to be a dwarf galaxy. Further companions of the Milky Way are small, low-luminosity galaxies of spherical shape and old stellar population, classified as dwarf spheroidal galaxies (Type dSph).

2.3 Star Formation

Galactic evolution and emission characteristics are strongly affected by the interplay between star formation and the ISM. Star formation takes place in cold molecular gas clouds

with masses of $10^4 - 10^7 M_{\odot}$ (Koda et al., 2023) and behaves differently depending on the galactic environment. It is believed that stellar bars and spiral arms stimulate the formation of molecular clouds through their dynamical evolution. The induced star formation creates feedback that affects the growth and quenching of the galaxy. Evidence for these processes can be seen in the molecular gas cloud distribution (Koda et al., 2023).

Further feedback is generated by stellar winds and supernova explosions, which can lead to gas outflows and superwinds. The produced shock fronts push the gas outwards, enriching the surrounding medium, and sometimes expanding the sites of star formation (Conselice et al., 1999, and references therein).

In addition, spiral galaxies are often surrounded by atomic gas reservoirs that extend far into the galactic halo (2-4 times the radius of the optical disc; Eibensteiner et al., 2023). This gas possibly drives accretion mechanisms from the circumgalactic medium and cosmic web and will fuel future star formation if it falls onto the disc.

In elliptical galaxies, molecular gas is far less abundant and tends to be concentrated in the central region. However, $\sim 15\%$ of early type galaxies show signs of recent star formation (Yi et al., 2005).

Further processes that greatly affect star formation and galactic evolution are tidal interactions and mergers with other galaxies. The accreted matter can feed super-massive black holes and initiate intense bursts of star formation over short time periods, so-called starbursts (Bellochi et al., 2020).

The SFRs of starburst galaxies can reach ~ 10 to $\sim 1000 M_{\odot} \text{ yr}^{-1}$ (Ianjamasimanana et al., 2022). While for some galaxies, the starburst is well distributed across the galaxy, others experience an intense, localized burst, e.g. in the galactic center. Such a localized burst is likely initiated by gas accretion on to the center, the inflow of gas through the bars, or an interaction with another galaxy. Starburst regions exhibit a high density of massive stars, which expell large amounts of energy into the surrounding medium and greatly affect the gas distribution and dynamics of the host galaxy (Ianjamasimanana et al., 2022, and references therein).

Energy released by AGNs can heat and expell the gas reservoirs. According to a study of Zinn et al., 2013, AGNs exhibit a higher SFR if they produce radio jets. Jet-driven shocks can initiate star formation and are thought to accelerate gas cooling (Conselice et al., 1999, and references therein).

3 X-ray Sources and Observations

3.1 X-ray Observations of Galaxies



Fig. 3.1: Image of Messier 83 in the soft 0.3 – 1 keV (red), medium 1 – 2 keV (green) and hard 2 – 8 keV (blue) X-ray band, taken with the Chandra Advanced CCD Imaging Spectrometer. The bright dots represent X-ray point sources such as cataclysmic variables and low-mass X-ray binaries. Additionally, one can see diffuse emission (mainly in the soft band X-ray band), which originates from the hot gas within the halo and galactic plane (NASA/CXC/U.Leicester/U.London/R.Soria/K.Wu, 2003).

In the 1990s, Einstein and ROSAT missions have already found that spiral galaxies emit soft X-rays in the 0.1–2.4 keV band. Although they reach luminosities of up to $10^{38} - 10^{40}$ erg s⁻¹ (Cui et al., 1996; Fabbiano et al., 1992; Read et al., 1997), detailed studies of their morphology weren't yet possible. The lack of spatial resolution made it hard to segregate point sources from diffuse gas emission, and the X-ray emission could therefore not be used in multi-wavelength studies. These circumstances have changed in the advent of modern X-ray observatories such as Chandra and eROSITA. The Chandra telescope has a remarkably high

spatial resolution and allows us to view galaxies at distances up to ~ 40 Mpc in unprecedented detail (Wang et al., 2016). An example Chandra RGB X-ray image in the energy range $0.3 - 8$ keV is shown in Figure 3.1. It represents the nearly face-on barred spiral galaxy Messier 83 and clearly shows large-scale diffuse structures in addition to bright point sources. The point sources, which are mostly low-mass X-ray binaries and Cataclysmic Variables (see section 3.2), often possess a harder spectrum and therefore emit more light in the medium $1 - 2$ keV (green) and hard $2 - 8$ keV (blue) X-ray band. The diffuse emission, on the other hand, appears more red-ish due to its dominance in the soft X-ray band. For galaxies with distances up to ~ 20 Mpc, XMM-Newton observations enabled studies of the emission origin via spectral analysis (e.g. Randall et al., 2006). The results have shown that the two dominating components of galactic X-ray emission are X-ray binaries and diffuse hot gas. However, the X-ray emission that originates from the hot plasma in the ISM is predominantly generated at energies below ~ 2 keV; an energy range that is strongly contaminated by background emission. The limited sensitivity and resolution of the instruments, combined with the strong background contamination, made studies of the diffuse X-ray emission relatively challenging. Consequently, only local group or really bright nearby galaxies were included in these studies.

The recently launched X-ray telescope eROSITA was designed for a high sensitivity in the soft X-ray band is therefore the perfect instrument for studies of the diffuse X-ray emission in galaxies. By analyzing the data from eRASS1 to eRASS4, we will be able to compare the X-ray emission of dozens of galaxies within our local Universe. The eROSITA mission will be explained in greater detail in chapter 4.

3.2 X-ray Point Sources

Among the brightest X-ray point sources in galaxies are X-ray binaries (XRBs). They are binary star systems composed of a donor and a neutron star or black hole accretor. Constellations, in which the donor star has a higher mass than the accretor (typically $\gtrsim 10 M_{\odot}$; Tan, 2012), are called high-mass X-ray binaries (HMXBs). Systems with less massive donor stars on the other hand, are called low-mass X-ray binaries (LMXBs).

Low-mass X-ray Binaries

In LMXB systems, the donor is either a main sequence star, a red giant or a white dwarf. The accretor is surrounded by an accretion disk due to mass transfer from the donor. The infalling matter leads to a release of gravitational potential energy in the form of X-rays. Hence, LMXBs are typically bright in X-rays, but faint in the optical. The accretion disk is the brightest part of the system (Tauris et al., 2006). In addition, some neutron star LMXBs have been observed to emit periodic X-ray bursts, which are typically more luminous than their ordinary emission by a factor of 100. Such events are categorized in Type I and Type II X-ray bursts. They are believed to occur when the accumulated matter from the donor star leads to bursting fusion reactions on the neutron star's surface. Type I bursts are a consequence of thermonuclear runaway processes and gradually decline after a sharp rise in luminosity. Type II bursts, on the other hand, result from gravitational potential energy

release and can occur many times in a row as a quick pulse shape. Type I bursts are far more common. In fact, Type II bursts have only been detected from two sources (Lewin et al., 1993), e.g. the Rapid Burster in the GC Liller 1.

LMXBs are often found in regions associated with old stellar populations, such as the Galactic center and GCs (Arnason et al., 2021). In fact, the observed spatial distribution indicates a strong concentration of LMXBs within the central 2kpc of the Galaxy (Grimm et al., 2002). This can be explained by the fact that some dynamical LMXB formation channels might only exist in dense stellar regions. LMXBs can be created by exchange interactions between neutron stars and primordial binaries, the tidal capture of a main sequence star by a neutron star, or by direct collision of a neutron star with a red giant (Zurek et al., 2009). The evolution of a LMXB out of a primordial binary system on the other hand, is far less likely (Servillat et al., 2008). According to Grimm et al., 2002, $\sim 50\%$ of LMXBs are located in the Galactic disk, while $\sim 25\%$ are concentrated in the Galactic buldge.

A subcategory of LMXB are the so-called Millisecond Pulsars (MSPs). They are pulsars with short rotational periods, and about as luminous as Cataclysmic Variables (Bassa et al., 2004). MSPs are believed to be neutron stars from LMXB systems, that have been spun up due to angular momentum transfer from the companion star. Such MSPs are typically observed in the radio band and can therefore be identified by their radio counterpart (Servillat et al., 2008). In some cases, however, a portion of the MSP surface near the magnetic poles can generate X-ray radiation due to heating by relativistic particles from the magnetosphere. In addition, it is possible that those relativistic particles generate non-thermal, pulsed X-ray emission (Bhattacharya et al., 2017).

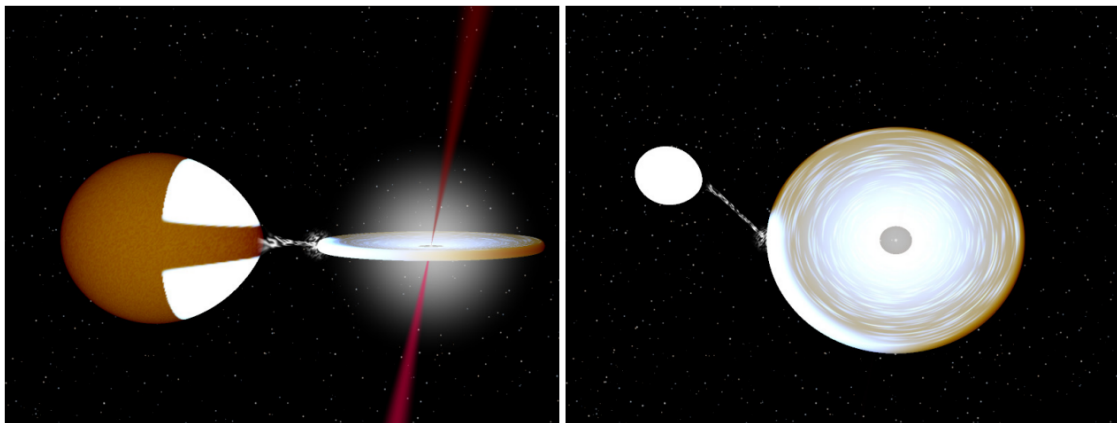


Fig. 3.2: Two illustrations of LMXB systems in different configurations.

Left image: A transient, eclipsing LMXB during an outburst (e.g. GRS 1747-312).

Right image: a persistent ultra-compact X-ray binary, viewed at a low inclination angle (e.g., 2S 0918-549, Bahramian et al., 2023; Zhong et al., 2011).

High-mass X-ray Binaries

The donor component in HMXB systems is a massive star, typically an O or B star, a supergiant or a Wolf-Rayet star. High-mass stars are very luminous in the optical band;

HMXB systems are therefore easier to detect than LMXBs. Furthermore, massive stars have significantly higher mass-loss rates due to stellar winds. The expelled stellar wind material can, in addition to Roche lobe overflow, be accreted by the compact object. This further increases the mass transfer rate and leads to very energetic X-ray emission ($kT \gtrsim 15$ keV) when the material falls onto the surface. For reference, LMXBs typically exhibit a softer spectrum with $kT \lesssim 10$ keV (Tan, 2012). Similar to LMXBs, HMXBs can exhibit various degrees of variability, e.g. X-ray pulses and X-ray bursts. X-ray pulses are produced when the infalling material is channeled into the poles by the strong magnetic field of the compact object (Tauris et al., 2000).

In contrast to LMXBs, HMXBs trace the young stellar population, as massive O and B stars have relatively short lifespans compared to low-mass stars. They contain stars of age $t \lesssim 10^7$ yrs ($t \gtrsim 10^9$ yrs for LMXBs; Tan, 2012) and are therefore mainly found in the galactic planes of young spiral galaxies. According to Mineo et al., 2012a, the presence of HMXBs hints towards recent star-forming activity of the host galaxy. In fact, they found that their collective luminosity L_{HMXB} scales with the SFR: $L_{\text{HMXB}} \approx 2.6 \cdot 10^{39} \cdot \text{SFR}$. However, the short lifespan also leads to a smaller timeframe in which they can be detected: LMXBs experience accretion on timescales of $10^7 - 10^9$ yrs, whereas HMXBs only accrete for $\sim 10^5$ yrs (Tan, 2012).

Cataclysmic Variables

In terms of brightness, LMXBs are followed by white dwarfs that are accreting material from low-mass companions, so-called Cataclysmic Variables (CVs). Such systems are common within the Galactic field, and even more abundant in dense, stellar regions such as GCs and the centers of galaxies. They can either originate from primordial binaries or result from close stellar encounters. A correlation between the number of faint sources and the stellar encounter rate of GCs indicates that most CVs in GCs are formed via close stellar encounters (Bassa et al., 2004). They can be identified by a blue, variable optical counterpart (Servillat et al., 2008).

Active Binaries

Chromospherically or magnetically active binaries (ABs) are typically fainter than LMXBs and CVs. They are categorized in 3 different types. The first two are detached binary systems of either two main sequence stars, or a main sequence star and a giant/sub-giant, while the third type are contact binaries (Bassa et al., 2004). ABs can be identified by their main-sequence-like, variable optical counterparts (Servillat et al., 2008).

3.3 Diffuse X-ray Emission

Recent Chandra observations have shown that normal galaxies exhibit diffuse X-ray emission with different types of morphologies. It is produced by thermal gas with a fairly hot $kT \sim 0.2$ keV (which is equivalent to a temperature of $T \sim 10^6$ K) component (Read et al., 1997; Strickland et al., 2004a) and can be separated into two constituents:

- X-ray emitting gas above the galactic plane, which escaped the galaxy due to the mechanical energy output from winds generated by massive stars and supernovae (e.g. Strickland et al., 2004b),
- Coronal X-ray emitting gas which is associated with galactic fountains (e.g. Kuntz et al., 2003).

The Interstellar Medium

This X-ray emitting gas originates from the ISM, which is assembled by three components:

- Clouds of cool gas, consisting of neutral atoms and molecules. These clouds typically have particle densities n exceeding 10 cm^{-3} and temperatures T below 10^2 keV .
- The warm inter-cloud medium, which has a slightly higher temperature of roughly $T \sim 10^4\text{ K}$. Due to the higher temperature, a significant fraction of the hydrogen particles is now partially ionized. The particle density is slightly lower at $n \sim 1\text{ cm}^{-3}$ (Cox et al., 2005).
- Another significant contribution originates from stellar material, which is expelled into the ISM by stellar winds and supernova explosions. These processes generate energetic shock waves, which heat and ionize the gas, creating hot plasma with temperatures up to $T \sim 10^6 - 10^7\text{ keV}$. Due to the high thermal pressure, the plasma expands and the density decreases below $n < 0.01\text{ cm}^{-3}$.

The diffuse X-ray emission that we detect from galaxies is produced by the hottest of these components, the thermal plasma in the hot phase of the ISM.

Stellar Winds

While stars are bound by self-gravity, strong radiation pressure dominates the outer layers and produces a stream of charged particles, the so-called stellar wind, into the surrounding medium. This flow of gas originates in the upper atmosphere and causes stars to lose a significant fraction of their mass during their lifetime (Mitchell, 2023).

As stars are the main production sites of heavier elements, they are responsible for the chemical enrichment of their host galaxy. Stellar winds are, alongside supernova explosions, the two primary mechanisms to spread and enrich such elements in the neighboring environment (Higgins et al., 2023).

The same two mechanisms are responsible for the production and distribution of hot thermal plasma, which we detect as soft X-rays. While the stellar winds of low-mass stars like the Sun are relatively slow ($400 - 760\text{ km s}^{-1}$, Johnstone et al., 2015), massive O and B stars produce winds with very high velocities, up to $v \sim 2000\text{ km s}^{-1}$ (Castor et al., 1975). Such high-energy winds produce strong shock waves and create stellar wind bubbles composed of hot, ionized plasma.

Supernova Explosions

Supernova (SN) explosions can be separated into two categories: core-collapse SNe and type Ia SNe.

Core-collapse SNe occur, when a massive star ($M > 8 M_{\odot}$) has reached the end of its lifetime. As the supply of nuclear fusion material, such as H, He, C, N and O, is depleted, nuclear burning in the core ceases. Due to the lack of thermal pressure, self-gravity causes the iron core to contract, forming a degenerate neutron star. Infalling matter from the stellar envelope is reflected at the core's surface and creates an outward moving shock front. As protons and electrons recombine in the core, the emitted neutrinos fuel the shock front with enormous amounts of energy, generating an eruptive explosion. The outer stellar layers are expelled into the surrounding medium, while depending on the mass, a neutron star or black hole is left behind.

Type Ia SNe on the other hand only occur in binary or multiple star systems. When a low-mass star ($M < 8 M_{\odot}$) reaches the end of its lifetime, the envelope is expelled into the environment via stellar winds. When the remaining core, a so-called white dwarf (WD), is located in a close binary system, it will start to accrete matter from its stellar companion. If the mass transfer rate is sufficiently high, chances are that the white dwarf will, at some point, surpass the Chandrasekhar mass limit of $M \sim 1.4 M_{\odot}$. Consequently, explosive C-burning is ignited, leading to runaway thermonuclear explosion which destroys the WD. Type Ia SNe can also occur if the Chandrasekhar limit is surpassed by two merging WDs (Mitchell, 2023).

SN explosions eject a huge amount of stellar material into the environment. As the shock waves propagate into the surroundings, they interact with the ISM and stellar wind, producing hot thermal plasma and accelerating non-thermal particles. The structure that is created around the explosion site is called a supernova remnant (SNR).

Superbubbles and Galactic Fountains

In spiral galaxies with many young stars, the large amount of stellar winds and SN explosions creates so-called superbubbles. The hot, ionized gas within these superbubbles expands to densities of $n < 0.01 \text{ cm}^{-3}$ and reaches temperatures of $T \sim 10^6 \text{ keV}$ (e.g. Wang et al., 1991). These hot superbubbles can be interpreted as an additional component to the ISM, observable as diffuse X-ray emission, which will remain in the galaxy for millions of years, as the cooling mechanisms of thin hot plasma are very inefficient.

If the SFR of a galaxy is sufficiently high, large-scale energetic outflows, so-called superwinds, can occur (Heckman et al., 1990). They can transport large amounts of gas and newly synthesized elements, possibly breaking out of the galactic plane, heating and enriching the intergalactic medium (IGM). These superwinds are of particular interest for cosmology, as the transport of hot gas is key for the understanding of the metallicity evolution of galaxies (e.g. Edmunds, 1990). They might be the origin of the X-ray emission that is found well above the galactic plane of edge-on starburst galaxies (e.g., Martin et al., 2002).

If this gas is not able to escape from the disk into the halo region, however, it will fall back onto the disk, forming a galactic fountain. During the outgoing phase, the X-ray emitting gas is still hot. However, such outflows cool quickly due to adiabatic expansion, and turn

into anomalous high velocity H I clouds during the infalling phase (Avillez et al., 2000). Such galactic fountains and outflows can also be observed in X-rays.

3.4 N_{H} map

As explained in the previous section, the ISM consists of multiple gaseous components with varying particle densities. Most of this gas is made up of hydrogen and helium, as they are by far the most abundant elements in the Universe. The bulk of helium nuclei was produced during the primordial nucleosynthesis, while heavier elements are synthesized in stars. According to Croswell, 1996, hydrogen makes up 74% of the mass in the Milky Way, while helium accounts for 24% and heavier elements for only 2%.

These baryonic particles, which are distributed within the ISM of our galaxy, interact with X-rays via photoelectric absorption. Wilms et al., 2000, determined the absorption cross section σ to be strongly correlated with energy $\sigma \sim E^{-3}$, which implies that the absorption particularly affects the soft X-ray spectrum. Qualitative knowledge of the baryonic particle column density in the line of sight of our observations is therefore critical to account for the modification of the spectrum. Due to its dominant prevalence in our galaxy, and since it can be conveniently measured via H I 21 cm line emission, the neutral hydrogen abundance is used as an approximation for the total number of interstellar gas particles.

In 2016, The HI4PI Collaboration (HI4PI, 2016) published the HI4PI survey, which quantifies the total number of H I hydrogen atoms in the vicinity of the Milky Way. It uses the data of the Effelsberg-Bonn HI Survey (Winkel et al., 2016), as well as the third revision of the Galactic All-Sky Survey (Kalberla et al., 2015) and accounts for all H I atoms in the velocity range $-600 \text{ km s}^{-1} < v_{\text{LSR}} < 600 \text{ km s}^{-1}$. NASA's HEASARC n_{H} tool makes use of the HI4PI survey to calculate the hydrogen column density n_{H} in the direction of specified coordinates within a given cone radius. However, as the HI4PI survey does not include molecular hydrogen, these results only pose a lower limit to the number of hydrogen particles interacting with the X-ray emission (Sasaki et al., 2022).

4 The eROSITA Mission

eROSITA is a relatively new X-ray telescope developed by the Max Planck Institute for extraterrestrial Physics (MPE). On July 13, 2019, it has been launched from the Baikonour cosmodrome as a part of the Russian-German Spectrum-Roentgen-Gamma (SRG) mission, and is now operating in a stable orbit around the L2 Lagrange point. The telescope consists of seven telescope modules (TMs), which are arranged in a hexagonal shape and are each equipped with a CCD detector. However, in contrast to the other modules, TMs 5 and 7 were not equipped with an aluminium on-chip optical light filter. As a consequence of that, these modules are contaminated by optical light from a small fraction of sunlight that reaches the CCD. An image of the eROSITA telescope is displayed in Figure 4.1 (Predehl et al., 2020).

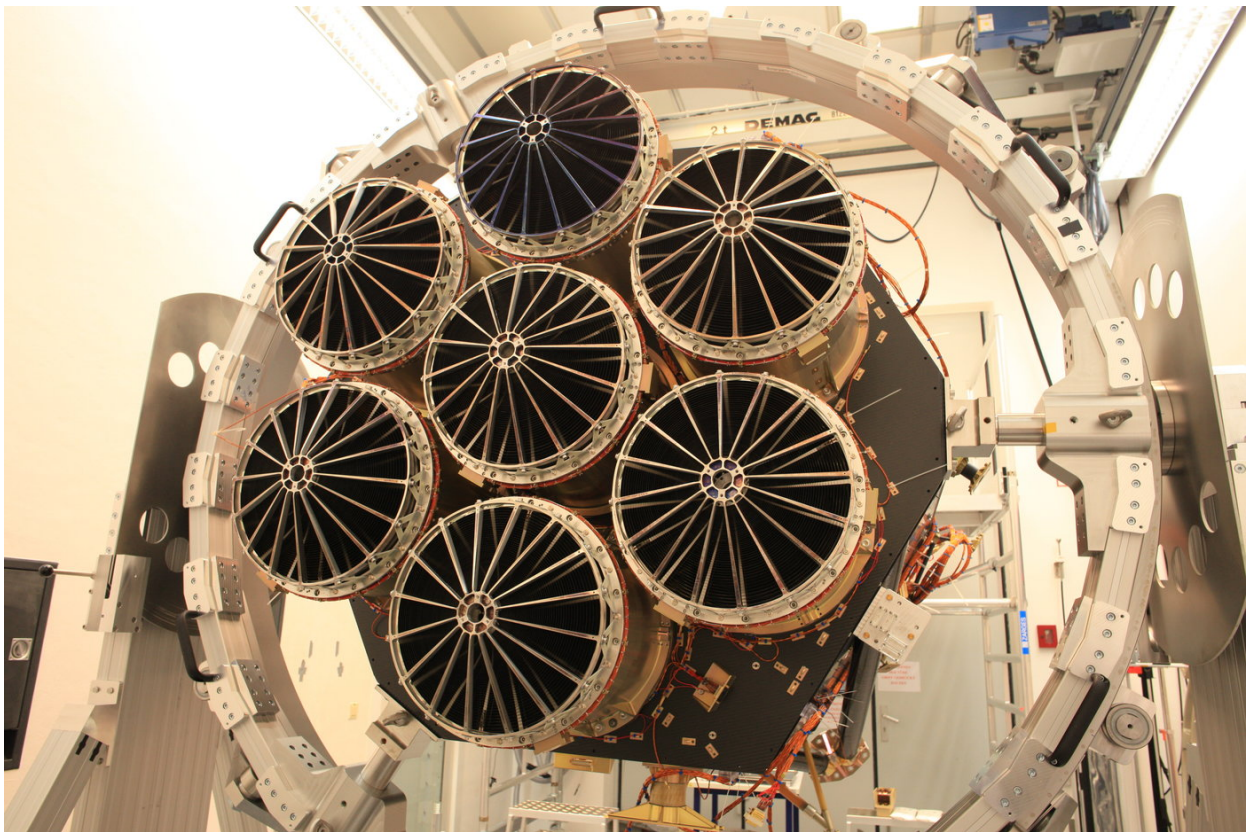


Fig. 4.1: The eROSITA X-ray telescope (Friedrich, 2019).

The concept of the eROSITA instrument is an advancement of previously developed devices by the MPE, e.g. the X-ray telescope for the ROSAT X-ray satellite mission. The first complete all-sky survey with an imaging X-ray telescope was carried out by ROSAT in the energy band $0.1 - 2.4$ keV. By completing 8 complete scans of the celestial sphere, the eROSITA mission aims to increase the sensitivity of the ROSAT All-Sky Survey by a factor of 25 and to provide the first imaging survey in the hard $2.3 - 8$ keV band. Each of these *eRASS* scans will last 6 months.

eROSITA is highly sensitive in an energy range between 0.2 and 8 keV and covers a remarkably large field of view (FOV) with a diameter of 1 degree (Predehl et al., 2020). This makes eROSITA the perfect instrument to conduct an all-sky survey of the X-ray sky, allowing us to study the spectral properties and the distribution of extended X-ray sources (Sasaki et al., 2022). The goal of the eROSITA mission was to complete the All-Sky Survey by the end of 2023. As of September 2023, eROSITA has completed 5 all-sky scans, and is currently in safe mode, not collecting further data. Beforehand, eROSITA carried out performance verification observations during its journey to the Lagrange point L2 in order to test and calibrate the instruments (Predehl et al., 2020). A view of our Universe, as observed by eROSITA during eRASS1, is shown in Figure 4.2.

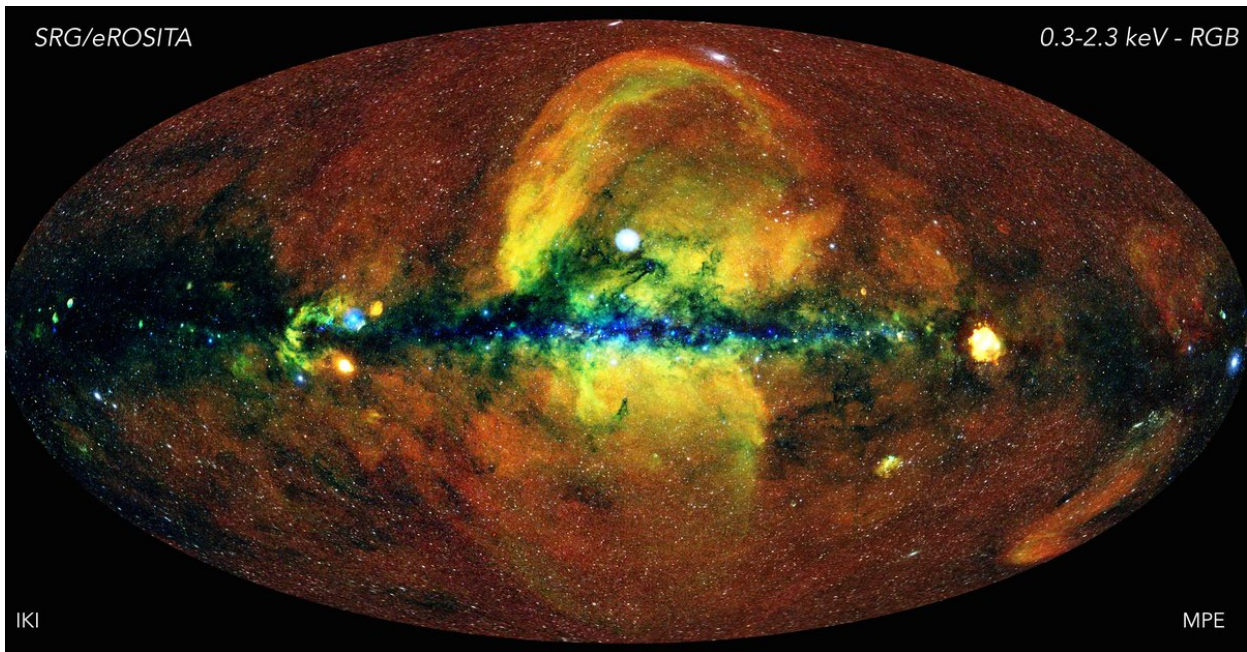


Fig. 4.2: The Universe, as seen with the eROSITA X-ray telescope in the 0.3–2.3 keV energy range (Sanders et al., 2020).

Alongside eROSITA, which is the primary X-ray telescope, the SRG observatory also carries the ART-XC (Astronomical Roentgen Telescope X-ray Concentrator). The ART-XC is an X-ray mirror telescope and complements the sensitivity of eROSITA at higher energies. It was developed under the lead of the Russian Space Research Institute IKI. Both instruments are attached to the *Navigator* spacecraft platform. Since the eROSITA mission was developed under german-russian collaboration, it has been agreed to divide the observational data between the two nations. The southern hemisphere has been assigned for studies by the German side, and the northern hemisphere for studies by the Russian side. A sky map, illustrating the separation between the German and Russian eROSITA sky, is displayed in Figure 4.3.

The primary goal of the eROSITA mission is to detect large samples of galaxy clusters up to redshifts $z > 1$. Such detections will greatly increase our understanding of the large-scale structure of the universe and provide crucial new data for the testing of cosmological models.

In particular, the results may constrain the rate of expansion of the Universe and deliver new insights into the nature of Dark Energy.

Galaxy Clusters can be detected due to X-ray emission from their hot intergalactic material. The eROSITA mission is expected to find 50 - 100 thousand of such galaxy clusters. Furthermore, it will enable the detection of obscured accreting black holes in nearby galaxies and millions of distant AGNs. Those new detections will provide important new insights into the evolution of supermassive black holes.

In addition to driving the study of cosmic structure evolution, the eROSITA mission will also greatly impact the study of Galactic X-ray source populations, such as SNRs, XRBs, and active stars. The increased sensitivity of the eROSITA all-sky survey will enable the identification of these objects and deliver new insights into their properties (Predehl et al., 2020).

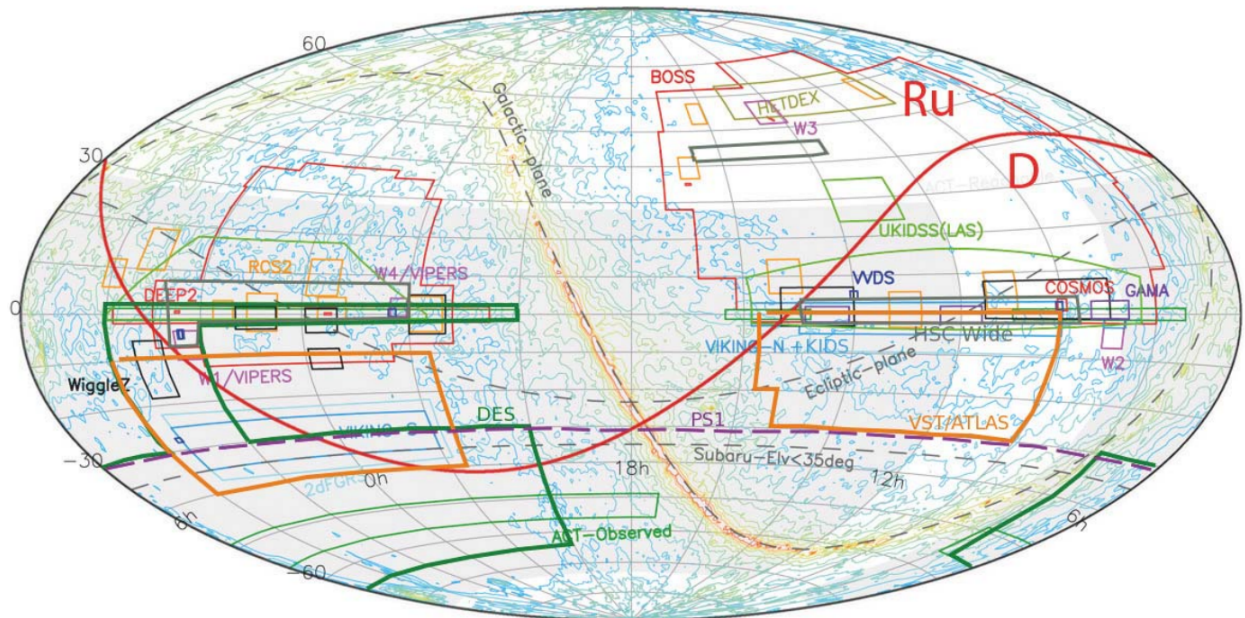


Fig. 4.3: Multi-band wide area optical imaging surveys (courtesy A. Nishizawa, IPMU) in equatorial coordinates. The thick red line marks the separation between the German and the Russian eROSITA sky. The German side is the southernmost one (Predehl, 2014).

5 Source Selection

5.1 The Nearby Galaxy Catalog

A Catalog of Neighboring Galaxies is an all-sky catalog of 869 galaxies with individual distance estimates up to ~ 17 Mpc, first presented by Karachentsev et al., 2004. The expanded, updated version was published 9 years later (Karachentsev et al., 2013). It contains data on a wide range of observables, e.g. angular diameters, apparent magnitudes, radial velocities, distance estimates and morphological types of the galaxies. In addition, it yields calculated parameters such as the Holmberg diameters and H I masses. The catalog therefore provides the groundwork for a large sample study of nearby galaxies. The acquired positions and diameters will be used to extract eROSITA images and spectra for further analysis. The angular diameters of the galaxies within this catalog are defined by the $26.5 \text{ mag/arcsec}^2$ Holmberg isophote in the B band.

5.2 The eROSITA Pipeline

The REMEIS EROPIPELINE is a data processing software developed by the scientists Steven Hämmerich, Philipp Weber and Aafia Zainab at the Dr. Karl Remeis-Observatory in Bamberg. It is composed of multiple scripts, such as ERO-PIPELINE, ERO-MODIFY-CATALOG and ERO-CREATE-REGIONS, which operate upon the eROSITA Science Analysis Software System (eSASS; MPE, 2023a). These scripts provide a variety of extraction methods to acquire and analyse eROSITA data:

- ERO-PIPELINE

The extraction pipeline is able to run source detection and extract source catalogs for a given position. It can also be used to produce X-ray RGB images, optical images and eventlists at specific coordinates. As an input it requires region files/specs or the RA , DEC coordinates of the desired positions.

Furthermore it is able to run srctool and extract spectra, light curves, as well as RMF, ARF and BKG files for a given area.

- ERO-MODIFY-CATALOG

This script produces a region catalog based on an empirical fit to count-rates and region radii for point sources. Receiving an eROSITA-formatted catalog, the script will generate a modified version of the input catalog with appropriate region sizes for the sources.

- ERO-CREATE-REGIONS

This script also requires an input source catalog. Based on this catalog, it will create custom region files for an input fits table with extraction targets. These region files can be used for the cheeing of X-ray sources. *Cheeing* denotes the exclusion of contaminating sources within an extracting region, which would otherwise distort the spectrum of the celestial object, such as fore- and background sources. By submitting

the modified catalog generated with `ERO-MODIFY-CATALOG`, one can exclude the point sources located in the direction of a galaxy from spectral extraction. An example can be seen in Figure 6.9, where the excluded sources are marked by green circles.

Furthermore, `EROPIPELINE` encompasses the scripts `ERO-ANALYSIS` and `ERO-FLAGS`, which provide an analysis framework for the extracted sources and a method of decoding and encoding eROSITA event filtering flags. Each task makes use of at least `evtool` and `srctool` and can be controlled by the user by modifying the eSASS input parameters.

The galaxy positions and diameters acquired from the Catalog of Neighboring Galaxies were submitted to `ERO-PIPELINE` via an input fits catalog to retrieve eventlists and images of the given coordinates. The extraction has been carried out with 020 processing: composite eventlists and images have been acquired from all 7 TMs, under usage of the on-chip filter (if available) for all energy bands (see Table 5.1).

X-ray band	Energy range
total	0.2 – 5.0 keV
soft	0.2 – 0.7 keV
medium	0.7 – 1.2 keV
hard	1.2 – 5.0 keV

Tab. 5.1: X-ray energy bands of the eRASS sources.

The retrieved images include eROSITA RGB X-ray images, as well as optical images from the STScI Digitized Sky Survey (DSS, 1994). However, the diffuse emission detected by eROSITA is very faint for most of the galaxies. Therefore, the counts from the four eROSITA All-Sky Surveys eRASS1 - eRASS4 have been put together to acquire merged eventlists and X-ray images with higher photon statistics. Still, the bulk of the galaxies remained very faint, with less than 1000 counts detected within the Holmberg diameters of all but 9 galaxies. These counts also include fore- and background emission. In order to better the visibility of the X-ray emitting structures, the X-ray images have been rebinned to a value of 160 virtual pixels per image pixel using the `evtool_image_rebin` input flag.

Since the script automatically filters galaxies that are located on the side of the night sky allocated to the Russian scientists, results were acquired for 439 out of the 869 galaxies.

5.3 List of Parameters

In the first step of organizing and selecting the galaxies suited for further analysis, an extended list of parameters has been created for the 439 galaxies. As the detected emission of most galaxies is too faint for further analysis, the list has been reduced to the galaxies with a semi-major axis $a \geq 90$ arcsec. The Large and Small Magellanic Clouds have also been excluded due to the large amount of intensive studies carried out by other authors. After this pre-selection, 105 galaxies remained. For 72 of these galaxies, the SFRs were acquired from the literature. This galaxy sample was selected for further analysis.

The parameter lists for these sources are presented in Table 5.2 and Table 5.3. They contain

the galaxies' name, their right ascension RA and declination DEC in deg, semi-major axis a and semi-minor axis b in arcsec, the position angle PA in deg, distance d in Mpc and their morphological classification. All values except the position angle and the morphological classification were acquired from the Catalog of Neighboring Galaxies (Karachentsev et al., 2013), retrieved from the VizieR website (Ochsenbein et al., 2014). The values for the semi-major and semi-minor axes are defined by the galaxies' 26.5 mag/arcsec² Holmberg isophotes in the B band. The position angles were acquired from the The Heraklion Extragalactic Catalogue (HECATE; Kovelakas et al., 2021) and the NASA/IPAC Extragalactic Database (NED; NASA/IPAC, 2018). For some galaxies, neither of the two references presented a PA value. In these cases, the PA value was set to zero. The morphological classifications of the galaxies were retrieved from NED (NASA/IPAC, 2018). They include information on whether the galaxies exhibit an AGN (e.g. Seyfert "Sy" galaxies) and/or an ongoing burst of star formation ("Sbrst").

Table 5.2 presents the targets with the best photon statistics (18 galaxies with ≥ 250 counts), sorted by counts, whereas Table 5.3 lists the parameters of the remaining galaxies in alphabetic order.

ID	NAME	RA	DEC	a	b	d	Counts	Classification
1	NGC 5128	201.3704	-43.0167	1040.1	811.3	3.75	7089	S0 pec;Sy2 BLLAC
2	Sculptor d.	15.0392	-33.7092	1194.3	812.1	0.09	3083	E?
3	Carina	100.4029	-50.9661	736.5	493.5	0.1	2735	E3
4	NGC 5236	204.2504	-29.8678	558.6	497.2	4.92	2005	SAB(s)c;HII Sbrst
5	NGC 300	13.7229	-37.6825	771	547.4	2.15	1364	SA(s)d
6	NGC 1291	49.3275	-41.1081	433.5	398.8	8.8	1075	(R_1)SB(1)0/a HII
7	NGC 6744	287.4413	-63.8578	641.4	416.9	8.3	1187	SAB(r)bc LINER
8	Bootes I	210.0000	14.5000	600	366.0	0.07	1134	Dwarf Spheroidal?
9	Sextans dSph	153.2625	-1.6144	906	588.9	0.09	1043	dSph
10	NGC 1313	49.5642	-66.4975	377.7	302.2	4.07	991	SB(s)d HII
11	Fornax	39.9779	-34.5258	533.4	373.4	0.14	975	dE0
12	NGC 4945	196.3588	-49.4711	845.4	160.6	3.8	830	SB(s)cd: sp Sy2
13	NGC 55	3.7854	-39.2203	1114.5	189.5	2.13	579	SB(s)m: sp
14	NGC 4826	194.1842	21.6847	414	215.3	4.37	473	(R)SA(rs)ab;HIISy2
15	NGC 5068	199.7304	-21.0392	300	264.0	5.45	410	SB(s)d
16	NGC 5102	200.4908	-36.6297	404.7	129.5	3.4	319	SA0- HII
17	NGC 4594	189.9963	-11.6231	352.5	179.8	9.3	296	SA(s)a;LINER Sy1.9
18	NGC 3621	169.5671	-32.8117	369	162.4	6.7	250	SA(s)d HII

Tab. 5.2: This table displays the properties of the most luminous (≥ 250 counts) galaxies from the selected sample. See Table 5.3 for more information.

ID	NAME	RA	DEC	a	b	d	Counts	Classification
19	Bootes II	209.5000	12.8333	201	146.7	0.04	127	dSph
20	Circinus	213.2888	-65.3392	207.6	89.3	4.2	97	SA(s)b: Sy2
21	Coma I	186.7458	23.9042	285	182.4	0.04	165	Galaxy group
22	DDO 47	115.4792	16.8006	140.4	119.3	8.05	41	IB(s)m
23	DDO 84	160.6746	34.4489	134.1	99.2	8.11	33	Im
24	DDO 161	195.8200	-17.4231	238.2	31.0	7.3	18	IB(s)m sp
25	ESO 115-21	39.4375	-61.3411	217.2	30.4	4.99	48	Scd
26	ESO 137-18	245.2471	-60.4875	104.1	302.2	6.4	12	SA(s)c
27	ESO 154-23	44.2100	-54.5731	249.6	44.9	5.55	70	SB(s)m
28	ESO 238-5	335.6254	-48.4050	92.7	55.2	7.8	13	IABm
29	ESO 269-58	197.6371	-46.9908	140.4	84.2	3.8	66	I0 pec
30	ESO 270-17	203.6971	-45.5475	475.5	57.1	3.6	140	SB(s)m
31	ESO 273-14	224.6263	-47.6986	114	493.5	9.9	53	SB(s)m pec
32	ESO 274-1	228.5563	-46.8125	404.7	40.5	3.09	101	Sd
33	ESO 300-14	47.4075	-41.0306	212.4	110.4	9.8	154	SAB:(s)dm
34	ESO 324-24	201.9058	-41.4806	99.3	181.3	3.73	49	IABm
35	ESO 325-11	206.2533	-41.8589	94.8	151.2	3.4	38	IB(s)m
36	ESO 364-29	91.4392	-33.0817	106.5	57.1	7.59	19	IB(s)m
37	ESO 383-87	207.3283	-36.0614	168.6	134.9	3.45	137	SB(s)dm
38	ESO 501-23	158.8467	-24.7542	104.1	129.5	7	14	SB(s)dm
39	HIZSS 12	112.5346	-22.0169	96	46.9	7.2	15	N/A
40	IC 1959	53.2992	-50.4106	122.1	28.1	6.05	36	SB(s)m: sp
41	IC 3104	184.6921	-79.7261	111.6	416.9	2.27	37	IB(s)m
42	IC 4710	277.1583	-66.9822	111.6	113.7	7.94	58	SB(s)m HII
43	IC 4951	302.3825	-61.8506	97.2	313.7	9.8	11	SB(s)dm: sp
44	IC 5052	313.0258	-69.2039	243.9	34.1	6.03	72	SBd: sp
45	IC 5152	330.6746	-51.2953	212.4	131.7	1.97	81	IA(s)m
46	IC 5201	335.2392	-46.0342	261.3	120.2	8.8	94	SB(s)cd Sy2
47	IC 5332	353.6146	-36.1017	249.6	217.2	7.8	140	SA(s)d
48	KK 208	204.1479	-29.5708	176.7	74.2	4.68	52	dwarf Irr
49	Leo A	149.8600	30.7464	172.5	105.2	0.81	74	Ibm
50	Leo I	152.1121	12.3081	293.1	231.5	0.25	123	E;dSph
51	Leo II	168.3717	22.1547	360.6	313.7	0.21	240	E0 pec
52	Leo IV	173.2375	-0.5333	219	170.8	0.16	101	dSph
53	Leo V	172.7900	2.2200	123	55.3	0.18	16	N/A
54	NGC 1311	50.0308	-52.1850	140.4	35.1	5.2	39	SB(s)m
55	NGC 1400	54.8783	-18.6881	104.1	97.1	24.5	113	SA0- HII
56	NGC 1533	62.4658	-56.1183	106.5	373.4	19.4	144	(L)SB(rs)0 ⁰ LINER
57	NGC 1637	70.3675	-2.8581	131.1	103.6	9.29	58	SAB(rs)c AGN
58	NGC 1744	74.9925	-26.0267	207.6	112.1	10	136	SB(s)d
59	NGC 2188	92.5396	-34.1061	140.4	35.1	7.4	24	SB(s)m
60	NGC 2283	101.4696	-18.2103	108.9	497.2	10	28	SB(s)cd
61	NGC 2683	133.1704	33.4172	404.7	97.1	7.73	153	SA(rs)b;LINER Sy2
62	NGC 2784	138.0808	-24.1717	165	66.0	9.82	19	SA(s)0 ⁰
63	NGC 2835	139.4704	-22.3553	267.3	179.1	10.3	133	SAB(rs)c HII
64	NGC 2903	143.0400	21.5006	377.7	181.3	8.87	173	SAB(rs)bc I-II HII
65	NGC 3104	150.9892	40.7569	106.5	398.8	16	11	IAB(s)m HII
66	NGC 3109	150.7800	-26.1600	598.5	113.7	1.32	180	SB(s)m

ID	NAME	RA	DEC	a	b	d	Counts	Classification
67	NGC 3115	151.3083	-7.7186	255.3	89.4	9.68	54	S0- PAS
68	NGC 3239	156.2704	17.1636	150.3	91.7	7.9	32	IB(s)m pec
69	NGC 3344	160.8758	24.9236	227.7	204.9	6.85	121	(R)SAB(r)bc HII
70	NGC 3351	160.9904	11.7036	217.2	147.7	10.05	66	SB(r)b;HII Sbrst
71	NGC 3368	161.6908	11.8197	267.3	181.8	10.42	160	SAB(rs)ab;Sy LINER
72	NGC 3377	161.9267	13.9856	157.5	91.3	10.91	49	E5-6
73	NGC 3379	161.9567	12.5817	161.1	143.4	11.12	115	E1 LINER
74	NGC 3384	162.0704	12.6292	165	74.3	11.38	37	SB(s)0-
75	NGC 3412	162.7221	13.4122	119.4	189.5	10.4	16	SB(s)0^0^PAS
76	NGC 3432	163.1296	36.6189	161.1	35.4	9.2	20	SB(s)m;LINER HII
77	NGC 3489	165.0775	13.9011	114	547.4	12.08	11	SAB(rs)0+ Sy;LINER
78	NGC 3521	166.4525	-0.0358	328.8	151.2	10.7	182	SAB(rs)bc;HII LINER
79	NGC 3593	168.6496	12.8186	176.7	76.0	10.8	23	SA(s)0/a;HII Sy2
80	NGC 3627	170.0625	12.9914	306.9	141.2	10.28	216	SAB(s)b;LINER Sy2
81	NGC 4136	182.3238	29.9275	119.4	811.3	7.9	45	SAB(r)c HII
82	NGC 4204	183.8100	20.6586	134.1	108.6	8	36	SB(s)dm
83	NGC 4455	187.1838	22.8225	97.2	162.4	8.4	16	SB(s)d? Sp
84	NGC 4517	188.1896	0.1150	360.6	46.9	9.7	64	SA(s)cd: sp HII
85	NGC 4559	188.9904	27.9597	328.8	134.8	8.1	151	SAB(rs)cd HII
86	NGC 4597	190.0538	-5.7992	166.8	76.7	10.1	48	SB(rs)m
87	NGC 4700	192.2817	-11.4114	122.1	812.1	7.3	10	SB(s)c? sp;HII Sy2
88	NGC 5206	203.4329	-48.1511	111.6	366.0	3.47	59	SB?(r?)0^-?
89	NGC 5253	204.9825	-31.6400	207.6	78.9	3.56	92	Im pec;HII Sbrst
90	NGC 5264	205.4042	-29.9139	104.1	40.5	4.53	23	IB(s)m
91	NGC 5398	210.3425	-33.0644	106.5	215.3	8.1	14	SB(rs)dm
92	NGC 6684	282.2413	-65.1733	119.4	588.9	8.7	45	(L)SB(r)0^+
93	NGC 7090	324.1192	-54.5572	306.9	55.2	6.7	100	SBc? Sp
94	NGC 7462	345.6967	-40.8350	165	28.1	10.1	14	SB(s)bc? sp
95	NGC 7713	354.0625	-37.9389	202.8	83.1	7.8	62	SB(r)d: HII
96	Orion	86.2583	5.0683	92.7	134.8	6.46	20	Sbd
97	Phoenix d.	27.7763	-44.4447	165	140.3	0.44	113	Sa;Sy1 Sy2
98	Segue 1	151.7633	16.0736	210	109.2	0.02	42	Globular cluster?
99	Sextans A	152.7533	-4.6928	176.7	146.7	1.32	64	IBm
100	Sextans B	150.0004	5.3322	180.9	124.8	1.36	44	ImIV-V
101	UGC 3303	81.2479	4.5050	168.6	131.5	7.14	68	Sd
102	UGC 4704	134.7513	39.2100	131.1	14.4	15.2	12	Sdm
103	UGC 5672	157.0871	22.5714	92.7	141.2	11.4	7	S?
104	UGC 7321	184.3917	22.5403	202.8	12.2	17.2	7	Sd HII
105	UGCA 193	150.6508	-6.0119	128.1	9.0	9.7	3	Sdm

Tab. 5.3: This table displays the properties of all galaxies from the selected sample with less than 250 detected counts. It contains the galaxy name, the right ascension RA in deg, the declination DEC in deg, the semi-major axis a in arcsec, the semi-minor axis b in arcsec and distance d in Mpc from the Catalog of Neighboring Galaxies (Karachentsev et al., 2013), the number of eROSITA counts and the morphological classification by NED (NASA/IPAC, 2018) of each galaxy.

5.4 X-ray and Optical Images

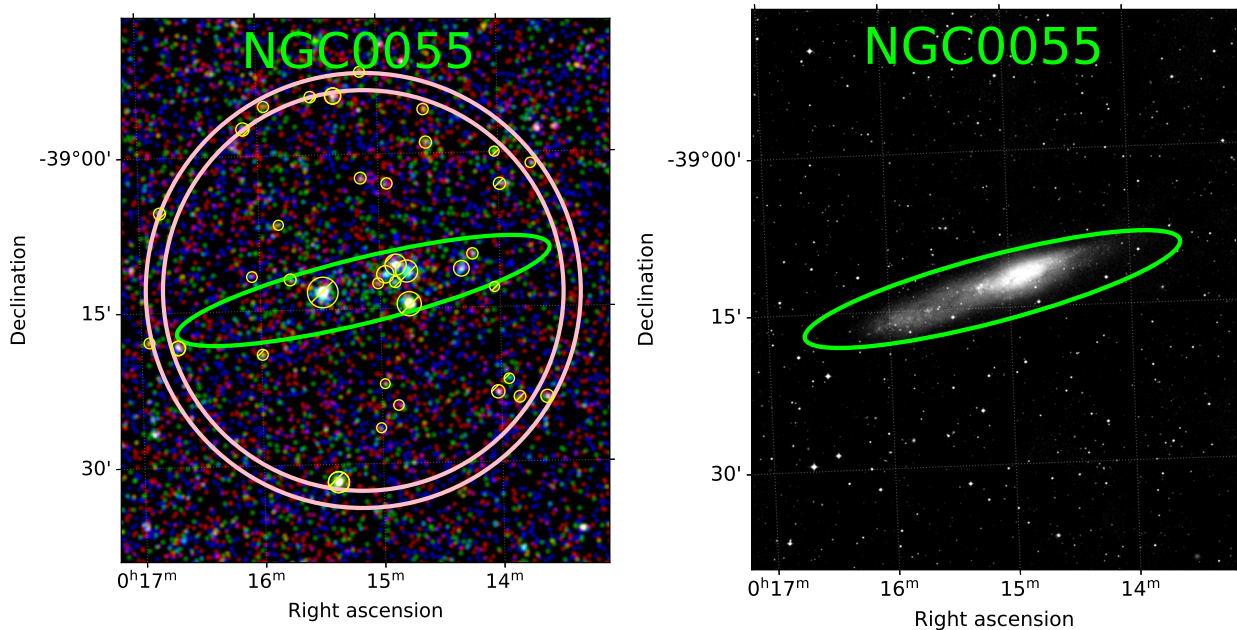


Fig. 5.1: Left side: RGB X-ray image in the 0.2 – 0.7 keV (red), 0.7 – 1.2 keV (green) and 1.2 – 5.0 keV (blue) bands of NGC 55 from merged eRASS1 - eRASS4 data. Right side: optical image from the STScI Digitized Sky Survey (DSS, 1994). The green ellipse marks the extraction region ($26.5 \text{ mag/arcsec}^2$ Holmberg isophote) of the galaxy. The surrounding red circles confine the background region. Cheesed-out sources are marked by smaller circles within the respective regions. Galaxy parameters: $a = 18.58 \text{ arcmin}$, $b = 3.16 \text{ arcmin}$, $\text{dist} = 2.13 \text{ Mpc}$. Classification: SB(s)m: sp.

In order to provide an overview on the X-ray emitting regions of the 72 selected galaxies, an extended image catalog has been created. It contains the merged eRASS1 - eRASS4 RGB X-ray and DSS optical images of each galaxy, which were acquired via the EROPIPELINE. The images of NGC 55 are portrayed in Figure 5.1 to provide an example.

The observed structure of the galaxies depends strongly on their size, distance, morphological type and our line of sight. From a face-on view, the galaxies appear more circular, whilst at higher inclination angles, they exhibit a higher eccentricity. When viewed from the side, elliptical galaxies generally display a more spherical shape than spiral galaxies. For high inclination angles, a higher electromagnetic flux is expected from the disk of spiral galaxies, as the hot gas is concentrated in a smaller area from our point of view. A good example of this can be seen in the images of NGC 4945 (Figure 6.17), where the emission is mainly seen in a broad line along the disk region. The position angle PA characterizes the rotation angle of the galaxy's elliptical shape relative to us. By using a Python 3.8 script created by Jonathan Knies, a scientist at the Dr. Reemis-Observatory, elliptical regions displaying the $26.5 \text{ mag/arcsec}^2$ Holmberg isophotes of each galaxy have been implemented into the images. They are marked by green ellipses in both the X-ray and optical images.

The optical images display the morphological type and general structure of the galaxies, e.g. the extent of the buldge, the amount of spiral arms and whether a central bar is present. They also indicate the presence of foreground stars as bright point-sources. As expected, some galaxies are much brighter in the optical than others. More distant galaxies generally appear dimmer, as we receive less of the emitted light. Smaller, less massive galaxies, such as dwarf galaxies, are also dimmer, since they contain less stars.

The emission seen in the X-ray images is subject to even greater variation, as it strongly depends on the amount of hot gas and X-ray point sources within a galaxy. Centaurus A, for instance, possesses a star-forming circumnuclear disk, which is believed to be fueled by recent AGN outbursts, and X-ray bright jets extending far into the halo (Espada et al., 2019). The circumnuclear disk and jets can be clearly seen in Centaurus A's X-ray image (Figure 6.3). The starburst galaxy Messier 83, which has the highest SFR ($4.17 M_{\odot} \text{yr}^{-1}$) out of the selected sample (according to the PHANGS-ALMA survey, Leroy et al., 2021), also has a bright circumnuclear region that can be seen in the X-ray image (Figure 6.5). The LINER galaxy NGC 6744 on the other hand, has a circumnuclear region that is dominated by old stellar populations. It is therefore believed that there is not much star formation going on in this region (Silva et al., 2018). This theory is supported by the lack of emission seen in its X-ray image (Figure 6.7)

A large sample of galaxies displays bright X-ray emission in the center. Due to the high stellar densities, it is likely to find X-ray point sources like CVs and LMXBs in the central regions of galaxies. In addition, many X-ray point sources are found distributed within the galaxy's Holmberg diameters. These could also be contaminating objects which don't belong to the galaxy, e.g. background AGNs or foreground stars. Within the framework of this study, we want to analyze the diffuse X-ray emission from the hot gas within the galaxies. Capturing the emission of X-ray point sources is therefore not in our interest. For this reason it has to be excluded from our data before the spectra of the galaxies can be extracted and analyzed. This was achieved by acquiring an eROSITA formatted catalog containing all detected sources in the stacked eRASS1 - eRASS4 surveys from the MPE Early Data Release site (MPE, 2023b). The catalog was modified using the ERO-MODIFY-CATALOG script, which generated appropriate region sizes for the catalog sources. The modified catalog has then been reduced to point-sources only, as the extended sources might encompass diffuse gas emission. Together with a fits table containing the extraction and background regions of the galaxies, the modified catalog was then submitted to the ERO-CREATE-REGIONS script, which generated custom region files for each galaxy and its background. These region files contain the extraction region of the galaxies defined by their Holmberg diameter, where all X-ray point sources are excluded. The background regions of the galaxies have been defined by a 100 arcsec thick ring surrounding the elliptical extraction region in a distance of 50 arcsec. The background extraction regions are marked by pink circles in the X-ray images. X-ray point sources located within this ring have also been excluded from the background extraction region. The excluded X-ray point sources are marked by yellow circles within the corresponding extraction regions. However some of the bright central regions of the galaxies were classified as extended sources by the source detection algorithm and were therefore not excluded. NGC 1291 is an example of such a galaxy (see Figure 6.9). In these cases, the bright central regions were later excluded by hand.

In the next step, these custom region files will be used for the extraction of the spectra of the diffuse gas within the galaxies in chapter 6. The X-ray and optical images of the 10 galaxies, which were included in the single spectral analysis, are presented in their respective subsections in section 6.5. The image catalog of all 72 galaxies is provided in chapter 8.

6 Analysis of eROSITA Data

6.1 Extracting Spectra

The EROPIPELINE script, as described in section 5.2, created eventlists for all 439 galaxies on the German side of the eROSITA sky. These eventlists were generated with 020 processing: including the detections of all 7 TMs under usage of the on-chip filter (if available) within all energy bands (see Table 5.1). Furthermore, the counts of the surveys eRASS1 - eRASS4 have been stacked in order to acquire higher photon statistics. In the following, these eventlists will be used to extract galaxy spectra with SRCTOOL.

SRCTOOL is a software tool that is part of eSASS (MPE, 2023a). It can be used to derive spectra, light-curves and the corresponding instrumental correction vectors/matrices from eROSITA event files. As an input for spectral extraction, it requires the eventlists and source coordinates, as well as the source and background region files that were created in chapter 5. In addition, a source extent model has to be defined, which SRCTOOL uses for effective area calculations. In this work, a TOPHAT model has been used with the radius $\frac{1}{2}(a + b)$, as it is suited for extended sources such as galaxies.

Using this information, SRCTOOL generates single spectra observed with the TMs 1-7, as well as composite spectra from the TMs 1,2,3,4,6 and 5,7, respectively. Since the TMs 5 and 7 don't carry an on-chip filter and are therefore affected by an optical light leak, their observations tend to cause problems in the analysis. For this reason, only the composite spectra of the the TMs 1,2,3,4,6 will be analyzed in this work. In addition to the source spectra, SRCTOOL also generates background spectra from the background region defined by a 100 arcsec thick ring surrounding the elliptical extraction region in a distance of 50 arcsec. Response matrix files (RMFs) and ancillary response files (ARFs), which provide calibration information about the detector response and are required for the correction of the spectra, are also generated by SRCTOOL.

6.2 Background Model

In the vastness of our universe, rich with elements, it is virtually impossible to extract a pure, uncontaminated spectrum. Emission from our ISM is constantly distorting our observations and adding new components to the spectrum. This background emission has to be taken care of to get valid fit results. One method is to observe the background spectrum separately and subtract it from the source spectrum. However, this method does not work with low photon statistics, as the spectral data is left with unproportionally large error bars, making further analysis unfeasible. This is the case for this work.

The second method is to establish and fit a model to the background emission. The model parameters are then frozen to the fitted values, so that new model components can be added for the source spectrum. This way we are left with an already fitted background model and a not-yet-fitted source model. By applying the combined model to our source spectrum, we can now acquire fit results without perturbation by the background emission.

The eROSITA Final Equatorial Depth Survey (eFEDS) survey was first conducted during the eROSITA performance verification phase and later repeated during the all-sky survey program. It covers an area of 142 square degrees, which was observed to a uniform depth of ~ 2.2 ks in 2019 (Brunner et al., 2022). eFEDS therefore offers a unique opportunity to study the properties of the soft X-ray ($0.3 - 0.6$ keV) background (Snowden et al., 1997).

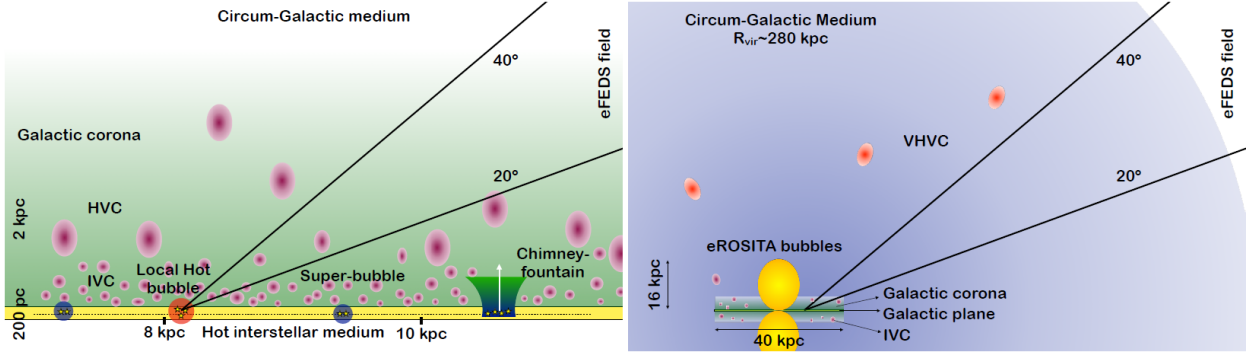


Fig. 6.1: A simplified illustration of the diffuse emission components in the eFEDS field.

Left image: A 100 pc thick Galactic disk is portrayed by a yellow plane. Hot plasma, which is produced in the disk via stellar winds and SN explosions, leads to the inflation of (super-)bubbles. These are marked by blue circles, while the LHB is marked by a red one. When outflows from the disk acquire a sufficient amount of energy to break into the corona, Galactic fountains or chimneys are formed. The corona also contains intermediate and high velocity hydrogen clouds (IVCs and HVCs, displayed as purple ellipses).

Right image: The extent of the Galactic corona, above and below the Galactic disk, is shown in green. In contrast, the CGM extends much further into the halo, as represented by the virial radius of the Milky Way (displayed by the blue sphere). Very high velocity clouds (VHVC, marked by red ellipses) are located within the CGM. The yellow ellipses represent eROSITA bubbles (Ponti et al., 2023).

Ponti et al., 2023, analyzed the spectral characteristics of the integrated soft X-ray emission in the eFEDS field in order to constrain the properties of the Milky Way hot halo emission towards intermediate Galactic latitudes. They observed a flux of 12.6 and $5.1 \cdot 10^{-12}$ erg cm $^{-2}$ deg $^{-2}$ in the total ($0.3 - 2$ keV) and soft ($0.3 - 0.6$ keV) energy bands (*Note: they defined the energy bands differently*). This emission was fitted by a combination of four components: the hot circum-Galactic medium (CGM), the extragalactic Cosmic X-ray background (CXB), the Galactic corona and the unabsorbed emission from the local hot bubble. In addition, they tested the impact of a fifth component: the non-negligible emission of solar wind charge exchange (SWCX). As schematic of the various components of the diffuse emission detected towards the eFEDS field, designed by Ponti et al., 2023, is showcased in Figure 6.1.

In the soft band, the CGM delivers the largest contribution to the background emission, at $\sim 47\%$ of the flux. However, a significant influence due to SWCX is also observed. Since the solar wind flux correlates with solar activity, the contribution of SWCX is intrinsically time-variable. Assuming a SWCX addition of $\sim 15\%$ during solar minimum decreases the

CGM contribution to $\sim 30\%$. The CXB and LHB make up for the remaining part of the flux, at $\sim 33\%$ and $\sim 18\%$, respectively. However, one further component is required to avoid large residuals in the fit. It is believed to originate from the elusive Galactic corona with a possible contribution by stellar sources and adds $\sim 9\%$ to the total flux.

Circum-Galactic Medium

The so-called circum galactic medium describes the gas surrounding our galaxy outside of the disk and extends up to the virial radius of $R \sim 200$ kpc. It is therefore spread over the entire sky and poses the largest contribution to the diffuse background emission. The dominating component of the CGM is believed to be a rarefied plasma, visible in X-rays at approximately the virial temperature of $kT \sim 0.15 - 0.2$ keV.

Assuming that the emission originates from hot plasma in thermal equilibrium, we can describe it by the APEC model in Xspec (Ponti et al., 2023; Smith et al., 2001). It is assumed that the CGM is absorbed by the full column density of Galactic H I as it originates from outside the Galactic disk.

Cosmic X-ray Background

The extragalactic Cosmic X-ray background, as revealed by detailed studies with Chandra, XMM-Newton and ROSAT observations (e.g. Brandt et al., 2022; Luo et al., 2017), consists of a large number of faint, individual sources. Objects that play a major role for this component are distant AGNs, galaxies and galaxy clusters. In fact, these X-ray instruments were able to resolve the origin of $\sim 80\%$ of the CXB flux in the $0.5 - 2$ keV energy range into distinct sources (Luo et al., 2017). This fraction increases to 95% in the $2 - 8$ keV energy band (Liu et al., 2017). The composite emission of these sources resembles a uniform X-ray continuum across the entire sky. At softer energies, below ~ 0.5 keV, the X-ray background seems to be indeed diffuse.

The CXB spectrum can be modelled by a power law of photon index $\Gamma = 1.45$ in the $1 - 10$ keV energy range (Ponti et al., 2023). However, CXB synthesis models that consider the contribution of galaxy groups and clusters point towards a steepening of the CXB slope at energies below ~ 1 keV (Gilli et al., 2007). This can be corrected by fitting a double broken power law (BKN2POW model in Xspec) with a photon index $\Gamma_1 = 1.96$ below 0.6 keV, $\Gamma_2 = 1.75$ between 0.6 keV and 1.2 keV and $\Gamma_3 = 1.45$ above 1.2 keV. Moreover, the CXB is affected by Galactic absorption due to its extra-Galactic nature (Ponti et al., 2023).

Local Hot Bubble

The LHB is a bubble of hot plasma ($kT \sim 0.1$ keV) that surrounds the Sun and extends up to a radius of ~ 200 pc. ROSAT data, which has shown that the soft X-ray background is highly in-homogeneous (Snowden et al., 1997), made it possible to separate the local hot bubble emission from Galactic-scale emission. In the softest band ($E < 0.2$ keV), it dominates over the CXB (Liu et al., 2017). It is assumed that the emission from the LHB can be reproduced by a hot plasma component in thermal equilibrium (APEC model in Xspec) with solar abundances. A temperature of $kT = 0.097$ keV is used in accordance to the work of Liu et al., 2017. The LHB is assumed to be unabsorbed in X-rays as it is located in our

immediate vicinity. (Ponti et al., 2023).

Solar Wind Charge Exchange

A complication arises due to the interaction of solar wind particles with the ISM. Neutral ISM particles constantly pass through the Heliosphere, leading to charge exchange processes with the ionized solar wind particles. These interactions produce diffuse soft X-ray emission (Kuntz et al., 2019), adding a time-variable component to the soft X-ray background. The variability arises due to modulation by the solar wind (Ponti et al., 2023). The SWCX component can be fitted by a solar wind charge exchange model (ACX2 model in Xspec from the atomDB package; Foster et al., 2020). In accordance with the work of Ponti et al., 2023, single recombination and solar abundances are assumed. Furthermore, they suggest a collision speed velocity of 450 km s^{-1} , which resembles the solar wind speed (Ponti et al., 2023). This component is, likewise, not affected by Galactic absorption.

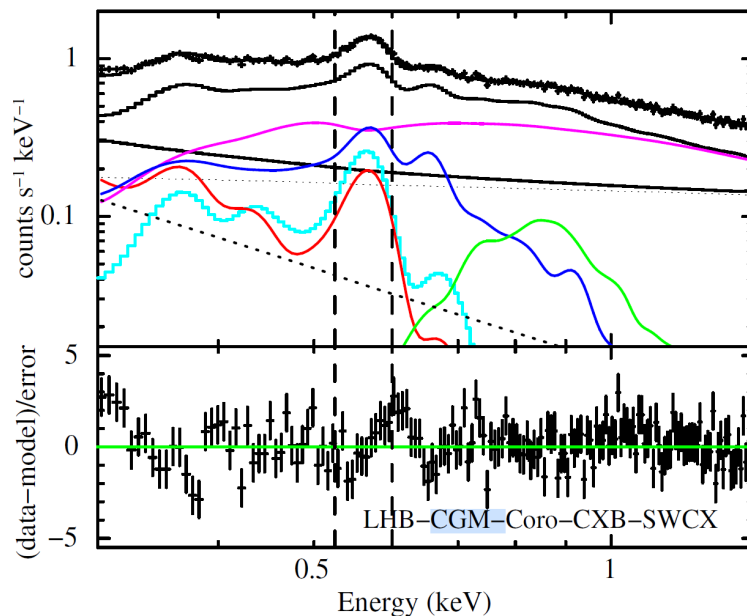


Fig. 6.2: The diffuse emission, which was detected in the eFEDS field during the first two passes of the all sky survey. It was fitted with a five-component model by Ponti et al., 2022. The red, blue, magenta, green and cyan line display the emission from the local hot bubble, the circum-Galactic medium, the Cosmic X-ray background, the Galactic corona and the SWCX, respectively. The black solid line represents the instrumental background and the dotted lines its contributors (Ponti et al., 2023).

Galactic Corona

According to Ponti et al., 2023, the eROSITA data requires an additional Galactic component, as the fit otherwise displays large residuals at energies between 0.7 keV and 1 keV (O VIII line). Ponti et al., 2023, interpreted this thermal component as either a Galactic

corona, produced by a thickened disc, or as the emission from the hot Galactic halo. Unresolved M dwarf stars may also add to this component. It dominates the Galactic-scale emission over the CXB and the LHB at energies between 0.2 keV and 0.6 keV. In accordance with the work of Ponti et al., 2023, the Galactic corona is assumed to be collisionally ionized and in thermal equilibrium, and can therefore be characterized by the APEC model in Xspec. It is assumed to be affected by Galactic absorption, as it is located outside of the Galactic disk. Moreover, Ponti et al., 2023, suggest that this plasma is related to ISM outflows from the Galactic disk, leading to a relatively high metal abundance. Therefore, solar abundances are assumed for this component. The fitted five-component model to the eRASS1 + eRASS2 data in the eFEDS field, performed in the work of Ponti et al., 2023, is displayed in Figure 6.2.

Complete Background Model

The complete background model, designed by the scientist Jonathan Knies at the Dr. Karl Remeis-Observatory in Bamberg based on the work of Ponti et al., 2023, looks as follows:

$$\text{CONSTANT} \times \text{CONSTANT}(\text{ACX2} + \text{APEC} + \text{TBABS}(\text{APEC} + \text{APEC} + \text{BKN2POW}))$$

The Galactic absorption of the CGM and Galactic corona APEC models, as well as the CXB BKN2POW model is described by the Tuebingen-Boulder ISM absorption model (TBABS model in Xspec). The values for the Galactic H I column density depend on the coordinates of the respective galaxy and are acquired from the HI4PI HI survey (HI4PI, 2016). The SWCX ACX2 and LHB APEC models are not affected by Galactic absorption. The spectral shape of the CXB and LHB models is fixed (except for their normalisations) due to the assumptions that were made.

All components are multiplied by 2 constant factors. The first factor used to vary between the values 0.75 and 1.25 to allow for a better calibration between the TMs 1,2,3,4 and 6. For our purposes it was frozen to 1, as no further calibration is required for the already combined spectrum of TMs 1,2,3,4 and 6.

The second factor equals the area of the extraction region in arcmin². This normalization enables the comparison between the source and background spectrum, as well as the comparison of different galaxies.

In the following, this background model will be used as a basis for the spectral analysis of the pre-selected galaxy sample. It has been implemented into Xspec by Jonathan Knies using a PyXspec script, which will be applied and extended for our purposes.

6.3 Source Model

As described in section 3.3, galaxies emit diffuse X-ray emission within and outside of their galactic plane, predominantly in the soft 0.3 – 1.0 keV X-ray band (see Figure 3.1). This emission originates from the hot phase ISM, with contributions from stellar winds, supernova remnants and unresolved stellar sources. It can be investigated by fitting the spectra with thermal plasma models. According to Chandra, XMM-Newton or Suzaku studies (e.g.,

Kavanagh et al., 2020; Kuntz et al., 2010 and references therein) of diffuse X-ray emission in nearby galaxies (e.g. the Magellanic clouds) and our own galaxy, most galaxies are consistent with thermal plasma emission at temperatures of $kT \sim 0.2$ keV. This emission component most likely originates from the hot ISM in equilibrium and unresolved stellar sources.

In addition, many galaxies also display hotter areas such as H II regions, SNRs and superbubbles. The contribution of these regions can be modelled by a second thermal plasma component with a temperature of $kT > 0.5$ keV. However, the X-ray emitting plasma in SNRs is fairly young and has therefore not yet settled in ionization equilibrium. SNR spectra are therefore not only characterized by a temperature, but also by an ionization timescale τ (Hamilton et al., 1983). A frequently used plasma model for SNRs is the constant-temperature, non-equilibrium ionization NEI model (Borkowski et al., 2001b). It describes the equilibration of an impulsively heated postshock gas, which was initially cold, neutral, uniform and homogeneous. The electrons in the shockfront produce the observed X-ray emission through Coulomb collisions with ions. Furthermore, the characteristics of the X-ray emission, the line strengths and, to a smaller degree, the continuum, are also dependant on the heavy-element abundance of the X-ray emitting gas (Borkowski et al., 2001a). The VNEI model in Xspec is an alternate version of the NEI model, which enables the configuration of the H, He, C, N, O, Ne, Mg, Si, S, Ar, Ca, Fe and Ni element abundances. The single ionization timescale τ in this model is defined as the product of the remnant's age t_0 and the post-shock electron number density n_e : $\tau = t_0 \cdot n_e$ (Borkowski et al., 2001a). Strickland et al., 2004a, found, based on observations of edge-on galaxies, that their X-ray emitting gas is filamentary, and rarely with a scale height larger than 1 kpc. According to Tyler et al., 2004, a low scale height and volume filling factor imply that the gas is not in hydrostatic equilibrium.

The aim of this thesis is to model and constrain the parameters of the non-equilibrium, diffuse X-ray emitting gas of nearby galaxies, that was produced by stellar winds and supernova remnants. Due to the low photon statistics of the eROSITA data, it has been decided to retain at one thermal plasma component per galaxy. It is therefore a good approach to fit the source spectrum with the VNEI model. The (initially) free parameters include the plasma temperature kT in keV, the ionization timescale τ in s cm^{-3} and the normalization factor (norm). An extended literature search was conducted to determine the element abundances of the selected galaxies.

In order to account for the intrinsic particle absorption within the respective galaxy, the VNEI component has been multiplied by the Tuebingen-Boulder ISM absorption model with variable elemental abundances (TBVARABS model in Xspec; Wilms et al., 2000). The only free parameter of this model is the hydrogen column density n_{H} towards our line of sight in atoms per cm^2 .

The complete spectral model is therefore given by

$$\text{CONSTANT} \times \text{CONSTANT}(\text{ACX2} + \text{APEC} + \text{TBABS}(\text{APEC} + \text{APEC} + \text{BKN2POW} + \text{TBVARABS}(\text{VNEI}))).$$

6.4 Spectral Analysis

In order to acquire physical parameters for the source spectrum, we have to consider background contributions. As explained in section 6.2, the source and background spectrum can not be separated due to the low photon statistics. Therefore, the background spectrum is modelled first in order to account for the background emission within the source region. Then, the background model is re-normalized to the area of the source region and the fitted parameters are frozen. Afterwards, the source components are added to the model and fitted to the source region.

In addition, we have to consider the particle background, which affects the response of the telescope modules. These effects can be taken into account by applying a filter-wheel-closed (FWC) model onto the detector responses for the source and background spectra. The appropriate FWC model for composite spectra of TMs 1,2,3,4,6 has been acquired from the eROSITA wiki. The normalization of the FWC model was set to 0.1 and fitted to values between 0 and 10.

The Galactic H I column density n_{H} of the TBABS model was acquired from the HI4PI HI survey (HI4PI, 2016) for the coordinates of each galaxy and frozen to the corresponding value in each fit.

Furthermore, average metallicities have been found in the literature for the galaxies NGC 5128, NGC 5236, NGC 300, NGC 1291 and NGC 1313. For those galaxies, all abundances of the VNEI model (except H and He) were set to the determined value (relative to the solar metallicity). For the remaining galaxies, solar abundances are assumed.

The energy range 0.25 – 3 keV was considered for the fits, as the hot plasma mainly emits in the soft X-ray band. Higher energies are highly contaminated by emission from X-ray binaries.

Table 5.2 presents the targets with the best photon statistics (18 galaxies with at ≥ 250 counts). The spectra of all these sources were modelled in Xspec. However, not all fits were successful. After fitting the first couple of galaxies, it was realized that the photon statistics were too bad to conduct the fits with four free parameters n_{H} (TBVARABS model), kT , τ and norm. Except for the most luminous galaxy within the sample, NGC 5128, the fitting algorithm was not able to determine confidence limits for kT and the other parameters. It is possible that the counts of some sources are heavily contaminated by background emission (e.g. NGC 55). In such cases, an even smaller fraction of the counts originates from the source, which is insufficient to confidently constrain physical parameters. This particularly affects close dwarf spheroidal galaxies such as Sculptor, Carina, Bootes I, Sextans DSph and Fornax, as their extraction regions are very large despite of their faint emission. These galaxies were therefore excluded from the spectral analysis.

In order to constrain the confidence intervals of the fit parameters, the degree of variability of the model had to be reduced. It was therefore necessary to freeze the ionization timescale τ and conduct multiple fits for different values of τ , e.g. 10^{11} , 10^{12} and 10^{13} s cm $^{-3}$. It is expected that different τ values will lead to varying results for the plasma temperature kT . The τ value that yields the most significant constraint on kT is considered to represent the best fit to the data. Assuming a particle density of $n = 0.01$ cm $^{-3}$, the τ values 10^{11} , 10^{12} , 10^{13} s cm $^{-3}$ would imply a gas age of $t_0 \sim 3 \cdot 10^5$, $3 \cdot 10^6$, $3 \cdot 10^7$ yrs, respectively.

This method provided adequate fit results for NGC 5128 and NGC 5236. The fit parameters

of the other galaxies remained unconstrained.

An approach was required, which improved the fit to the data prior to the error calculations. In order to adjust the background model to the source region, the previously frozen parameters of the background model were allowed to vary within their 90% confidence range. Parameters, for which the confidence range could not be determined, remained frozen. After fitting the n_{H} and adjusting the background model values to the source region, all parameters except kT and the VNEI norm were frozen in order to reduce the model variability for the error calculation. The FWC model normalizations were frozen to the *BACKSCAL* value given in the source and background spectrum files. These changes significantly improved the fits and yielded reasonable fit results for the galaxies NGC 5128, NGC 5236, NGC 6744, NGC 1291, NGC 300, NGC 1313, NGC 4594, NGC 4945, NGC 4826 and NGC 5068. The results are listed in Table 6.1, including the average metallicity values for NGC 5128, NGC 5236, NGC 300, NGC 1291 and NGC 1313, which were found in the literature. Note: No confidence limits were determined for n_{H} , as the parameter had to be frozen to acquire confidence limits for kT .

Table 5.3 lists the parameters of the remaining galaxies. With less than 250 detected counts, they are very faint and can therefore not be fitted separately. However, it is feasible to acquire average physical parameters by stacking the counts of many faint galaxies and fitting the combined spectra (see section 6.8 for a more detailed explanation). All galaxies were therefore sorted into three groups based on their SFR (see Table 6.2) and an analysis of their stacked spectra has been carried out (see section 6.8).

6.5 Single Spectra

		NGC 5128	NGC 5236	NGC 6744	NGC 1291	NGC 300
Type		S0;Sy2,BLLac	SAB(r)bc;L	SA(s)d	SB(1)0/a	SA(s)d
Distance	(Mpc)	3.75	4.92	8.3	8.8	2.15
Counts	0.25 – 3 keV	6023	1628	844	616	791
Z/Z_{\odot}		0.40 ¹	1.91 ²		0.13 ³	0.41 ⁴
Gal. n_{H}	10^{22} cm^{-2}	0.041	0.041	0.044	0.014	0.094
$\tau = 10^{11}$	kT (keV)	0.367 ^{+0.026} _{-0.023}	0.36 ^{+0.10} _{-0.07}	0.38 ^{+0.31} _{-0.15}	0.56 ^{+0.34} _{-0.23}	0.17 ^{+0.07} _{-0.10}
s cm^{-3}	n_{H}	0.36	$3.9 \cdot 10^{-5}$	0.44	0.19	0.12
	norm	$1.66^{+0.21} \cdot 10^{-5}$	$3.7^{+1.3} \cdot 10^{-7}$	$1.9^{+4} \cdot 10^{-6}$	$1.6^{+1.2} \cdot 10^{-6}$	$3^{+81} \cdot 10^{-6}$
	χ_{red}^2	1.11	1.12	1.11	1.09	1.18
$\tau = 10^{12}$	kT (keV)	0.198 ^{+0.010} _{-0.009}	0.22 ^{+0.04} _{-0.04}	0.18 ^{+0.08} _{-0.04}	0.47 ^{+0.34} _{-0.18}	0.160 ^{+0.023} _{-0.026}
s cm^{-3}	n_{H}	0.40	0.06	0.65	0.05	$3.8 \cdot 10^{-8}$
	norm	$6.7^{+1.3} \cdot 10^{-5}$	$1.3^{+0.5} \cdot 10^{-6}$	$3.0^{+6} \cdot 10^{-5}$	$1.7^{+1.5} \cdot 10^{-6}$	$4.5^{+2.7} \cdot 10^{-6}$
	χ_{red}^2	1.10	1.13	1.10	1.09	1.17
$\tau = 10^{13}$	kT (keV)	0.183 ^{+0.009} _{-0.008}	0.22 ^{+0.04} _{-0.03}	0.18 ^{+0.08} _{-0.04}	0.45 ^{+0.35} _{-0.18}	0.156 ^{+0.022} _{-0.027}
s cm^{-3}	n_{H}	0.49	0.12	0.61	0.05	0.0056
	norm	$1.22^{+0.26} \cdot 10^{-4}$	$2.1^{+0.8} \cdot 10^{-6}$	$2.5^{+5} \cdot 10^{-5}$	$1.7^{+1.7} \cdot 10^{-6}$	$5.1^{+3.2} \cdot 10^{-6}$
	χ_{red}^2	1.11	1.12	1.10	1.09	1.17
		NGC 1313	NGC 4594	NGC 4945	NGC 4826	NGC 5068
Type		SB(s)d	SA(s)a;Sy1.9,L	SB(s)cd;Sy2	SA(rs)ab;Sy2	SB(s)d
Distance	(Mpc)	4.07	9.3	3.8	4.4	5.45
Counts	0.25 – 3 keV	658	652	598	351	270
Z/Z_{\odot}		0.50 ⁵				
Gal. n_{H}	10^{22} cm^{-2}	0.071	0.037	0.14	0.030	0.072
$\tau = 10^{11}$	kT (keV)	0.48 ^{+0.15} _{-0.12}	0.36 ^{+0.19} _{-0.13}	0.72 ^{+0.24} _{-0.21}	0.56 ^{+0.29} _{-0.20}	0.20 ^{+0.5} _{-0.07}
s cm^{-3}	n_{H}	0.23	0.60	1.0	$1.2 \cdot 10^{-15}$	0.86
	norm	$2.4^{+1.0} \cdot 10^{-6}$	$2.7^{+6} \cdot 10^{-6}$	$9.1^{+6} \cdot 10^{-6}$	$2.3^{+1.3} \cdot 10^{-7}$	$7.0^{+34} \cdot 10^{-5}$
	χ_{red}^2	1.20	0.94	1.19	0.99	0.95
$\tau = 10^{12}$	kT (keV)	0.25 ^{+0.06} _{-0.04}	0.20 ^{+0.07} _{-0.05}	0.63 ^{+0.06} _{-0.12}	0.30 ^{+0.16} _{-0.08}	0.34 ^{+0.35} _{-0.12}
s cm^{-3}	n_{H}	0.22	0.77	1.0	$7.1 \cdot 10^{-12}$	0.62
	norm	$7.1^{+4} \cdot 10^{-6}$	$2.1^{+4} \cdot 10^{-5}$	$1.5^{+0.5} \cdot 10^{-5}$	$6^{+4} \cdot 10^{-7}$	$7^{+14} \cdot 10^{-6}$
	χ_{red}^2	1.20	0.94	1.21	1.00	0.95
$\tau = 10^{13}$	kT (keV)	0.26 ^{+0.07} _{-0.04}	0.22 ^{+0.06} _{-0.05}	0.62 ^{+0.12} _{-0.13}	0.29 ^{+0.17} _{-0.07}	0.32 ^{+0.31} _{-0.12}
s cm^{-3}	n_{H}	0.20	0.60	1.0	$1.4 \cdot 10^{-9}$	0.65
	norm	$7.5^{+3.1} \cdot 10^{-6}$	$1.1^{+1.2} \cdot 10^{-5}$	$1.6^{+0.6} \cdot 10^{-5}$	$6.4^{+2.7} \cdot 10^{-7}$	$8^{+21} \cdot 10^{-6}$
	χ_{red}^2	1.20	0.94	1.20	1.00	0.95

Tab. 6.1: Fit parameters of the galaxies NGC 5128, NGC 5236, NGC 6744, NGC 1291, NGC 300, NGC 1313, NGC 4594, NGC 4945, NGC 4826 and NGC 5068 for the ionization timescales $\tau = 10^{11}, 10^{12}, 10^{13} \text{ s cm}^{-3}$. The morphology types were acquired from Vaucouleurs et al., 1991, the distance from Karachentsev et al., 2013, the n_{H} values from HI4PI, 2016 and the average metallicities Z/Z_{\odot} from ¹ Walsh et al., 2012, ² Gazak et al., 2014, ³ Pérez et al., 2006, ⁴ Kudritzki et al., 2008 and ⁵ Hernandez et al., 2022. No average metallicity values were found for NGC 6744, NGC 4594, NGC 4945, NGC 4826 and NGC 5068 in the literature.

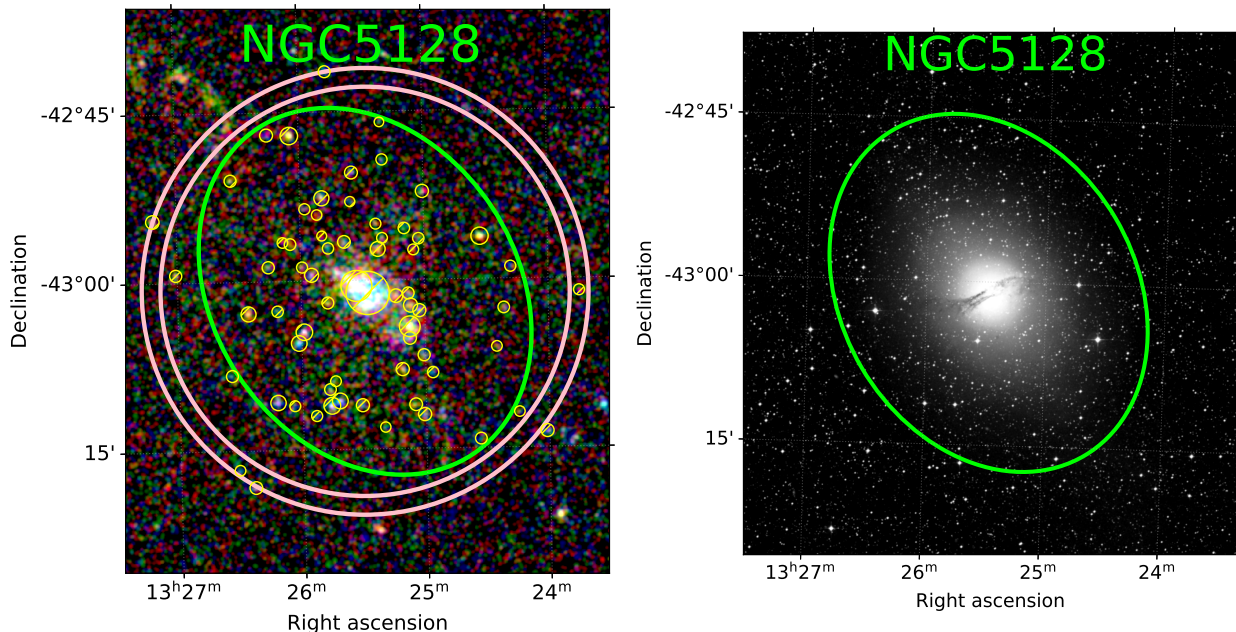
Centaurus A (NGC 5128)

Fig. 6.3: Left side: RGB X-ray image in the 0.2 – 0.7 keV (red), 0.7 – 1.2 keV (green) and 1.2 – 5.0 keV (blue) bands of NGC 5128 from merged eRASS1 - eRASS4 data. Right side: optical image from the STScI Digitized Sky Survey (DSS, 1994). Galaxy parameters: $a = 17.34$ arcmin, $b = 13.52$ arcmin, $\text{dist} = 3.75$ Mpc. Classification: S0-pec;Sy2-BLLAC. See Figure 5.1 for more details.

Cen A, also referred to as NGC 5128, is one of the closest and brightest early-type galaxies to the Milky Way (Dumont et al., 2023). With a distance of roughly 3.8 Mpc (Harris et al., 2010), it provides a unique opportunity to study the structure and evolution of giant elliptical galaxies (Aghdam et al., 2023). It is located in the center of a moderately rich group of galaxies, the Centaurus group, and hosts the most powerful nearby AGN (Salomé et al., 2016), as well as a rich population of GCs and planetary nebulae (Dumont et al., 2023). By comparing the abundances of Cen A’s planetary nebulae with the stellar population, Walsh et al., 2012, suggest an average metallicity of $[\text{Fe}/\text{H}] = -0.4$.

The AGN fuels radio and X-ray bright jets and is surrounded by a ~ 400 pc sized circumnuclear disc (CND; Espada et al., 2019) of dust, gas and young stars (Salomé et al., 2016). Furthermore, CO line detection at SEST revealed molecular gas in the halo up to a distance of ~ 20 kpc from the galaxy center (Charmandaris et al., 2000). ALMA CO(1–0) observations towards the dust lane of Cen A suggest a total molecular gas mass of $1.6 \cdot 10^9 M_{\odot}$ (Espada et al., 2019). While most of the stellar mass in Cen A resembles an old, metal-rich, elliptical galaxy, the peculiar shape and star-forming activity hint towards a recent merger. Furthermore, various halo substructures indicate an ongoing active accretion history (Baade et al., 1954; Wang et al., 2020). It is believed that the gaseous component of Cen A has been replenished during a collision with a H I-rich galaxy some 10^8 yrs ago (Struve et al., 2010). The accreted galaxy now comprises the origin of both the CND and the extended

molecular disk reaching several kpc into Cen A (Espada et al., 2019). This molecular disk also encompasses ionized gas traced by $H\alpha$ (Nicholson et al., 1992), stellar emission in the near-IR (Quillen et al., 1993), as well as dust in the submillimeter (Hawarden et al., 1993) and mid-IR continuum (Mirabel et al., 1999). Archival data from GALEX (FUV) and Herschel (IR) have also shown molecular gas located in filaments in the direction of the jets, with weak star formation ($10^{-5} - 10^{-4} M_{\odot} \text{yr}^{-1}$) on scales of hundreds of parsecs. This is consistent with colour-magnitude diagrams, which indicate jet-induced star formation down to 10 – 15 Myr ago (Salomé et al., 2016). Cen A is also surrounded by stellar shells containing H I gas at a radius of several kpc (J. H. van Gorkom, 1994). The optically bright filaments along the ~ 1.35 kpc long radio jets (Mould et al., 2000) suggest that the ionized gas originates from young stars, however the AGN might also contribute significantly (Morganti et al., 1991). Moreover, the AGN is enclosed in giant radio lobes extending up to ~ 250 kpc (Salomé et al., 2016).

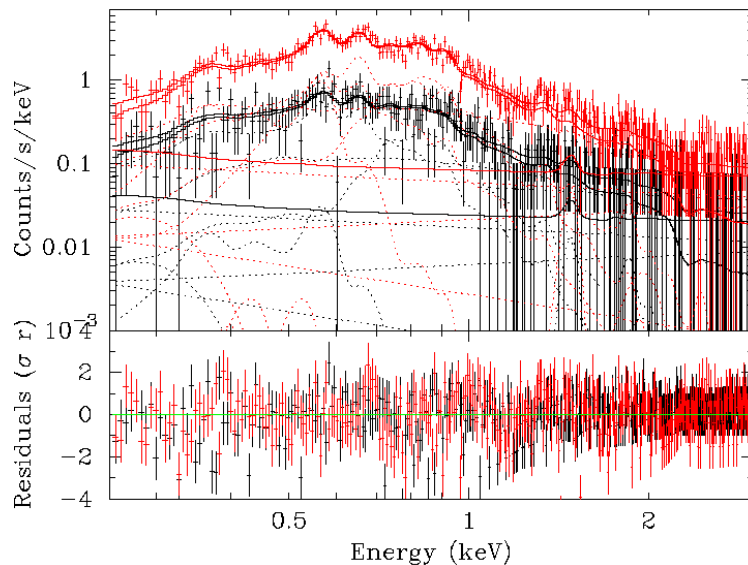


Fig. 6.4: X-ray spectrum of NGC 5128 from merged eRASS1 - eRASS4 surveys under usage of telescopes 1,2,3,4,6 with on-chip filter. Black data points represent the background spectrum, red data points the source spectrum. The solid lines visualize the fits with- and without accounting for the particle background. The dashed lines show the contributions from the different model components.

In a study of long period variable stars and asymptotic giant branch stars, Aghdam et al., 2023, concluded that Cen A experienced three major star formation episodes in the past: 800 Myr, 3.2 Gyr and 10 Gyr ago. The increase of star formation ~ 800 Myr ago agrees with the theory of a recent merger. A lower rate of star formation remained constant for the last ~ 400 Myrs (Aghdam et al., 2023). It is believed that a second, minor merger occurred at that time (Peng et al., 2002). In addition, this star formation could have been fueled by AGN outbursts and jet-induction. It is possible that the interaction with a gas-rich galaxy lead to an increase of AGN activity (Aghdam et al., 2023; H. Mo, 2010). However, the (possibly jet-induced) SFR in the northern filament is only $\sim 0.2\%$ of that in the central

region (Salomé et al., 2016). According to Spitzer mid-IR and GALEX FUV data, the global SFR in Cen A is roughly $1 M_{\odot} \text{yr}^{-1}$ and the global star formation efficiency 0.6Gyr^{-1} with a depletion time of $\tau = 1.5 \text{Gyr}$. However, the SFE value in the CND is lower by a factor of 4 compared to the outer disk, suggesting that mainly central molecular gas will remain in $\sim 1 \text{Gyr}$ (Espada et al., 2019).

The X-ray and optical images of Cen A are displayed in Figure 6.3. One can clearly see the CND as an X-ray bright region around the AGN in the center. In addition, the two jets are visibly stretching towards the lower-right and upper-left corner of the X-ray image. The filaments in the upper-left corner are located beyond the 26.5 mag Holmberg isophote of Cen A.

For the spectral analysis, an average metallicity of $Z/Z_{\odot} = 0.40$ relative to the solar metallicity, derived by Walsh et al., 2012, has been used for the element abundances of the VNEI model (except H and He). The fit parameters are listed in Table 6.1. The resulting values for the temperature kT span between $0.367^{+0.026}_{-0.023} \text{keV}$ and $0.183^{+0.009}_{-0.008} \text{keV}$ depending on the ionization timescale τ .

Messier 83 (NGC 5236)

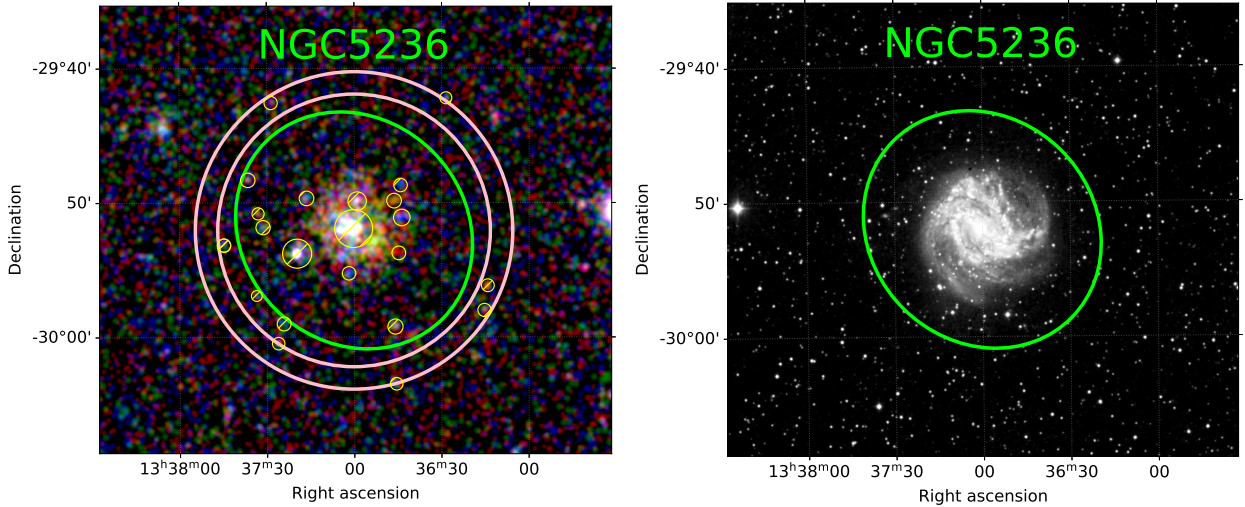


Fig. 6.5: Left side: RGB X-ray image in the 0.2 – 0.7 keV (red), 0.7 – 1.2 keV (green) and 1.2 – 5.0 keV (blue) bands of NGC 5236 from merged eRASS1 - eRASS4 data. Right side: optical image from the STScI Digitized Sky Survey (DSS, 1994). Galaxy parameters: $a = 9.31 \text{ arcmin}$, $b = 8.29 \text{ arcmin}$, $\text{dist} = 4.92 \text{ Mpc}$. Classification: SAB(s)c;HII-Sbrst. See Figure 5.1 for more details.

M83, the "Southern Pinwheel Galaxy" (also named NGC 5236), is a relatively close, nearly face-on (inclination angle $i = 26^\circ$; Koda et al., 2023) barred spiral galaxy at a distance of 4.5 Mpc (Thim et al., 2003). It is also located within the Centaurus group of galaxies (Kiar et al., 2017). With a stellar mass $M_{\text{star}} = 2.5 \cdot 10^{10} M_{\odot}$, slightly smaller than that of the Milky Way (Koda et al., 2023), it is the largest member of the M83 subgroup (Kiar

et al., 2017). The molecular gas mass $m_{\text{H}_2} = 2.6 \cdot 10^9 M_{\odot}$ (Koda et al., 2023) and SFR of $4.2 M_{\odot} \text{yr}^{-1}$ (Leroy et al., 2021) are slightly larger than those of the Milky Way. M83 therefore closely resembles our own galaxy and provides a great opportunity to study grand-design spiral galaxies (Koda et al., 2023). By analyzing the near-infrared flux of super star clusters, Gazak et al., 2014 found a metallicity of $[Z] = (0.28 \pm 0.14)$ dex for M83.

M83 is well-studied across the electromagnetic spectrum. The central star formation is bright in X-rays (Trinchieri et al., 1985), UV (Bohlin et al., 1983), optical and near-IR (Gallais et al., 1991; Rouan et al., 1996), as well as mid-IR (Telesco et al., 1993) and radio (Turner et al., 1994). The emissions in the near-IR are a consequence of the obscuration by large amounts of dust surrounding the M83 center (Gallais et al., 1991; Rouan et al., 1996). According to Eibensteiner et al., 2023, M83 harbors a super-extended H I disk with a radius of ~ 50 kpc. ALMA CO(1-0) imaging of the molecular gas within this disk shows that the locally measured brightness temperature, velocity dispersion, and surface density decrease radially from the center to the outer disk. Coherent large-scale structures can be seen within the molecular gas distribution: a higher concentration towards the center, offset ridges along the bar and prominent spiral arms (Koda et al., 2023). However, a large fraction of the H I in M83 appears to reside outside the Holmberg radius (Huchtmeier et al., 1981).

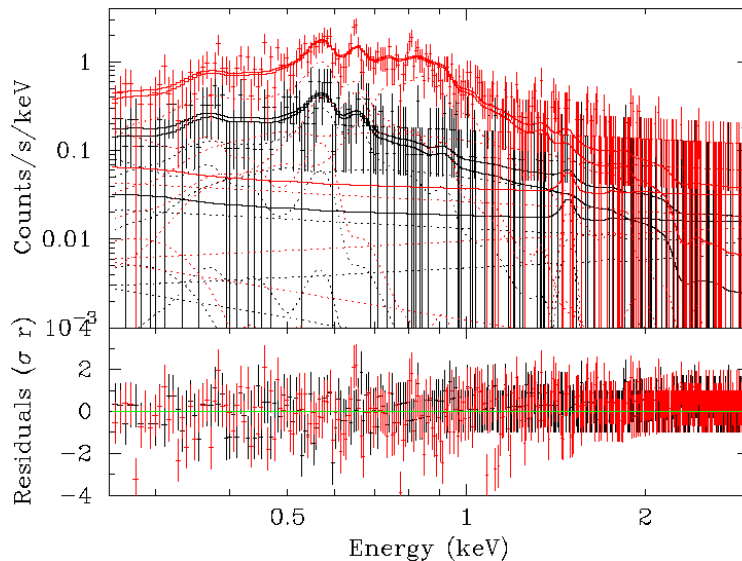


Fig. 6.6: X-ray spectrum of NGC 5236 from merged eRASS1 - eRASS4 surveys. See Figure 6.4 for more details.

Lundgren et al., 2008, created CO gas maps and estimated SFRs based on far-UV, B and H α integrated light. The results point towards an increased SFR in the nuclear region, close to where the bar ends, as well as in the arms of the galaxy. In addition, the SFE appears to be higher along the spiral arms (Silva-Villa et al., 2012b). This is consistent with previous studies indicating an increased star formation activity during the last ~ 10 Myrs (e.g. Knapen et al., 2010; Ryder et al., 1995).

M83 forms a gravitationally bound pair with NGC 5253, a metal-poor dwarf galaxy. As both galaxies are experiencing a high-intensity burst of star formation in their central re-

gions (Conselice et al., 1999), it has been suggested that the starburst was triggered by a collision roughly 1 Gyr ago (Bergh, 1980). Furthermore, Eibensteiner et al., 2023, possibly found a connecting branch between the H I disk and the dwarf irregular galaxy UGCA 365. Petitpas et al., 1998, suggest that the central starburst may be fueled by gas inflow along the bar, accumulating at the inner Lindblad resonance.

The X-ray and optical images of M83 are displayed in Figure 6.5. One can clearly see the X-ray emission of the molecular clouds radially increasing towards the center of the galaxy. The optical image nicely displays the gaseous structure of the grand-design spiral galaxy M83, including the prominent bar and spiral arms. For the spectral analysis, an average metallicity of $Z/Z_{\odot} = 1.91$ relative to the solar metallicity, derived by Gazak et al., 2014, has been used for the element abundances of the VNEI model (except H and He). The fit parameters are listed in Table 6.1. The resulting values for the temperature kT span between $0.36_{-0.07}^{+0.10}$ keV and $0.22_{-0.03}^{+0.04}$ keV depending on the ionization timescale τ .

NGC 6744

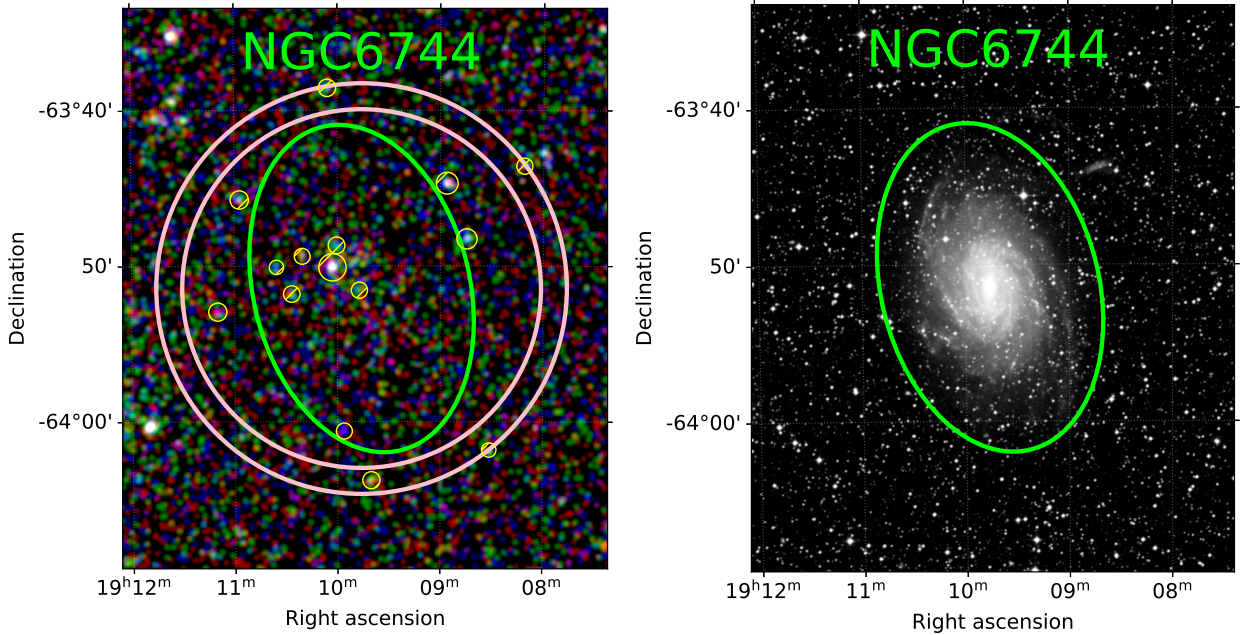


Fig. 6.7: Left side: RGB X-ray image in the 0.2 – 0.7 keV (red), 0.7 – 1.2 keV (green) and 1.2 – 5.0 keV (blue) bands of NGC 6744 from merged eRASS1 - eRASS4 data. Right side: optical image from the STScI Digitized Sky Survey (DSS, 1994). Galaxy parameters: $a = 10.69$ arcmin, $b = 6.95$ arcmin, $\text{dist} = 8.3$ Mpc. Classification: SAB(r)bc-LINER. See Figure 5.1 for more details.

NGC 6744 is one of the largest and most Milky Way-like galaxies in our close vicinity (Talent, 1982). Classified as a type SAB(r)bc barred spiral galaxy, it is located at a distance of 8.5 Mpc in the Pavo group (NASA/IPAC, 2018; Silva et al., 2018). According to Vaucouleurs, 1963, NGC 6744 can be characterized by a bright elliptical nucleus and a central

ring structure. The core is crossed by a relatively weak bar, enclosed in a narrow ring and multiple filamentary arms (Talent, 1982). Although it is morphologically very similar, it is much more isolated than the Milky Way, with the only prominent companion being an irregular dwarf galaxy NGC 6744A (Ryder et al., 1999).

NGC 6744 is an ideal target for studies of the structure and composition of supernova remnants (SNRs) and H II regions. A wide range of multi-frequency observations have been kickstarted after the discovery of SN2005at (Yew et al., 2018). In a combined study of Chandra X-ray, ATCA and MWA radio, as well as WISE infrared observations, Yew et al., 2018, discovered 17 H II regions and determined the SFR of NGC 6744 to be in the range $2.8 - 4.7 M_{\odot} \text{ yr}^{-1}$. According to the PHANGS-ALMA survey (Leroy et al., 2021), the SFR is marginally smaller with a value of $2.4 M_{\odot} \text{ yr}^{-1}$. Although this value is considerably smaller than that of a typical starburst galaxy, it signifies that NGC 6744 is still actively forming stars (Yew et al., 2018). Botticella et al., 2012, estimated a slightly higher value of $3.3 - 6.8 M_{\odot} \text{ yr}^{-1}$ based on H α emission. Further studies include the investigation of the H I disk (Ryder et al., 1999) and the H II regions in the optical band (Ryder, 1995; Talent, 1982). Deep optical images show evidence of an interaction with the dwarf companion NGC 6744A or another host of nearby dwarf galaxies (Ryder et al., 1999). Spectral synthesis points towards a possible merger roughly 1 Gyr ago (Silva et al., 2018).

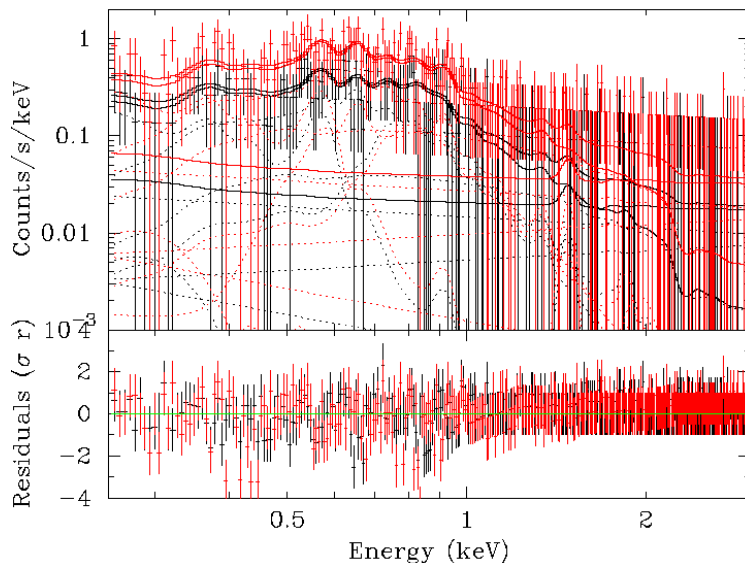


Fig. 6.8: X-ray spectrum of NGC 6744 from merged eRASS1 - eRASS4 surveys. See Figure 6.4 for more details.

Silva et al., 2018, analyzed GMOS data and found that NGC 6744 has a nucleus with emission line ratios typical of Low Ionization Nuclear Emission Line Regions (LINERs) surrounded by three line emitting regions. LINERs are often AGNs and classify a lower ionization degree spectrum compared to Seyferts (Heckman, 1980). Furthermore, HST archival images have shown that the nucleus is associated with a compact blue source, which may resemble the AGN. Emission from the circumnuclear region is likely part of the AGN's extended narrow line region (Silva et al., 2018). The area between the nucleus and the

ring on the other hand is dominated by old stellar populations (Roussel et al., 2001) and has shown little emission in infrared observations taken with the Spitzer telescope. It can therefore be concluded that there is not much star formation going on in this region (Silva et al., 2018). Moreover, Silva et al., 2018, suggest, based on the relative degree of ionization and luminosities in the central regions, that the AGN was brighter in the past and that the remaining emission in the circumnuclear region is merely an echo of its earlier phase.

The X-ray and optical images of NGC 6744 are displayed in Figure 6.7. One can clearly see the bright circumnuclear ring structure in the optical image, with the spiral arms extending from both sides. No metallicity values were found for NGC 6744 in the literature. The fit parameters are listed in Table 6.1. The resulting values for the temperature kT span between $0.38^{+0.31}_{-0.15}$ keV and $0.18^{+0.08}_{-0.04}$ keV depending on the ionization timescale τ .

NGC 1291

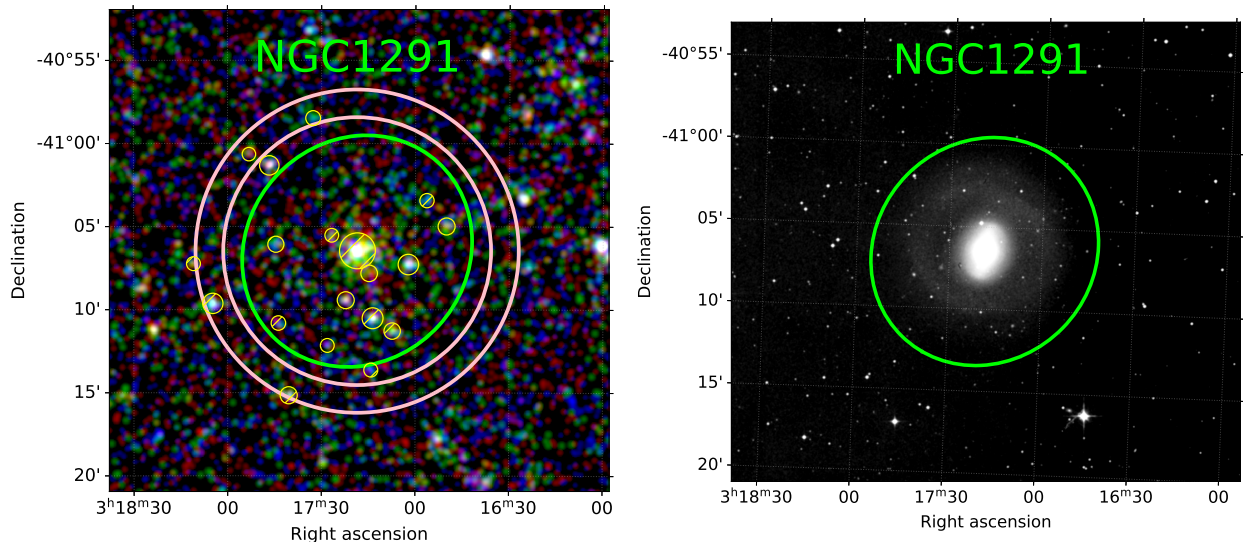


Fig. 6.9: Left side: RGB X-ray image in the 0.2 – 0.7 keV (red), 0.7 – 1.2 keV (green) and 1.2 – 5.0 keV (blue) bands of NGC 1291 from merged eRASS1 - eRASS4 data. Right side: optical image from the STScI Digitized Sky Survey (DSS, 1994). Galaxy parameters: $a = 7.23$ arcmin, $b = 6.65$ arcmin, $\text{dist} = 8.8$ Mpc. Classification: (R_1)SB(1)0/a III. See Figure 5.1 for more details.

NGC 1291 is a lenticular, double-barred galaxy, first studied in detail by Vaucouleurs, 1975. It is located in a distance between 7 and 10.4 Mpc (Kennicutt et al., 2008; Masters, 2005) and is viewed at an inclination angle of $i = (35 \pm 7)^\circ$ (Prescott et al., 2007). NGC 1291 is the first galaxy, in which a large outer ring structure was discovered (Perrine et al., 1922). The ring has a diameter of ~ 16 kpc (Pérez et al., 2006) and contains at least 70% of the total dust mass of the galaxy (Hinze et al., 2012). According to Hinze et al., 2012, who analyzed Herschel images of NGC 1291, this dust is cooler compared to the dust of the inner galaxy, and becomes prominent at wavelengths $\lambda > 160 \mu\text{m}$. NGC 1291 is also easily detected in

the ultraviolet (Thilker et al., 2007). Moreover, in the optical band, NGC 1291 displays a bright inner lens at a radius of ~ 9 kpc, a primary bar, as well as a secondary bar that is misaligned by $\sim 30^\circ$ (Perez et al., 2006; Vaucouleurs, 1975).

Based on WiFeS integrated spectral analysis, Gil et al., 2023, suggest that NGC 1291 underwent a gas-rich merger ~ 9 Gyrs ago, and estimate that the bars developed 6.5 – 8 Gyrs ago, leading to the formation of the outer ring. In present times, the ring is the main site of star formation in NGC 1291 (Bosma et al., 2010), as apparent from GALEX images (Thilker et al., 2007). The star formation of NGC 1291 has been studied via $H\alpha$ emission (e.g. Meurer et al., 2006). Moreover, measurements of the H I content (Driel et al., 1988) have shown that it is mainly concentrated in the outer ring, while the central regions are largely devoid of atomic gas. Despite of that, NGC 1291 is relatively gas-rich for a lenticular galaxy, with a H I mass of $0.81 \cdot 10^9 M_\odot$ (e.g. Li et al., 2011).

Vaucouleurs, 1975, discovered, that the inner bar adheres to the same lens-bar-nucleus pattern pattern as the outer bar, and suggested that the bar structures arised due to dynamical instabilities between the outer and inner disc, such as gas inflow through the outer bar Méndez-Abreu et al., 2019. Such instabilities are believed to be an efficient gas transportation mechanism to the galactic center, leading to the formation of new stellar structures and possibly even feeding AGNs (Méndez-Abreu et al., 2020, and references therein).

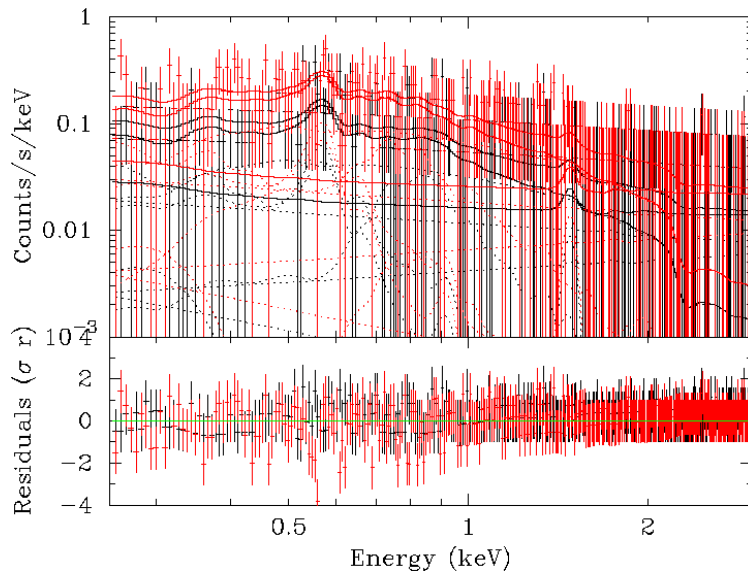


Fig. 6.10: X-ray spectrum of NGC 1291 from merged eRASS1 - eRASS4 surveys. See Figure 6.4 for more details.

X-ray data presented by Bregman et al., 1995, as well as Chandra observations (Hogg et al., 2001; Irwin et al., 2002) confirm the presence of X-ray emitting, hot gas in the central hole of the galaxy. Pérez et al., 2006, argue that the X-ray emission is composed of two components and, with radius, decreases in hardness. This is consistent with the studies of Irwin et al., 2002, which indicate that most of the X-ray emission originates from LMXBs, despite of the presence of a diffuse, hot component. However, the Chandra data yields a metallicity of only $(0.13 \pm 0.04) Z_\odot$ (Pérez et al., 2006) for the X-ray emitting gas in the

central region, whereas optical observations point towards a metallicity of $\sim 1.1 Z_{\odot}$ within the stellar buldge (Terlevich et al., 1981). The origin of the low metallicity gas is therefore hard to explain. Pérez et al., 2006, conducted spectroscopy of NGC 1291 with FORS1 on the ESO VLT at Paranal, and suggest that gas from the outer, gas-rich ring falls to the galactic center due to energy loss induced by bar-driven shocks. During the infall, the gas is accelerated to velocities of $\sim 700 \text{ km s}^{-1}$ and thereby heated to X-ray temperatures. As the inner disc is more metal-rich (Méndez-Abreu et al., 2020), this hypothesis provides an explanation for the significantly lower metallicity of the X-ray emitting gas.

The X-ray and optical images of NGC 1291 are displayed in Figure 6.9. In the optical image, the bars can be seen stretching from the bulge, and the faint outer ring is visibly encircling the galactic center. In the X-ray image, one can clearly see the bright X-ray emitting region in the core of NGC 1291. However, since the X-ray emission in the center mainly originates from LMXBs (Irwin et al., 2002), it has been excluded from the spectrum. This has been done manually, as the source detection algorithm classified it as an extended source.

With a metallicity of only $0.13 Z_{\odot}$ (Pérez et al., 2006), NGC 1291 hosts the lowest-metallicity X-ray emitting gas of our galaxy sample. For the spectral fit, all element abundances of the VNEI model (except H and He) were set to 0.13 (relative to solar). The spectrum of NGC 1291 is displayed in Figure 6.10, the fit results in Table 6.1. The resulting values for the temperature kT span between $0.56_{-0.23}^{+0.34} \text{ keV}$ and $0.45_{-0.18}^{+0.35} \text{ keV}$ (depending on the ionization timescale τ), meaning that the X-ray emitting gas in NGC 1291 is much hotter than in the other galaxies of the sample (except NGC 4945). This is consistent with the hypothesis of Pérez et al., 2006, who argue that the gas is strongly heated during its infall to the galactic center.

NGC 300

With a distance of just 1.88 Mpc (Gieren et al., 2005), NGC 300 is the closest galaxy of the selected sample. It is a nearly face-on spiral galaxy, the brightest one within the Sculptor galaxy group (Butler et al., 2004), and might be gravitationally interacting with the Sculptor galaxy NGC 55 (Read et al., 2001). Since its close proximity and small inclination provide favorable conditions for multiwavelength observations, NGC 300 has been subject to a great deal of studies in the past, including studies of its star formation history (Butler et al., 2004) and stellar populations (Bresolin et al., 2009 and references therein). Moreover, the relatively low Galactic hydrogen column density in the direction of NGC 300 ($n_{\text{H}} = 3.6 \cdot 10^{20} \text{ cm}^{-2}$) makes it a good target for X-ray population studies (Read et al., 2001). The first study of this kind was conducted by Read et al., 2001 between 1991 and 1997, using ROSAT observations. Further studies of the X-ray sources in NGC 300 were performed by Carpano et al., 2005, Binder et al., 2017, Carpano et al., 2018a and Urquhart et al., 2019.

Read et al., 2001, discovered 29 X-ray sources within the disk, several of which appear to be subject to variability. In addition to multiple supernova remnants and H II regions, a supersoft source and a black hole X-ray binary candidate NGC 300 X-1 have been detected. With an X-ray luminosity of $L_{\text{X}} = 2.2 \cdot 10^{38} \text{ erg s}^{-1}$ in the 0.1 – 2.4 keV band, NGC 300 X-1 was the brightest detected X-ray source at the time (Carpano et al., 2018b; Read et al.,

2001). The unresolved emission of NGC 300 on the other hand has an X-ray luminosity of $L_X = 5.8 \cdot 10^{38} \text{ erg s}^{-1}$ in the stated energy range (Read et al., 2001). It makes up roughly $\sim 20\%$ of NGC 300's total X-ray emission and possibly originates from hot, diffuse gas. Read et al., 2001, add, that the data is indicative of many star formation episodes in the past. This idea is supported by more recent studies of NGC 300's young stellar population (Butler et al., 2004). By now, nearly 100 X-ray sources have been detected with an X-ray luminosity $L_X > 10^{36} \text{ erg s}^{-1}$ in the $0.35 - 8 \text{ keV}$ energy range (Binder et al., 2012). The discoveries of supergiants, Wolf-Rayet stars and Cepheids (Butler et al., 2004, and references therein) are signs of recent star formation. However these young stars are mostly found in the galactic disk, while the central region of the galaxy has a relatively small population of stars with ages $t < 1 \text{ Gyr}$, pointing towards suppressed star-forming activity in the last 10^9 yrs (Davidge et al., 1998). According to Binder et al., 2017, the star-forming disk of NGC 300 remained undisturbed in the last $\sim 6 \text{ Gyrs}$, showing no signs of a merger event. Read et al., 2001, compared the X-ray luminosity distribution of NGC 300 with other nearby galaxies, and concluded, due to the lack of unusual properties, that NGC 300 is "quite an unremarkable system", and that "it may be one of the best examples of a completely typical normal quiescent late-type spiral galaxy".

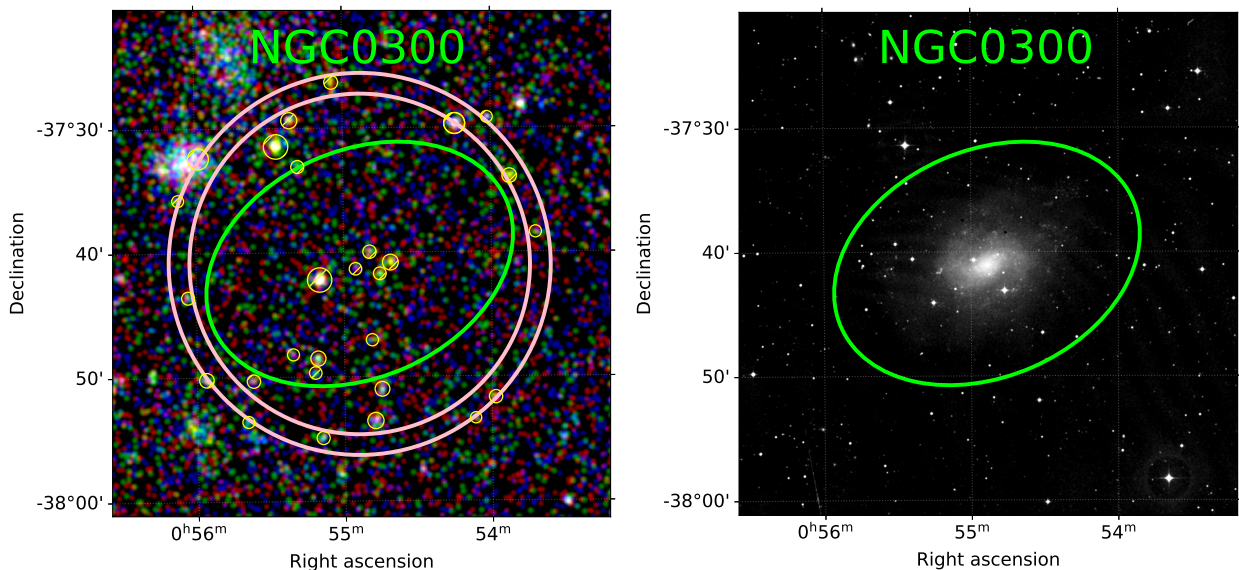


Fig. 6.11: Left side: RGB X-ray image in the $0.2 - 0.7 \text{ keV}$ (red), $0.7 - 1.2 \text{ keV}$ (green) and $1.2 - 5.0 \text{ keV}$ (blue) bands of NGC 300 from merged eRASS1 - eRASS4 data. Right side: optical image from the STScI Digitized Sky Survey (DSS, 1994). Galaxy parameters: $a = 12.85 \text{ arcmin}$, $b = 9.12 \text{ arcmin}$, $\text{dist} = 2.15 \text{ Mpc}$ Classification: SA(s)d. See Figure 5.1 for more details.

However in 2014, a very bright, soft X-ray transient source (CXOU J005440.5-374320) has been detected in a Chandra observation of NGC 300 (Sacchi et al., 2023). With an X-ray luminosity of $L_X \sim 4 \cdot 10^{39} \text{ erg s}^{-1}$, it is classified as an ultraluminous X-ray source (ULX) (Sacchi et al., 2023). It exhibits a 6-hour periodic flux modulation and is subject to recurrent flaring activity. Four outbursts were detected during $\sim 8 \text{ years}$ of follow-up observations

with Chandra, XMM-Newton and the Swift Neil Gehrels Observatory. Sacchi et al., 2023, suggest, that the source is, most likely, either a HMXB system with a Wolf-Rayet star companion, or an interacting system containing a stellar object and an intermediate-mass black hole.

The X-ray and optical images of NGC 300 are displayed in Figure 6.11. The ULX does not appear to be visible in the X-ray image. Based on a spectral analysis of 24 A supergiants, Kudritzki et al., 2008, derived a metallicity of $0.41 Z_{\odot}$ for NGC 300. For the spectral fit, all element abundances of the VNEI model (except H and He) were set to 0.41 (relative to solar). The spectrum of NGC 300 is displayed in Figure 6.12, the fit results in Table 6.1. With kT values between $0.17^{+0.07}_{-0.10}$ keV and $0.156^{+0.022}_{-0.027}$ keV (depending on the ionization timescale τ), the fit for NGC 300 yielded the lowest results for the plasma temperature within the selected galaxy sample.

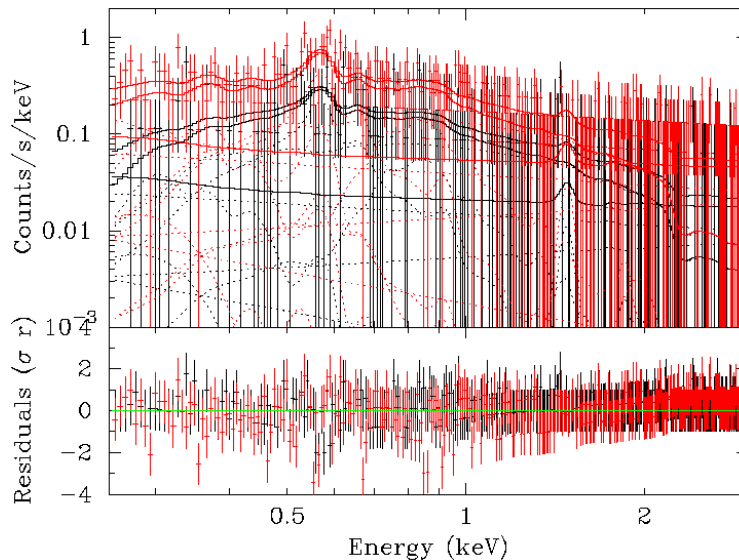


Fig. 6.12: X-ray spectrum of NGC 300 from merged eRASS1 - eRASS4 surveys. See Figure 6.4 for more details.

NGC 1313

NGC 1313, also referred to as the "Topsy Turvy Galaxy", is a slightly inclined ($i = 40.7^\circ$) late-type barred spiral galaxy in a distance of (4.39 ± 0.04) Mpc (Jacobs et al., 2009). According to its classification by Vaucouleurs et al., 1963, it is currently in a transition state between the irregular barred systems SBm and more regular SB(s)c stage. Vaucouleurs et al., 1963, also mentioned its resemblance to the Large Magellanic Cloud.

As to the structure of NGC 1313, optical studies (e.g. Vaucouleurs et al., 1963; Marcellin et al., 1983) have shown that it exhibits a prominent bar and mostly symmetric arms, of which the northern one is brighter (Peters et al., 1994). Some unusual features are found in the south-west of NGC 1313. The stars and H II regions detected in this area are not common for galaxies of its type, leading to speculations of a recent interaction with a satellite galaxy by some authors of the optical studies (Peters et al., 1994). Multiwavelength ob-

servations have revealed the strange physical properties and irregular appearance of NGC 1313, including the shape of the arms and the presence of a bar, and attracted the attention for many following studies (Silva-Villa et al., 2012a).

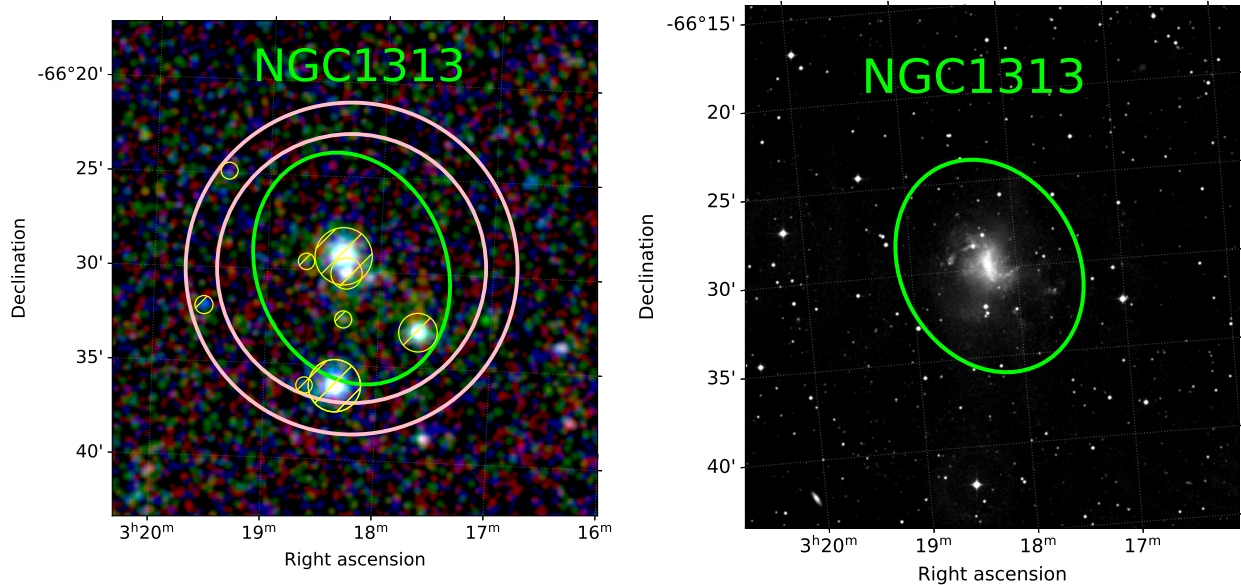


Fig. 6.13: Left side: RGB X-ray image in the energy bands 0.2 – 0.7 keV (red), 0.7 – 1.2 keV (green) and 1.2 – 5.0 keV (blue) of NGC 1313 from merged eRASS1 - eRASS4 data.

Right side: optical image from the STScI Digitized Sky Survey (DSS, 1994).

Galaxy parameters: $a = 6.3$ arcmin, $b = 5.04$ arcmin, $\text{dist} = 4.07$ Mpc.

Classification: SB(s)d-III. See Figure 5.1 for more details.

Based on estimations of the mass-to light ratio M/L , Marcelin et al., 1982, suggest that NGC 1313 is the host of two distinct stellar populations: one in the inner disc, and one in the bar with a 3-10 times smaller M/L . Although NGC 1313 has no apparent close-by companions, Peters et al., 1994, find that the atomic hydrogen distribution and velocity field favor the satellite interaction scenario. In the outer south-west region of the galaxy, where the interaction was suspected, the velocity field is disturbed, and the H I distribution is indicative of hydrogen gas streamers. These streamers are either trailing behind the satellite galaxy or belong to a part of the NGC 1313 plane that has been warped out by the interaction. However, this evidence is insufficient to prove the existence of a satellite galaxy (Peters et al., 1994). Silva-Villa et al., 2012a, argue, that U and H α images of NGC 1313 point towards recent star formation activity in the south-western region, possibly representing the remnant of the tidally disrupted companion (Sandage et al., 1979). The stellar population study of Silva-Villa et al., 2012a, and the acquired star formation histories are in agreement with this claim. In addition, this region shows signs of a population that lacks a connection to the southern arm of the galaxy, when observed in the I and K bands. This population appears to have experienced a recent burst of star formation, possibly being associated with the disrupted satellite galaxy (Silva-Villa et al., 2012a). However, while the south-western

region of the galaxy was subject to increased star forming activity during the last 100 Myrs, the remaining parts of NGC 1313 appear to have had a constant SFR during that time. Silva-Villa et al., 2012a, therefore conclude, that the interaction event caused a local burst of star formation 100 Myrs ago, while leaving the rest of the galaxy unaffected; not strongly increasing the global SFR.

Furthermore, Messa et al., 2021, claim that NGC 1313 has a prominent star cluster population, with 673 star clusters below the age of 300 Myr. The most massive, young star cluster is located within the starburst region of NGC 1313 (e.g. Larsen et al., 2011). The most remarkable X-ray source in NGC 1313, however, is NGC 1313 X-1, a "mysterious" ultraluminous X-ray source that powers a large, bubblelike structure (Palit et al., 2023). The presence of this ionized, gaseous nebula surrounding NGC 1313 X-1, with "abnormally high" $[\text{O I}]\lambda 6300/\text{H}\alpha > 0.1$ ratios (Gúrpidé et al., 2022), points towards powerful outflows and has sparked many extensive studies of NGC 1313 X-1 (e.g. Palit et al., 2023). Palit et al., 2023, suggest, based on a XMM-Newton and NuSTAR analysis of NGC 1313 X-1, that it is likely a black hole accretor with an estimated mass of $(133 \pm 33) M_{\odot}$. Such a massive compact object is on the verge of being classified as an intermediate-mass black hole.

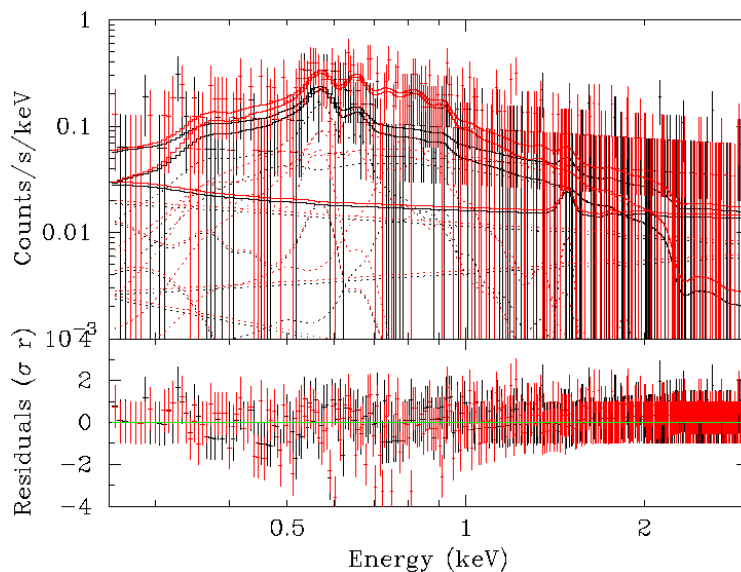


Fig. 6.14: X-ray spectrum of NGC 1313 from merged eRASS1 - eRASS4 surveys. See Figure 6.4 for more details.

The X-ray and optical images of NGC 1313 are displayed in Figure 6.13. The X-ray emission in the south-western region (lower-right) of NGC 1313, where the interaction event took place, appears to be slightly enhanced. The extremely bright region above the center of NGC 1313 coincides with the position of the ultraluminous X-ray source NGC 1313 X-1 and possibly represents the ionized, bubblelike structure. Based on the analysis of young massive clusters, Hernandez et al., 2022, derived a metallicity of $0.50 Z_{\odot}$ for NGC 1313. For the spectral fit, all element abundances of the VNEI model (except H and He) were set to 0.50 (relative to solar). The spectrum of NGC 1313 is displayed in Figure 6.14, the fit results in Table 6.1. The plasma temperature ranges between $0.48^{+0.15}_{-0.12}$ keV and $0.26^{+0.07}_{-0.04}$ keV

(depending on the ionization timescale τ).

Sombrero Galaxy (NGC 4594)

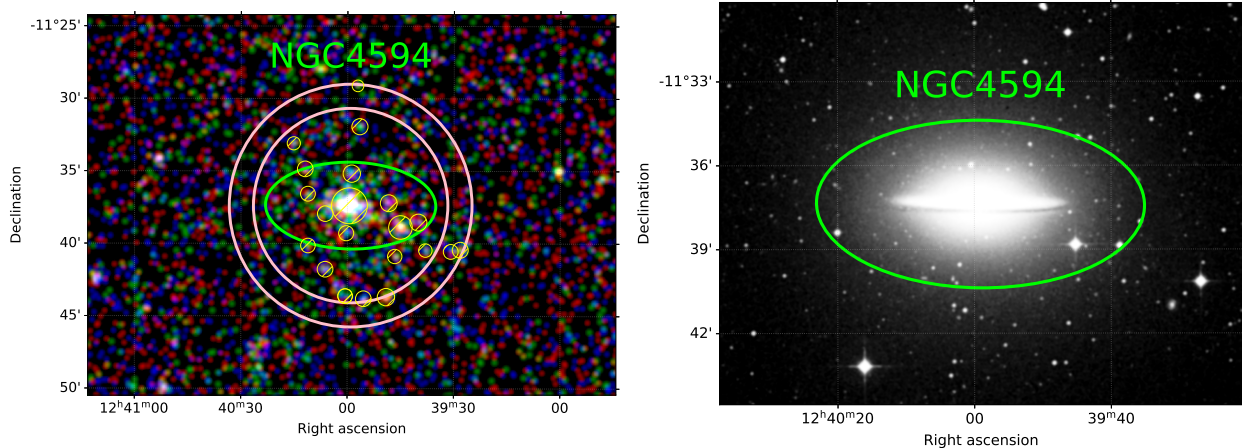


Fig. 6.15: Left side: RGB X-ray image in the 0.2 – 0.7 keV (red), 0.7 – 1.2 keV (green) and 1.2 – 5.0 keV (blue) bands of NGC 4594 from merged eRASS1 - eRASS4 data. Right side: optical image from the STScI Digitized Sky Survey (DSS, 1994). Galaxy parameters: $a = 5.88$ arcmin, $b = 3.0$ arcmin, $\text{dist} = 9.3$ Mpc. Classification: SA(s)a;LINER-Sy1.9. See Figure 5.1 for more details.

NGC 4594 is a famous, early-type spiral galaxy known as the "Sombrero Galaxy". At its nearly edge-on view of $i \sim 79^\circ$ (Jiang et al., 2023), it stands out with a prominent disk, a thick ring of dust and a huge stellar spheroid. Located at a distance of (9.55 ± 0.34) Mpc (McQuinn et al., 2016) in the foreground of the Virgo cluster's southern extension (Tully et al., 1982), it is considered to be the most massive and most luminous galaxy within the Local Volume (Crosby et al., 2024).

The unique morphology of NGC 4594 has sparked large controversies regarding its classification, as multiple features are indicative of NGC 4594 actually being an elliptical or a lenticular galaxy (e.g. Buta et al., 2015). First off, it is very massive. Jiang et al., 2023, and references therein, determined a stellar mass of $M = 2.6 \cdot 10^{11} M_\odot$. For comparison, the stellar mass of the Milky Way is estimated to be $M = 4.6 \cdot 10^{10} M_\odot$ (Licquia et al., 2013). Secondly, with an absolute magnitude of $M_V = -22.4$ mag, NGC 4594 is as bright as M86, a giant elliptical galaxy in the Virgo Cluster (Kang et al., 2022). The huge stellar spheroid, which can be seen in the optical image (Figure 6.15), is, likewise, rather consistent with elliptical galaxies (Gadotti et al., 2012). The metallicity distribution resembles that of Centaurus A; a dominant, metal-rich population and small fraction of metal-poor stars (e.g. Cohen et al., 2020). Lastly, due to the high number of GCs $N_{GC} = 1900 \pm 200$, Rhode et al., 2004, classified NGC 4594 as an S0 elliptical galaxy, while others call it a "mysterious early-type galaxy" (Kang et al., 2022). In any case, NGC 4594's complex structure and interplay between the thick ring of dust, stellar spheroid, and active nucleus inspired many studies across the electromagnetic spectrum.

According to Jiang et al., 2023, NGC 4594 is extremely gas poor, and has a relatively low

SFR ($0.4 M_{\odot} \text{ yr}^{-1}$; Jiang et al., 2023, and references therein) for such a massive galaxy. Furthermore, they calculated the gas supply rate that is required to restore the consumed gas. Based on their findings, they claim that NGC 4594 experienced a starburst stage in the past. On the other hand, Diaz et al., 2018, and J.Kang et al., 2022, suggest that NGC 4594 recently underwent a gas-rich merger, and thereby acquired its unique morphology. The leftover gas after such a merger would provide the fuel for ongoing star formation and growth of the galactic disk (Jiang et al., 2023). However it is also possible that NGC 4594 feasted on many dwarf galaxies. Although it is largely isolated from other host galaxies (Crosby et al., 2024), Karachentsev et al., 2020, found, based on distances and radial velocities, that it hosts 27 group members, mostly dwarf galaxies (e.g. Carlsten et al., 2020). In a recent study using the Subaru Hyper Suprime-Cam, (Crosby et al., 2024), claim to have detected 40 new satellite dwarf galaxies in the sphere of influence of NGC 4594. Such a discovery would make NGC 4594 one of the richest hosts in the Local Volume.

Another bullet point on NGC 4594's CV is that it was one of the first galaxies, in which a central black hole was detected (Jardel et al., 2011). In fact, it hosts one of the nearest low-luminosity active galactic nuclei (LLAGN), which was classified as a low-ionization nuclear emission region based on its optical emission characteristics (Heckman et al., 1989). Jardel et al., 2011, studied the central black hole with axisymmetric, orbit-based models and determined a black hole mass of $(6.6 \pm 0.4) \cdot 10^8 M_{\odot}$. Hada et al., 2013, analyzed the radio structure of NGC 4594 via Very Long Baseline Array observations and found evidence of radio jets powered by the nucleus. At $0.2c$, the intrinsic jet velocity is sub-relativistic; the northern side is approaching, while the southern side is receding (Hada et al., 2013). The presence of a LLAGN with powerful jets was also confirmed by X-ray observations (Pellegrini et al., 2003). Furthermore, measurements of the CO gas rotation velocity indicate that NGC 4594 resides in a massive dark matter halo with $M \sim 10^{13} M_{\odot}$ (Jiang et al., 2023).

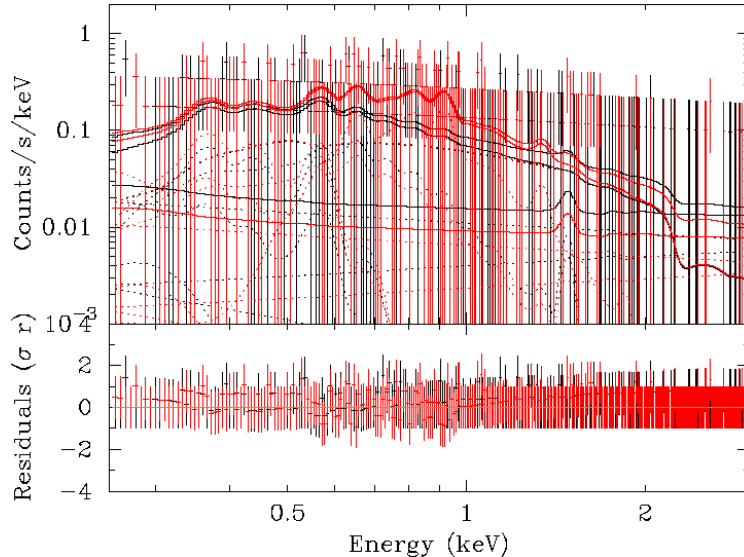


Fig. 6.16: X-ray spectrum of NGC 4594 from merged eRASS1 - eRASS4 surveys. See Figure 6.4 for more details.

The X-ray and optical images of NGC 4594 are displayed in Figure 6.15. The dust ring and

huge stellar spheroid can be clearly seen in the optical image. The X-ray image displays bright X-ray emission in the center of NGC 4594, likely originating from the LLAGN and showing traces of the jets.

The spectrum of NGC 4594 is displayed in Figure 6.16, the fit results in Table 6.1. No average metallicity value was found in the literature; the element abundances were set to solar values. The plasma temperature ranges between $0.36^{+0.19}_{-0.13}$ keV and $0.20^{+0.07}_{-0.05}$ keV (depending on the ionization timescale τ). As expected for an early-type galaxy, the plasma temperature is relatively low.

NGC 4945

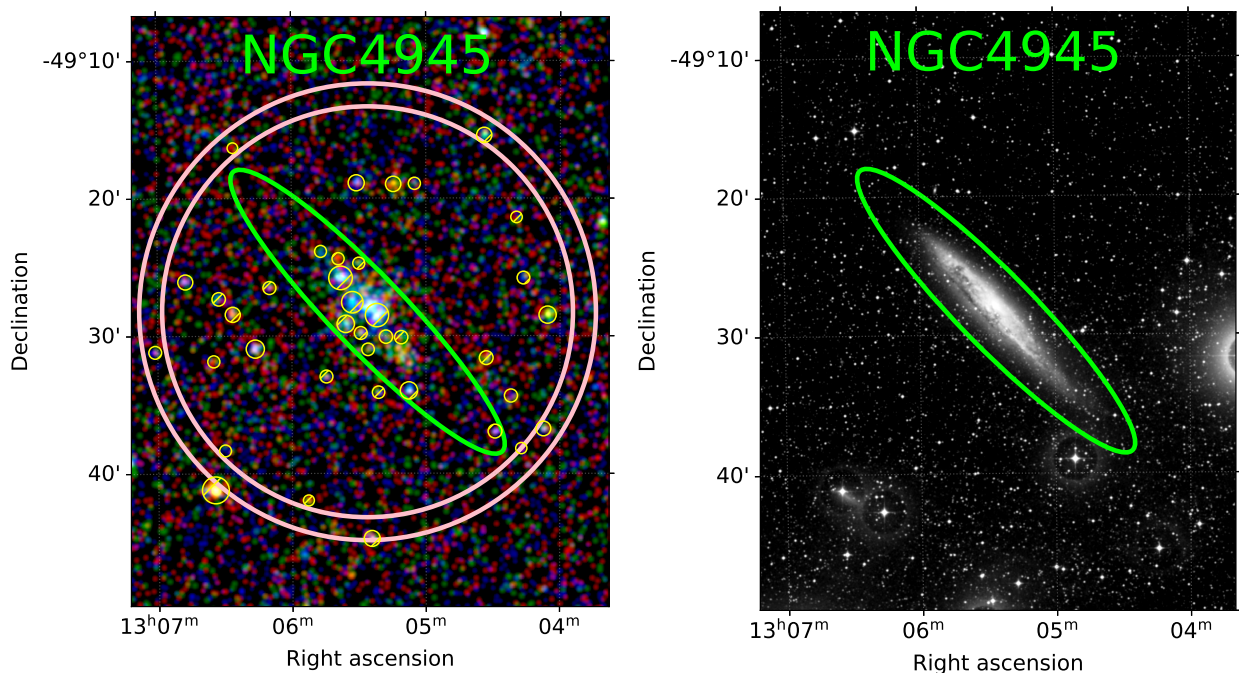


Fig. 6.17: Left side: RGB X-ray image in the 0.2 – 0.7 keV (red), 0.7 – 1.2 keV (green) and 1.2 – 5.0 keV (blue) bands of NGC 4945 from merged eRASS1 - eRASS4 data. Right side: optical image from the STScI Digitized Sky Survey (DSS, 1994). Galaxy parameters: $a = 14.09$ arcmin, $b = 2.68$ arcmin, $\text{dist} = 3.8$ Mpc. Classification: SB(s)cd:-sp-Sy2. See Figure 5.1 for more details.

NGC 4945 is a nearby edge-on ($i = 78^\circ$; Tully et al., 2016) galaxy in the Centaurus A/M83 group (Barrera et al., 2023). At a distance of 3.72 Mpc (Tully et al., 2016), it is one of the closest galaxies that hosts a Seyfert 2 AGN co-existing with a central starburst (Emig et al., 2020). NGC 4945 is one of the brightest sources in the X-ray sky, with a nuclear region very rich in molecular lines, extensively studied across the electromagnetic spectrum (Ianjamasimanana et al., 2022). Using Fe K spectroscopy, Marinucci et al., 2017, has shown that the morphology of NGC 4945 is very complex; probably due to the AGN affecting its nearby environment.

By investigating the extinction in optical and near-infrared images, it becomes apparent

that NGC 4945 faces us with its southwestern rim (Bolatto et al., 2021). Parts of the galaxy located south of the nucleus are therefore heavily obscured by the disk, while the north-western parts are not strongly affected (e.g. Marconi et al., 2000). Marchesi et al., 2018, determined an absorbing column density of $3.8 \cdot 10^{24} \text{ cm}^{-2}$ for NGC 4945. Although heavily obscured, NGC 4945 hosts the brightest Seyfert 2 AGN at energies $> 20 \text{ keV}$ (Itoh et al., 2008), discovered as an X-ray source with variability on timescales of hours (Iwasawa et al., 1993). However, since the primary nuclear emission is completely absorbed, it is only visible through reflected emission below 10 keV (Bellocchi et al., 2020). The central regions of NGC 4945 are even detected in gamma-rays by Fermi, though it is unclear whether the emission is caused by the AGN or star formation activity (Ackermann et al., 2012). Moreover, NGC 4945's nucleus is associated with bright infrared emission, dense molecular clouds, a compact radio source, as well as a bright H_2O megamaser (Greenhill et al., 1997). Through a kinematic analysis of the maser emission, Greenhill et al., 1997, determined a black hole mass of $1.4 \cdot 10^6 M_{\odot}$. Although similar to the black hole mass of the Milky Way, the NGC 4945 nucleus exhibits much larger accretion rates (Bolatto et al., 2021).

Near-infrared images of NGC 4945 show signs of a $\sim 100 \text{ pc}$ scale starburst ring surrounding the nucleus. Bolatto et al., 2021, suggest that the starburst is fed by a bar that is obscured due to the high extinction. Based on 93 GHz radio continuum emission, Bolatto et al., 2021, determined a SFR of $4.3 M_{\odot} \text{ yr}^{-1}$ for the central region of NGC 4945. The global SFR is slightly weaker at $1.5 M_{\odot} \text{ yr}^{-1}$, according to Leroy et al., 2021. Ianjamasimanana et al., 2022 conducted MeerKAT observations of NGC 4945 and found a large amount of H I in the halo (equivalent to 6.8% of the total H I mass). This extra-planar gas was likely driven out of the disk by massive stars and will eventually cool and fall back to spark new episodes of star formation (Ianjamasimanana et al., 2022).

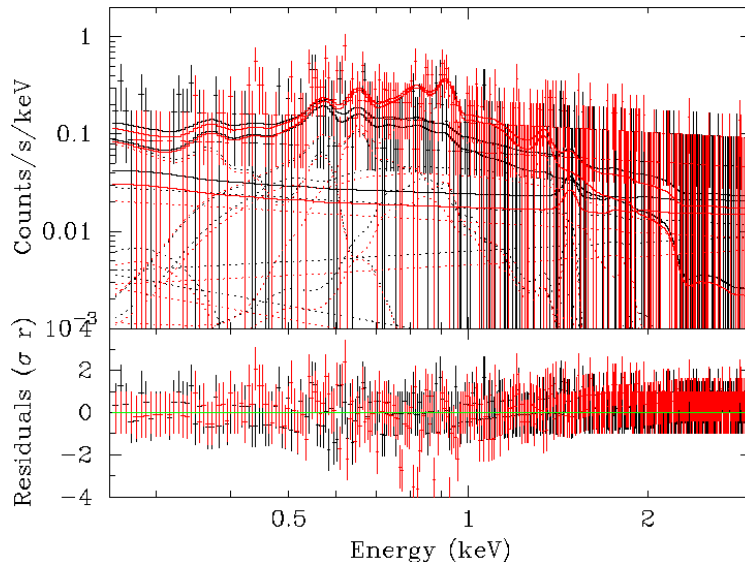


Fig. 6.18: X-ray spectrum of NGC 4945 from merged eRASS1 - eRASS4 surveys. See Figure 6.4 for more details.

Moreover, multiple authors claim that NGC 4945 produces a large-scale outflow of warm

ionized gas along its minor axis (e.g. Mingozi et al., 2019). This outflow has been detected at mm wavelengths, in the optical and in X-rays (Barrera et al., 2023, and references therein), extending out of the galactic plane from $\gtrsim 2''$ (Chandra; Marinucci et al., 2012) to $\sim 30''$ (MUSE/VLT; Venturi et al., 2017). Based on an analysis of Chandra data, Barrera et al., 2023, find that the gas temperature decreases along the outflow and estimate a mass outflow rate of $2.1 M_{\odot} \text{ yr}^{-1}$. According to Bellocchi et al., 2020, mechanical heating, e.g. shocks and turbulence generated by the outflow, dominates the heating of the ISM beyond a distance of 100 pc from the galaxy center. Schurch et al., 2002, analyzed XMM-Newton and Chandra observations of a $3''$ region around the AGN and found three thermal plasma components with temperatures of $(0.60 \pm 0.03) \text{ keV}$, $(0.87 \pm 0.08) \text{ keV}$ and $(6.0 \pm 1.1) \text{ keV}$. Barrera et al., 2023, estimate, that emission from charge exchange contributes 12% to the X-ray flux.

The edge-on nature of NGC 4945 can be viewed in the X-ray and optical images in Figure 6.17, which explains the high extinction in most parts of the galaxy. The X-ray image shows very bright emission in the central regions, produced by the central starburst and the AGN. Some X-ray emission can be traced along the minor axis of NGC 4945, possibly representing the outflow of warm, ionized gas.

The spectrum of NGC 4945 is displayed in Figure 6.18, the fit results in Table 6.1. NGC 4945 is the only galaxy of the sample, for which the n_{H} column density ran against the upper limit of $1.0 \cdot 10^{22} \text{ cm}^{-2}$. This is in agreement with the high extinction values ($3.8 \cdot 10^{24} \text{ cm}^{-2}$, Marchesi et al., 2018) presented in the literature. The spectral analysis of NGC 4945 also yielded the highest plasma temperature values $0.72_{-0.21}^{+0.24} \text{ keV} > kT > 0.62_{-0.13}^{+0.12} \text{ keV}$ (depending on the ionization timescale τ). These results are consistent with the $(0.60 \pm 0.03) \text{ keV}$ thermal plasma component determined by Schurch et al., 2002, and can be explained by the outflow of warm ionized gas from the nucleus, which heats the ISM via shocks and turbulence. The fits were carried out with element abundances set to solar values, as no average metallicity for NGC 4945 was found in the literature.

Black Eye Galaxy (NGC 4826)

The presence of a magnificent dust lane, asymmetrically placed across the prominent bulge, gave rise to many nicknames for NGC 4826. It is more famously known as the "Black-" or "Evil Eye Galaxy". The unique spiral galaxy is located in a distance of 4.4 Mpc (Tully et al., 2013) and hosts two counter-rotating gas rings (Kang et al., 2020). The central region of NGC 4826 is associated with ongoing star-forming activity and several H II regions (Pierini et al., 2002, and references therein). Based on spectroscopic studies (e.g. Alonso-Herrero et al., 2000), it has been classified as a starburst-powered low-ionization nuclear emission-line region (LINER) galaxy.

Using, the IRAM telescope, Casoli et al., 1993, created CO maps of NGC 4826's disk and found that the inner gas ring, which follows the rotation of the galaxy, abruptly ends at a radius of $45 - 50''$ (a small fraction of the galaxy's optical extent). The outer ring counter-rotates the stellar disk (Braun et al., 1992) and extends from $\sim 80''$ to $\sim 9.8'$. Both gas rings have a comparable mass (García-Burillo et al., 2003). Although such structures have previously been detected in elliptical galaxies, NGC 4826 is the first identified spiral galaxy

with counter-rotating subsystems (Saniga et al., 1995).

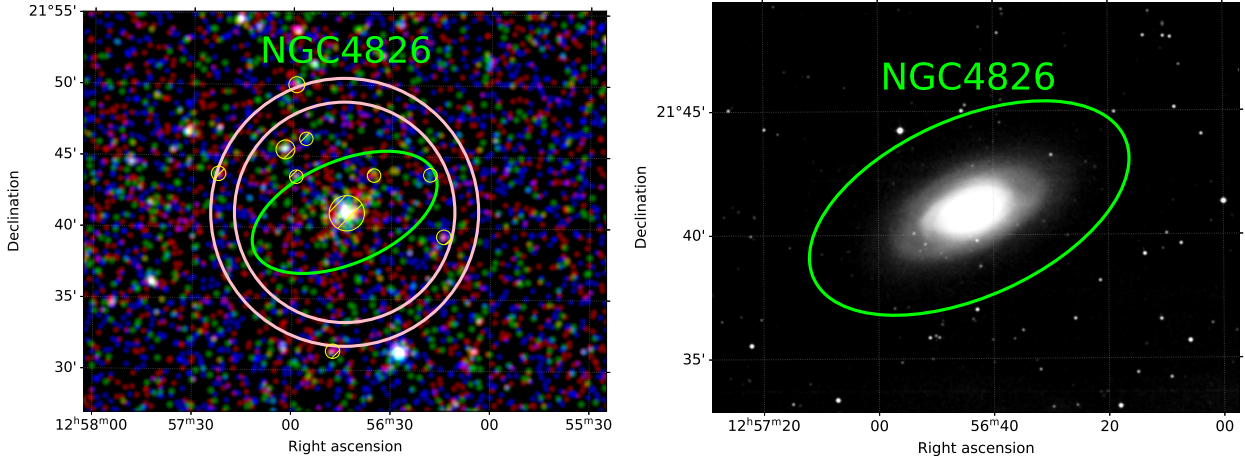


Fig. 6.19: Left side: RGB X-ray image in the 0.2 – 0.7 keV (red), 0.7 – 1.2 keV (green) and 1.2 – 5.0 keV (blue) bands of NGC 4826 from merged eRASS1 - eRASS4 data. Right side: optical image from the STScI Digitized Sky Survey (DSS, 1994). Galaxy parameters: $a = 6.9$ arcmin, $b = 3.59$ arcmin, $\text{dist} = 4.37$ Mpc. Classification: (R)SA(rs)ab;HIISy2. See Figure 5.1 for more details.

By inspecting NICMOS images of NGC 4826, Böker et al., 1999, discovered an inner, arc-shaped region of star formation, as well as a broad lane of bright H II regions (Pierini et al., 2002). Moreover, Kang et al., 2020, found dust lanes, young stars, strong UV emission and a high density of H I gas in multiband images (Watkins et al., 2016). They suggest that the H I distribution extends out to radii of $r \gg 600''$, while the star forming activity is limited to the inner disk region at $r < 200''$. It is believed that the collision of the counter-rotating disks has sparked a burst of star formation at their interface, and possibly even created NGC 4826's famous dust lanes (Braun et al., 1992). Rix et al., 1995, found evidence for strong kinematic disturbance in this region, a rotation velocity approaching zero, and indications of a radial gas inflow along the minor axis.

Although NGC 4826 is an isolated galaxy, known to only host the companion dwarf galaxy NGC 4789A (and a few suggested ones, e.g. Coma P; Brunner et al., 2019), it has been claimed that the recent star formation and high molecular gas content might have been induced by a gas-rich merger roughly 1 Gyr ago (e.g. Rosolowsky et al., 2005; Watkins et al., 2016). In this scenario, the counter-rotating gas disk would have been accreted from the oppositely spinning satellite (e.g. Rubin et al., 1994a). The unusually high H I density ($> 50 M_{\odot} \text{pc}^{-2}$) in the central $r < 0.5$ kpc of NGC 4826 can be explained by a radial gas inflow towards the nucleus; generated by a highly turbulizing merger event (Sil'chenko, 1996). However, NGC 4826's stellar kinematics show little evidence of a recent interaction. It can therefore not be excluded, that NGC 4826 accreted its counter-rotating gas directly from the IGM (Rix et al., 1995). Nevertheless, Brunner et al., 2019, suggests the more likely scenario of a "flyby" interaction with the gas-rich dwarf galaxy Coma P. Smercina et al., 2023, analyzed Subaru Hyper Suprime-Cam observations of NGC 4826 and found evidence for a "spectacular shell feature", as well as further tidal structures that point towards an

ongoing, minor merger event. They estimate a stellar mass $5 \cdot 10^8 M_{\odot}$ and metallicity very similar to the Small Magellanic Cloud (SMC) for the progenitor galaxy. Based on their results, Smercina et al., 2023, claim that this SMC-sized satellite resembles the origin of the counter-rotating gas ring and the inner star-forming disk.

Most importantly, however, Rubin et al., 1994b, renamed NGC 4826 to the "Sleeping Beauty Galaxy" due to its astounding beauty, in the hopes that future astronomers will embrace this title.

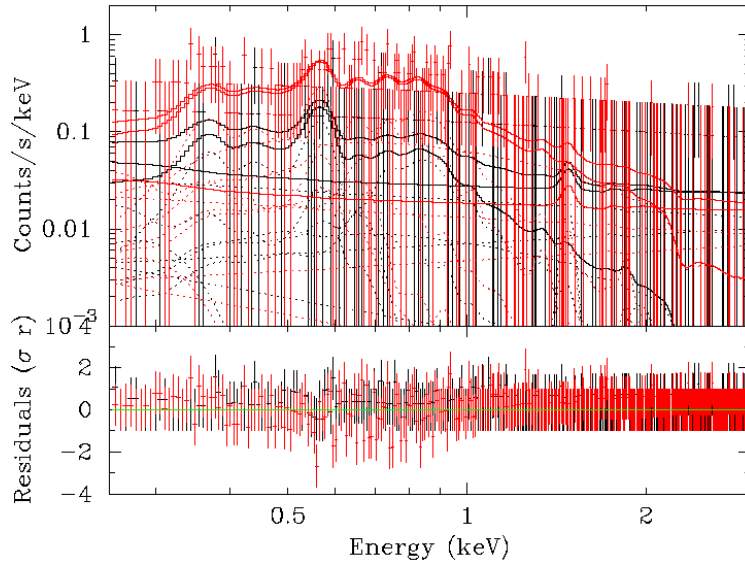


Fig. 6.20: X-ray spectrum of NGC 4826 from merged eRASS1 - eRASS4 surveys. See Figure 6.4 for more details.

The bright nucleus of NGC 4826 can be seen in both the optical and the X-ray images (Figure 6.19). The optical image also displays the counter-rotating disk structures surrounding the nucleus. The spectrum of NGC 4826 is displayed in Figure 6.20, the fit results in Table 6.1. The fits were carried out with element abundances set to solar values, as no average metallicity for NGC 4826 was found in the literature. The spectral analysis yielded plasma temperature values ranging between $0.56^{+0.29}_{-0.20}$ keV and $0.29^{+0.17}_{-0.97}$ keV (depending on the ionization timescale τ). The plasma temperatures are the third-highest of the sample (after NGC 4945 and NGC 1291), which is expected for a starburst galaxy in an ongoing interaction event.

NGC 5068

NGC 5068 is the least well-studied galaxy of the sample. It is a nearby, face-on barred spiral galaxy located at a distance of (5.20 ± 0.22) Mpc (Anand et al., 2021) beyond the Centaurus A group (Karachentsev et al., 2007). It has a moderate stellar mass $M = 2.57 \cdot 10^9 M_{\odot}$ and medium SFR = $0.28 M_{\odot} \text{ yr}^{-1}$ (Leroy et al., 2021).

Healy et al., 2023, have studied MeerKAT observations of NGC 5068 and recognized a complex H I structure resembling clumpy "fingers" at the edge of the star-forming disk. They argue that an interaction with a neighboring galaxy is an unlikely origin scenario for the

outwards extending low-column density gas, as NGC 5068 is an isolated galaxy with the closest neighbor being > 400 kpc away. Since low column density gas appears to be distributed across the whole H I disk, accretion of outer gas from a minor merger seems also unlikely. Instead, due to the clumpiness of the H I gas in the outskirts of the H I disk, they suggest the accretion of cold gas as the origin scenario.

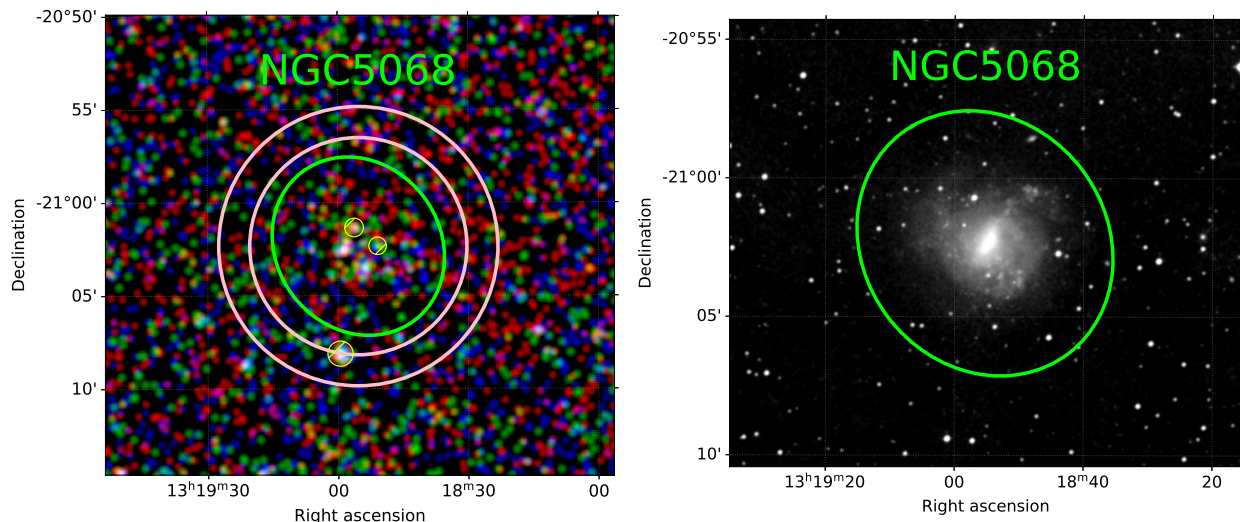


Fig. 6.21: Left side: RGB X-ray image in the 0.2 – 0.7 keV (red), 0.7 – 1.2 keV (green) and 1.2 – 5.0 keV (blue) bands of NGC 5068 from merged eRASS1 - eRASS4 data. Right side: optical image from the STScI Digitized Sky Survey (DSS, 1994). Galaxy parameters: $a = 5.0$ arcmin, $b = 4.4$ arcmin, $\text{dist} = 5.45$ Mpc. Classification: SB(s)d. See Figure 5.1 for more details.

NGC 5068 has also been known to host Wolf-Rayet stars due to their spectroscopic signatures in observations of bright H II regions, conducted by Roas et al., 1986. This has been confirmed by Bibby et al., 2012, who carried out an imaging survey and spectral analysis of NGC 5068 using the narrow-band Very Large Telescope/Focal Reduced Low-dispersion Spectrograph. They identified 160 candidate Wolf-Rayet sources, as well as 28 bright H II regions.

The X-ray and optical images of NGC 5068 are displayed in Figure 6.21. The spectrum is shown in Figure 6.22, the fit results in Table 6.1. The plasma temperature ranges between $0.34^{+0.35}_{-0.12}$ keV and $0.20^{+0.5}_{-0.07}$ keV (depending on the ionization timescale τ). The fits were carried out with element abundances set to solar values, as no average metallicity for NGC 5068 was found in the literature. It is the only galaxy, for which the kT values of the $\tau = 10^{12} \text{ s cm}^{-2}$ and $\tau = 10^{13} \text{ s cm}^{-2}$ fits are higher than for the $\tau = 10^{11} \text{ s cm}^{-2}$ fit. This is likely a consequence of the low photon statistics for NGC 5068, with only 270 detected counts in the 0.25 – 3 keV energy range. The results are accompanied by the largest errors of all fitted galaxies and don't exclude a scenario with the expected hierarchy of kT values. Most importantly, these results show that ~ 270 eROSITA counts approach the minimum amount of counts that is required for the spectral analysis of a galaxy.

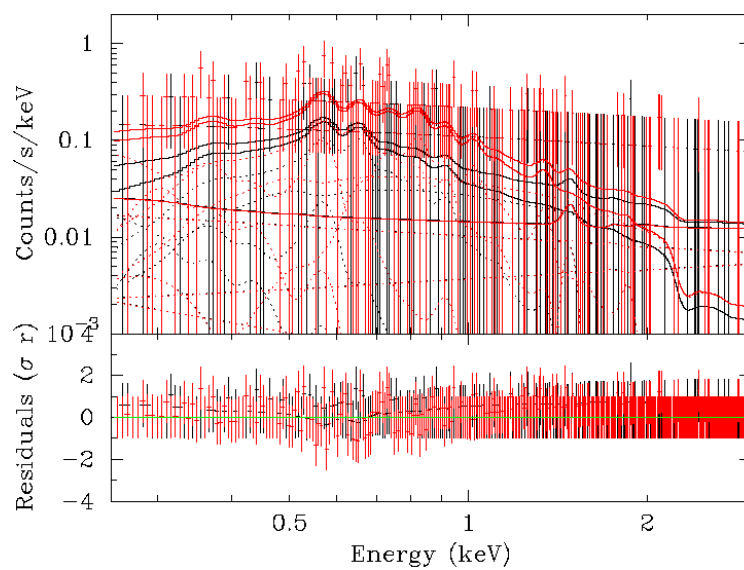


Fig. 6.22: X-ray spectrum of NGC 5068 from merged eRASS1 - eRASS4 surveys. See Figure 6.4 for more details.

6.6 Star Formation Rates

Observations of the Milky Way and nearby galaxies indicate that star formation takes place in clouds of cold gas, mainly due to the presence of molecular hydrogen H_2 . A detailed insight into the molecular gas distribution is therefore crucial for the understanding of galactic evolution (Schruba et al., 2012). The SFR in nearby galaxies is observed to correlate spatially with the distribution of neutral gas. However, the same gas surface density can correspond to substantially different SFRs (Leroy et al., 2008). The SFR of young spiral galaxies is typically higher than that of elliptical or dwarf galaxies (Schruba et al., 2012). In addition, it can vary greatly between the inner and outer parts of the galactic disk.

Understanding the star formation properties of galaxies is crucial, as the SFR is deeply connected to the observed X-ray luminosity L_X . Kouroumpatzakis et al., 2020, derived a linear L_X -SFR relation for the diffuse hot gas in star-forming normal galaxies. This relation is accompanied by a significant scatter, which indicates that L_X also depends on the metallicity of the star-forming gas. The metal abundance has a strong impact on stellar evolution, e.g. the mass-loss rate in stellar winds. As explained in section 3.3, stellar winds, supernova remnants and X-ray binaries are the main production sites of galactic X-ray emission. Lower mass-loss rates lead to the formation of more massive compact objects in X-ray binaries, and therefore a higher L_X .

Due to the importance of understanding galactic star formation properties, an extended literature search has been conducted to constrain the SFRs of our galaxy sample. The search yielded SFR values for 72 out of the 105 galaxies. The results are listed in Table 6.3, Table 6.4 and Table 6.5. The three dwarf spheroidal galaxies Fornax, Sculptor and Sextans dSph were excluded from this analysis, as their close proximity ($d < 0.1 \text{ Mpc}$) leads to a large extraction region and very strong background contamination of their spectra.

The largest fraction of the SFR values, in particular for the high SFR ($\geq 1.0 \text{ M}_\odot \text{ yr}^{-1}$) galaxies, has been retrieved from the PHANGS-ALMA survey (Leroy et al., 2021). Within this project, Leroy et al., 2021, determined the properties of 90 nearby star-forming galaxies by mapping the CO(2-1) emission lines detected with the Atacama Large Millimeter Array (ALMA) radio telescope. As mentioned in section 6.4, it is feasible to acquire average physical parameters by stacking the counts of many faint galaxies and fitting the combined spectra. For this purpose, all galaxies with a retrieved SFR value have been sorted into three groups based on their SFR: high, medium and low SFR (see Table 6.3, Table 6.4 and Table 6.5).

Group	SFR Range
High SFR	$\text{SFR} \geq 1.0 \text{ M}_\odot \text{ yr}^{-1}$
Medium SFR	$1.0 \text{ M}_\odot \text{ yr}^{-1} > \text{SFR} \geq 0.1 \text{ M}_\odot \text{ yr}^{-1}$
Low SFR	$\text{SFR} < 0.1 \text{ M}_\odot \text{ yr}^{-1}$

Tab. 6.2: Galaxy grouping based on their SFR.

The respective ranges of the SFR values are displayed in Table 6.2. The spectra of the galaxies within these three groups have been stacked and further analyzed in section 6.8.

High SFR Galaxies	SFR ($M_{\odot} \text{ yr}^{-1}$)	$\log M/M_{\odot}$	SFR/ M (10^{-10} yr^{-1})	L_{tot} (L_{\odot})	L_{VNEI} (L_{\odot})	r (kpc)	d (Mpc)
Circinus	2.1	10.54	0.606	$7.31 \cdot 10^4$	$7.47 \cdot 10^3$	20.28	4.2
IC 4710	1.3	8.96	14.254	$2.30 \cdot 10^5$	$2.42 \cdot 10^4$	9.23	7.94
IC 5201	1.7	10.36	0.742	$5.52 \cdot 10^5$	$5.98 \cdot 10^4$	21.85	8.8
NGC 2835	1.3	10.63	0.305	$1.08 \cdot 10^6$	$1.16 \cdot 10^5$	28.9	10.3
NGC 2903	3.1	11.13	0.230	$1.29 \cdot 10^6$	$1.31 \cdot 10^5$	32.45	8.87
NGC 3351	1.3	10.81	0.201	$6.41 \cdot 10^5$	$4.53 \cdot 10^4$	21.39	10.05
NGC 3521	3.7	11.32	0.177	$2.03 \cdot 10^6$	$2.12 \cdot 10^5$	34.92	10.7
NGC 3621	1	10.73	0.186	$5.91 \cdot 10^5$	$5.98 \cdot 10^4$	25.02	6.7
NGC 3627	3.9	11.1	0.310	$2.45 \cdot 10^6$	$3.01 \cdot 10^5$	30.58	10.28
NGC 4559	1.1	10.59	0.283	$6.18 \cdot 10^5$	$5.61 \cdot 10^4$	25.37	8.1
NGC 4700	1	9.46	3.467	$4.31 \cdot 10^4$	$3.32 \cdot 10^3$	8.49	7.3
NGC 4945	1.6	11.05	0.143	$4.49 \cdot 10^5$	$1.28 \cdot 10^5$	34.38	3.8
NGC 5128	1.2	11.7	0.024	$5.78 \cdot 10^6$	$9.85 \cdot 10^5$	42.65	3.75
NGC 5236	4.2	11.32	0.201	$3.10 \cdot 10^6$	$2.92 \cdot 10^5$	28.19	4.92
NGC 6744	2.4	11.35	0.107	$5.79 \cdot 10^6$	$4.74 \cdot 10^5$	52.75	8.3

Tab. 6.3: SFRs, distances d , Counts, X-ray luminosities L_X , linear diameters r , masses M and mass-weighted SFRs for the high SFR galaxies. See Table 6.5 for references.

Medium SFR Galaxies	SFR ($M_{\odot} \text{ yr}^{-1}$)	$\log M/M_{\odot}$	SFR/ M (10^{-10} yr^{-1})	L_{tot} (L_{\odot})	L_{VNEI} (L_{\odot})	r (kpc)	d (Mpc)
ESO 300-014	0.15	10	0.150	$4.94 \cdot 10^5$	$3.22 \cdot 10^4$	19.96	9.8
IC 5332	0.41	10.24	0.236	$8.14 \cdot 10^5$	$5.85 \cdot 10^4$	19.05	7.8
NGC 55	0.22	10.15	0.156	$1.48 \cdot 10^5$	$1.03 \cdot 10^4$	21.71	2.13
NGC 300	0.15	10.18	0.099	$3.88 \cdot 10^5$	$4.26 \cdot 10^4$	16.05	2.15
NGC 1291	0.4	9.77	0.679	$2.46 \cdot 10^6$	$2.08 \cdot 10^5$	37.35	8.8
NGC 1313	0.72	10.44	0.261	$4.23 \cdot 10^5$	$5.72 \cdot 10^4$	16.37	4.07
NGC 1637	0.63	10.4	0.251	$3.69 \cdot 10^5$	$2.74 \cdot 10^4$	12.12	9.29
NGC 1744	0.27	10.38	0.113	$5.47 \cdot 10^5$	$3.21 \cdot 10^4$	20.41	10
NGC 2188	0.11	9.45	0.390	$5.64 \cdot 10^4$	$3.98 \cdot 10^3$	9.82	7.4
NGC 2283	0.52	10.39	0.212	$2.30 \cdot 10^5$	$1.23 \cdot 10^4$	14.96	10
NGC 2683	0.33	11.14	0.024	$9.30 \cdot 10^5$	$5.66 \cdot 10^4$	29.52	7.73
NGC 2784	0.13			$1.93 \cdot 10^5$	$1.43 \cdot 10^4$	19.27	9.82
NGC 3239	0.39	10.01	0.381	$2.42 \cdot 10^5$	$1.62 \cdot 10^4$	11.64	7.9
NGC 3344	0.46	10.63	0.108	$5.53 \cdot 10^5$	$4.38 \cdot 10^4$	15.51	6.85
NGC 3368	0.91	11.14	0.066	$1.95 \cdot 10^6$	$1.52 \cdot 10^5$	27.25	10.42
NGC 3432	0.49	10.31	0.240	$2.02 \cdot 10^5$	$1.61 \cdot 10^4$	13.7	9.2
NGC 3593	0.48	10.48	0.159	$3.19 \cdot 10^5$	$2.36 \cdot 10^4$	18.2	10.8
NGC 4136	0.71	10.03	0.663	$2.53 \cdot 10^5$	$2.01 \cdot 10^4$	9.27	7.9
NGC 4204	0.11	9.71	0.214	$2.01 \cdot 10^5$	$9.95 \cdot 10^3$	10.65	8
NGC 4594	0.1	11.76	0.002	$2.53 \cdot 10^6$	$4.45 \cdot 10^5$	32.46	9.3
NGC 4597	0.9	10.07	0.766	$3.60 \cdot 10^5$	$2.59 \cdot 10^4$	16.22	10.1
NGC 4826	0.2	10.7	0.040	$7.13 \cdot 10^5$	$8.38 \cdot 10^4$	17.75	4.37
NGC 5068	0.28	9.94	0.321	$6.79 \cdot 10^5$	$8.29 \cdot 10^4$	17.33	5.45
NGC 5102	0.1	10.11	0.078	$2.02 \cdot 10^5$	$1.69 \cdot 10^4$	13.44	3.4
NGC 5253	0.38	8.91	4.675	$6.79 \cdot 10^4$	$5.50 \cdot 10^3$	7.27	3.56
NGC 7090	0.58	10.26	0.319	$4.39 \cdot 10^5$	$3.27 \cdot 10^4$	19.03	6.7
NGC 7462	0.28	10.06	0.244	$1.51 \cdot 10^5$	$1.29 \cdot 10^4$	15.2	10.1
UGCA 193	0.23	9.57	0.619	$1.43 \cdot 10^4$	$1.46 \cdot 10^3$	11.23	9.7

Tab. 6.4: SFRs, distances d , Counts, X-ray luminosities L_X , linear diameters r , masses M and mass-weighted SFRs for the medium SFR galaxies. See Table 6.5 for references.

Low SFR Galaxies	SFR ($M_{\odot} \text{ yr}^{-1}$)	$\log M/M_{\odot}$	SFR/ M (10^{-10} yr^{-1})	L_{tot} (L_{\odot})	L_{VNEI} (L_{\odot})	r (kpc)	d (Mpc)
DDO 47	$1.00 \cdot 10^{-2}$	9.4	0.040	$3.26 \cdot 10^5$	$2.90 \cdot 10^4$	11.22	8.05
DDO 161	$1.00 \cdot 10^{-2}$	9.67	0.021	$8.29 \cdot 10^4$	$8.44 \cdot 10^3$	16.77	7.3
ESO 115-021	$2.80 \cdot 10^{-2}$	9.5	0.089	$4.21 \cdot 10^4$	$2.64 \cdot 10^3$	9.95	4.99
ESO 238-005	$1.50 \cdot 10^{-2}$	9.18	0.099	$8.39 \cdot 10^4$	$8.94 \cdot 10^3$	6.98	7.8
ESO 269-058	$2.40 \cdot 10^{-4}$	8.77	0.004	$5.15 \cdot 10^4$	$3.30 \cdot 10^3$	5.6	3.8
ESO 274-001	$1.50 \cdot 10^{-2}$	9.96	0.016	$5.66 \cdot 10^4$	$6.22 \cdot 10^3$	14.06	3.09
ESO 324-024	$1.90 \cdot 10^{-2}$	9.06	0.165	$4.48 \cdot 10^4$	$4.37 \cdot 10^3$	3.93	3.73
ESO 325-011	$2.50 \cdot 10^{-3}$	8.4	0.100	$3.08 \cdot 10^4$	$3.08 \cdot 10^3$	3.3	3.4
ESO 383-087	$8.40 \cdot 10^{-3}$	8.36	0.367	$1.03 \cdot 10^5$	$9.87 \cdot 10^3$	5.98	3.45
IC 1959	$4.70 \cdot 10^{-2}$	9.41	0.183	$4.15 \cdot 10^4$	$3.82 \cdot 10^3$	6.84	6.05
IC 4951	$6.50 \cdot 10^{-2}$	9.47	0.220	$5.68 \cdot 10^4$	$3.02 \cdot 10^3$	8.94	9.8
IC 5052	$5.60 \cdot 10^{-2}$	9.97	0.060	$2.05 \cdot 10^5$	$2.10 \cdot 10^4$	13.81	6.03
IC 5152	$3.50 \cdot 10^{-2}$	8.94	0.402	$3.01 \cdot 10^4$	$2.58 \cdot 10^3$	4.07	1.97
Leo A	$6.20 \cdot 10^{-4}$	6.11	4.813	$5.26 \cdot 10^3$	$4.10 \cdot 10^2$	1.35	0.81
NGC 1311	$1.00 \cdot 10^{-2}$	9.02	0.095	$3.93 \cdot 10^4$	$3.55 \cdot 10^3$	6.83	5.2
NGC 3104	$4.00 \cdot 10^{-2}$	9.73	0.074	$4.24 \cdot 10^5$	$2.57 \cdot 10^4$	16.35	16
NGC 3109	$4.00 \cdot 10^{-2}$	9.37	0.171	$2.52 \cdot 10^4$	$2.26 \cdot 10^3$	7.66	1.32
NGC 3115	$2.00 \cdot 10^{-2}$	10.5	0.006	$5.93 \cdot 10^5$	$6.28 \cdot 10^4$	24.04	9.68
NGC 3377	$4.50 \cdot 10^{-3}$			$8.20 \cdot 10^5$	$7.92 \cdot 10^4$	16.95	10.91
NGC 3379	$2.60 \cdot 10^{-2}$			$1.95 \cdot 10^6$	$2.11 \cdot 10^5$	17.86	11.12
NGC 3384	$7.80 \cdot 10^{-3}$			$7.34 \cdot 10^5$	$7.82 \cdot 10^4$	18.09	11.38
NGC 3412	$5.50 \cdot 10^{-3}$			$2.69 \cdot 10^5$	$2.81 \cdot 10^4$	12.09	10.4
NGC 3489	$2.60 \cdot 10^{-2}$	9.69	0.053	$2.01 \cdot 10^5$	$2.01 \cdot 10^4$	13.26	12.08
NGC 4455	$8.50 \cdot 10^{-2}$	9.32	0.407	$9.41 \cdot 10^4$	$6.84 \cdot 10^3$	7.67	8.4
NGC 5264	$2.20 \cdot 10^{-2}$	8.1	1.748	$3.56 \cdot 10^4$	$3.32 \cdot 10^3$	4.69	4.53
Orion D.	$4.00 \cdot 10^{-2}$	9.64	0.092	$6.93 \cdot 10^4$	$4.31 \cdot 10^3$	11.17	6.46
Sextans A	$1.20 \cdot 10^{-2}$	8.4	0.478	$1.10 \cdot 10^4$	$9.86 \cdot 10^2$	2.34	1.32
UGC 5672	$6.30 \cdot 10^{-3}$	9.19	0.041	$1.30 \cdot 10^5$	$5.78 \cdot 10^3$	9.95	11.4
UGC 7321	$6.00 \cdot 10^{-3}$	10.54	0.002	$2.19 \cdot 10^5$	$1.46 \cdot 10^4$	31.02	17.2

Tab. 6.5: SFRs, distances d , Counts, X-ray luminosities L_X , linear diameters r , masses M and mass-weighted SFRs for the low SFR galaxies.

References: Leroy et al., 2021 (IC 5332, NGC 300, NGC 1313, NGC 1637, NGC 2283, NGC 2835, NGC 2903, NGC 3239, NGC 3351, NGC 3489, NGC 3521, NGC 3621, NGC 3627, NGC 4594, NGC 4826, NGC 4945, NGC 5068, NGC 5128, NGC 5236, NGC 6744), Lee et al., 2009a (ESO 115-021, ESO 238-005, ESO 300-014, ESO 324-024, IC 1959, IC 4951, IC 5152, NGC 1744, NGC 2784, NGC 3109, NGC 3368, NGC 3432, NGC 4455, NGC 5264, Sex A, UGC 5672, UGCA 193), Amblard et al., 2014 (NGC 3115, NGC 3377, NGC 3379, NGC 3384, NGC 3412, NGC 3593), Côté et al., 2009 (DDO 161, ESO 269-058, ESO 274-001, ESO 325-011, ESO 383-087), Kennicutt et al., 2003 (IC 4710, NGC 1291, NGC 4594), Heesen et al., 2018 (NGC 55, NGC 7462), Mahajan et al., 2019 (NGC 4042, NGC 4136), Rossa et al., 2008 (NGC 4700, NGC 7090), Guo et al., 2019 (Circinus) Hunter et al., 2004 (DDO 47), Coleman et al., 2008 (Fornax), Elmegreen et al., 2020 (IC 5052), Ryder et al., 1994 (IC 5201), Lešćinskaitė et al., 2022 (Leo A), Eskridge et al., 2010 (NGC 1311), Domgorgen et al., 1997 (NGC 2188), Manna et al., 2023 (NGC 2683), Kewley et al., 2002 (NGC 3104), Padave et al., 2021 (NGC 3344) Vargas et al., 2017 (NGC 4559), Kennicutt, 1983 (NGC 4597), Kaisin et al., 2019 (UGC 4704), Beaulieu et al., 2010 (NGC 5102), Mineo et al., 2012c (NGC 5253), Cannon et al., 2010 (Orion dwarf), Lianou et al., 2012 (Sculptor dwarf), Lee et al., 2009b (SexDSph), Matthews et al., 2003 (UGC 7321).

All galaxies, which had sufficiently good photon statistics for the single spectral analysis, have high or medium SFRs with values ranging between 4.2 and $0.1 M_{\odot} \text{ yr}^{-1}$. This is consistent with the expectation, that high SFR galaxies produce more X-ray emission. The results for the plasma temperature kT , which have been obtained in the single spectral analysis (section 6.4), have been plotted over the SFR values of the corresponding galaxy (Figure 6.23). There seems to be no obvious kT -SFR correlation. This can be explained by the fact, that the galaxies in the selected sample all have medium to high SFRs. That means, that new, hot X-ray emitting gas is regularly supplied by supernova explosions and stellar winds. Since the cooling mechanisms of the X-ray emitting gas are very inefficient, once heated, it will remain at temperatures of $T \sim 10^6$ K for millions of years. The temperature therefore strongly depends on the star formation history and the amount of hot gas that has been produced in the past. For low SFR galaxies, with no active supply of X-ray emitting gas, a lower temperature is expected. Moreover, the results are subject to large uncertainties due to the low photon statistics, causing these small deviations to be less prominent.

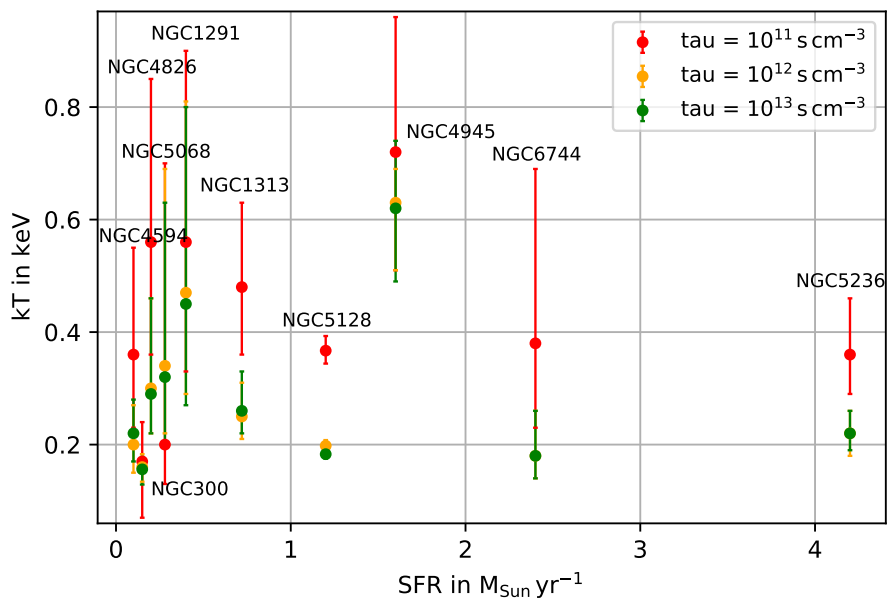


Fig. 6.23: Fitted temperatures kT of the vNEI model plotted over the SFRs for the three values $\tau = 10^{11}, 10^{12}, 10^{13} \text{ s cm}^{-3}$ of the ionization timescale τ .

6.7 The Ionization Timescale

As apparent from Figure 6.23, an ionization timescale of $\tau = 10^{11} \text{ s cm}^{-3}$ typically leads to significantly higher plasma temperature values than $\tau = 10^{12} \text{ s cm}^{-3}$, and $\tau = 10^{12} \text{ s cm}^{-3}$ leads to marginally higher values than $\tau = 10^{13} \text{ s cm}^{-3}$. This is consistent with our expectations, as a higher ionization timescale implies that the gas has had more time to cool down. The galaxies NGC 4594 and NGC 5068 pose the only exceptions to this trend. Their contradicting results are most likely a consequence of the low photon statistics, as the large

uncertainties don't exclude a scenario with the expected hierarchy of kT values. Table 6.6 presents the kT ranges and mean kT values for each τ . The errors were calculated according to Equation 6.1, where $N = 10$ is the number of galaxies in the sample.

$$\Delta\bar{x} = \sqrt{\frac{\sum_{n=1}^N (x_n - \bar{x})^2}{N(N-1)}} + \sqrt{\frac{\sum_{n=1}^N \Delta x_n^2}{N^2}} \quad (6.1)$$

The mean kT value of $0.42_{-0.15}^{+0.17}$ keV for $\tau = 10^{11} \text{ s cm}^{-3}$ is $\sim 45\%$ higher compared to the results for $\tau = 10^{12} \text{ s cm}^{-3}$ and $\tau = 10^{13} \text{ s cm}^{-3}$. With $kT = 0.72_{-0.21}^{+0.24}$ keV, NGC 4945 has the highest plasma temperature. However, the results for $\tau = 10^{11} \text{ s cm}^{-3}$ are also accompanied by significantly larger uncertainties, indicating that $\tau = 10^{11} \text{ s cm}^{-3}$ is an inadequate assumption for the ionization timescale.

The mean kT results of $0.29_{-0.16}^{+0.16}$ keV and $0.29_{-0.18}^{+0.18}$ keV for $\tau = 10^{12} \text{ s cm}^{-3}$ and $\tau = 10^{13} \text{ s cm}^{-3}$ are almost identical. They possess smaller errors and cover a smaller range of plasma temperature values $0.156 \text{ keV} < kT < 0.63 \text{ keV}$. Hence, for $\tau = 10^{12} \text{ s cm}^{-3}$ and $\tau = 10^{13} \text{ s cm}^{-3}$, the results are better constrained and more consistent. For a particle density of $n = 0.01 \text{ cm}^{-3}$, $\tau = 10^{12} \text{ s cm}^{-3}$ corresponds to a gas age of $t_0 \sim 3 \cdot 10^8 \text{ yrs}$ and $\tau = 10^{13} \text{ s cm}^{-3}$ to $t_0 \sim 3 \cdot 10^9 \text{ yrs}$. It can therefore be concluded, that the gas is in collisional ionization equilibrium. The mean kT 's correspond to a plasma temperature of $T = 3.4_{-1.8}^{+1.8} \cdot 10^6 \text{ K}$ and $T = 3.4_{-2.1}^{+2.1} \cdot 10^6 \text{ K}$. However, these are average values which vary strongly between and within galaxies.

$\tau \text{ (s cm}^{-3}\text{)}$	$kT \text{ Range (keV)}$	Mean $kT \text{ (keV)}$
10^{11}	$0.17 < kT < 0.72$	$0.42_{-0.15}^{+0.17}$
10^{12}	$0.16 < kT < 0.63$	$0.29_{-0.16}^{+0.16}$
10^{13}	$0.156 < kT < 0.62$	$0.29_{-0.18}^{+0.18}$

Tab. 6.6: Ranges and mean values of the plasma temperature kT for different values of the ionization timescale τ .

6.8 Stacked Spectra

Motivation

As explained in section 6.4, the bulk of the galaxy sample exhibits insufficient photon statistics for single spectral analysis. For many distant galaxies, the number of detected counts from the source region is too small (see Table 5.3). The spectra of some closer galaxies, in particular nearby dwarfs, have not been successfully fitted despite a large amount of counts; most likely because the spectra are strongly contaminated by background emission.

By stacking the spectra of multiple galaxies, the hot ISM component should become more pronounced and easier to analyze. The significantly improved photon statistics of the stacked spectra are likely to draw a more accurate (average) picture of reality. Therefore, the spectra of all galaxies within their SFR group (see Table 6.3, Table 6.4 and Table 6.5) will be stacked.

Methods

This is done in Python 3.7 by summing the counts in each channel, the exposure times and the extraction areas of both source and background spectra, separately. The ancillary response matrices of each observation have been summed after weighing them by their exposure time. Three stacked spectra have been acquired using this method: a spectrum of 15 high SFR galaxies, one of 28 medium SFR galaxies and one of 29 low SFR galaxies. In the following, these stacked spectra will be modelled in order to acquire average physical parameters for the X-ray emitting gas in galaxies.

Model

Since the bulk of the galaxy sample consists of spiral galaxies with distances up to $d = 17.2$ Mpc, we expect a non-negligible contribution to the spectrum by unresolved X-ray binaries. The source model presented in section 6.3 will therefore receive new components to account for their contamination.

Mineo et al., 2012b, studied the emission from the hot interstellar medium and the populations of high-mass X-ray binaries in a sample of 29 nearby star-forming galaxies using Chandra, Spitzer, GALEX and 2MASS data. They found that, on average, $\sim 30 - 40\%$ of the galaxies' apparent luminosity from diffuse emission in the $0.5 - 2$ keV energy range is produced by faint compact sources, such as HMXBs and LMXBs. By combining the spectra of the detected compact sources, Mineo et al., 2012b, derived an average spectrum of the HMXBs within their sample. The best-fitting model to this spectrum consists of two thermal components and a power law with a slope of $\Gamma = 1.8$ and an intrinsic absorption with a hydrogen column density of $n_{\text{H}} = 4.9 \cdot 10^{21} \text{ cm}^{-2}$. Further models were introduced to fit the spectrum of LMXBs, the combined spectra of CVs and ABs, as well as the spectra of unresolved young faint objects. Similar to the HMXB model, the LMXB model is composed of a power law with a slope of $\Gamma = 1.8$, but with weaker intrinsic absorption ($n_{\text{H}} = 10^{21} \text{ cm}^{-2}$). Due to the low photon statistics of the eROSITA observations, one X-ray binary component must suffice. By introducing a power law with a slope of $\Gamma = 1.8$ and intrinsic absorption described by the TBABS model, both the contributions of HMXBs and LMXBs are taken into consideration. The n_{H} was initially left free to vary in the range $10^{21} \text{ cm}^{-2} < n_{\text{H}} < 4.9 \cdot 10^{21} \text{ cm}^{-2}$, so that a mean value for the HMXB and LMXB models of Mineo et al., 2012b could be determined. However it mostly approached the HMXB value, and was therefore frozen to $4.9 \cdot 10^{21} \text{ cm}^{-2}$. The complete spectral model for the stacked spectra is therefore given by

$$\text{CONSTANT} \times \text{CONSTANT}(\text{ACX2} + \text{APEC} + \text{TBABS}(\text{APEC} + \text{APEC} + \text{BKN2POW} + \text{TBVARABS}(\text{VNEI}) + \text{TBABS}(\text{POWERLAW}))).$$

Analysis

In contrast to the single spectral analysis, the Galactic H I column density n_{H} can not be simply acquired from HI4PI, 2016, as we are dealing with multiple galaxies located towards different directions. In addition, the stacking of multiple spectra eliminates the option of fixing the FWC model normalization to the *BACKSCAL* value. Both parameters will

therefore be fitted.

Since X-ray binaries mainly emit at higher energies ($kT \lesssim 10$ keV for LMXBs and $kT \gtrsim 15$ keV for HMXBs, see section 3.2), it makes sense to consider a larger bandwidth for the fits. That way, a more precise estimate can be acquired for the XRB contribution to the spectrum. Therefore the energy range 0.25 – 6 keV was considered for the fits. Similar to the single spectral analysis, all parameters are frozen for the error calculations, except for the plasma temperature kT and the normalization of the VNEI model (norm).

Results

The fit results for the stacked spectra are presented in Table 6.7. The spectra of the high, medium and low SFR galaxy groups are shown in Figure 6.24, Figure 6.25 and Figure 6.26, respectively.

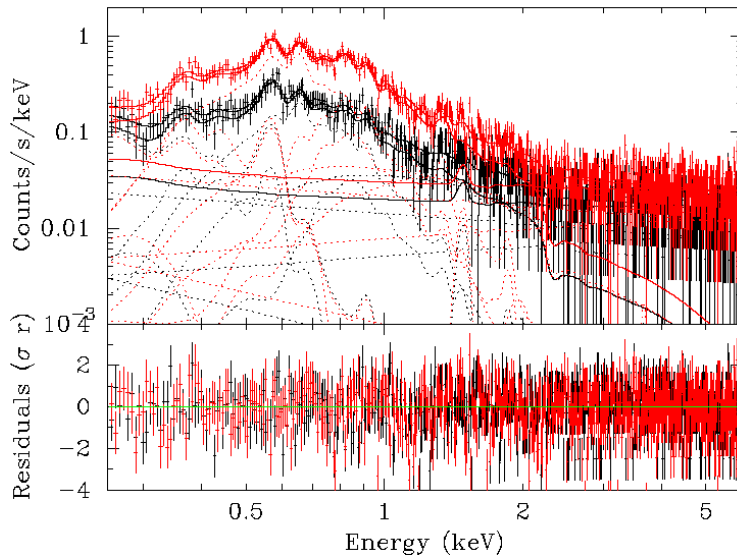


Fig. 6.24: Stacked X-ray spectrum of high SFR galaxies ($\text{SFR} > 1 M_{\odot} \text{yr}^{-1}$) at $\tau = 10^{12} \text{s cm}^{-3}$ from merged eRASS1 - eRASS4 surveys. See Figure 6.4 for more details.

Similar to the single spectral analysis, the plasma temperature kT consistently decreases with the ionization timescale τ for all galaxy groups, as a higher τ implies a higher gas age and hence more time to cool down.

Interestingly, the stacked spectra also don't exhibit a clear $kT - \text{SFR}$ correlation. For $\tau = 10^{11} \text{s cm}^{-3}$, the plasma temperature decreases from $0.43^{+0.07}_{-0.07}$ keV to $0.35^{+0.03}_{-0.07}$ keV for the medium SFR galaxies, and jumps back to $0.43^{+0.08}_{-0.15}$ keV for the low SFR galaxies. However, with temperatures of 0.33 – 0.34 keV, the diffuse gas is, on average, the hottest for the medium SFR galaxies at $\tau = 10^{12} \text{s cm}^{-3}$ and $\tau = 10^{13} \text{s cm}^{-3}$. The high SFR galaxies display a temperature of 0.29 – 0.30 keV, followed by the low SFR galaxies with a temperature of 0.22 – 0.26 keV.

In principle, kT should increase with the SFR, as high star-formation activity leads to

an increased production of X-ray emitting gas via stellar winds and supernova explosions. Galaxies with high SFRs are therefore expected to contain more regions of recently produced, hot gas. This holds true when comparing the high and low SFR galaxies; however, the temperature of the medium SFR galaxies is higher than expected.

		High SFR	Medium SFR	Low SFR
SFR	$M_{\odot} \text{ yr}^{-1}$	$\text{SFR} \geq 1.0$	$1.0 > \text{SFR} \geq 0.1$	$0.1 > \text{SFR}$
Counts	0.25 - 6 keV	11458	6217	1143
$\tau = 10^{11}$	kT (keV)	$0.43^{+0.07}_{-0.07}$	$0.35^{+0.03}_{-0.07}$	$0.43^{+0.08}_{-0.15}$
s cm^{-3}	$n_{\text{H,Gal}}$	0.14	0.10	0.14
	$n_{\text{H,int}}$	0.63	0.53	0.56
	VNEI norm	$5.0^{+1.7}_{-1.0} \cdot 10^{-7}$	$< 1.8 \cdot 10^{-7}$	$< 2.3 \cdot 10^{-7}$
	PL norm	$6.3 \cdot 10^{-8}$	$1.2 \cdot 10^{-8}$	$8.6 \cdot 10^{-9}$
	χ^2_{red}	1.04	1.08	1.14
$\tau = 10^{12}$	kT (keV)	$0.30^{+0.04}_{-0.03}$	$0.34^{+0.08}_{-0.06}$	$0.26^{+0.06}_{-0.11}$
s cm^{-3}	$n_{\text{H,Gal}}$	0.13	0.12	0.14
	$n_{\text{H,int}}$	0.65	0.52	0.60
	VNEI norm	$1.2^{+0.4}_{-0.3} \cdot 10^{-6}$	$< 1.9 \cdot 10^{-7}$	$3.5^{+5}_{-1.9} \cdot 10^{-7}$
	PL norm	$8.9 \cdot 10^{-8}$	$9.1 \cdot 10^{-9}$	$1.0 \cdot 10^{-8}$
	χ^2_{red}	1.04	1.08	1.14
$\tau = 10^{13}$	kT (keV)	$0.29^{+0.04}_{-0.03}$	$0.33^{+0.08}_{-0.06}$	$0.22^{+0.12}_{-0.03}$
s cm^{-3}	$n_{\text{H,Gal}}$	0.13	0.12	0.14
	$n_{\text{H,int}}$	0.71	0.52	0.67
	VNEI norm	$1.5^{+0.5}_{-0.4} \cdot 10^{-6}$	$1.5^{+0.7}_{-0.5} \cdot 10^{-7}$	$6^{+10}_{-5} \cdot 10^{-7}$
	PL norm	$8.6 \cdot 10^{-8}$	$9.3 \cdot 10^{-9}$	$1.0 \cdot 10^{-8}$
	χ^2_{red}	1.04	1.08	1.14

Tab. 6.7: Fit parameters of the stacked spectra for the ionization timescales $\tau = 10^{11}, 10^{12}, 10^{13} \text{ s cm}^{-3}$. The Galactic hydrogen column density $n_{\text{H,Gal}}$ and the intrinsic one of the galaxies $n_{\text{H,int}}$ is given in 10^{22} cm^{-2} .

As explained in section 6.6, the cooling mechanisms of hot plasma are very inefficient, and therefore the star formation history determines the amount of currently available, X-ray emitting gas. Since the medium SFR sample contains almost twice as many galaxies, its total amount of hot gas probably exceeds the high SFR one. By stacking the spectra of 28 galaxies with ongoing star formation, the hot component possibly became more pronounced and increased the average gas temperature.

Moreover, the normalization of the VNEI model component is not well constrained for the medium and low SFR sample; only defined by an upper limit. As the SFR correlates linearly with the X-ray luminosity, less emission is expected to be detected for galaxies with lower SFRs. This implies that a large fraction of the counts is contaminated by background emission and decreases the quality of the photon statistics. With $\text{norm} \lesssim 1.9 \cdot 10^{-7}$, the normalization is the lowest for the medium SFR sample. This indicates that, although the gas is hot, its emission is less prominent compared to the other galaxy groups.

Due to the low star-forming activity of the low SFR galaxies, they have a significantly smaller supply of new hot gas. The previously heated gas is expected to be cooler, as it had

more time to cool down. This is consistent with the relatively low plasma temperature of $0.22 - 0.26 \text{ keV}$ for $\tau = 10^{12} \text{ cm}^{-3}$ and $\tau = 10^{13} \text{ cm}^{-3}$, which is smaller than the mean kT values of the single spectra derived in section 6.7.

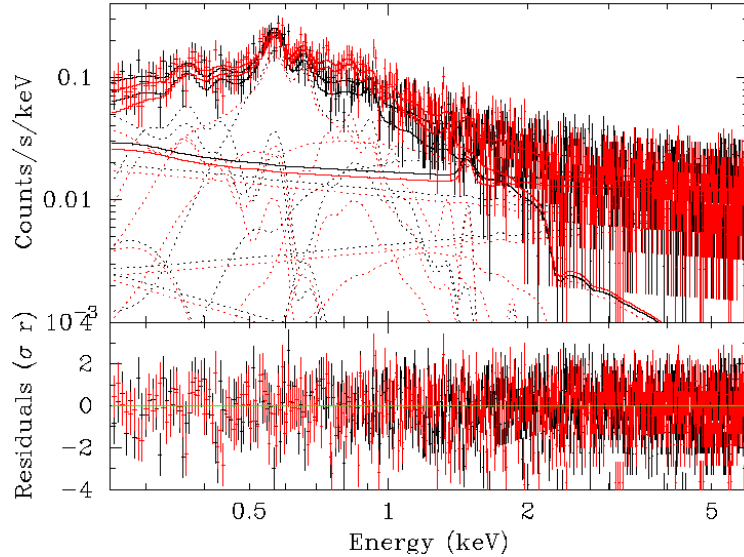


Fig. 6.25: Stacked X-ray spectrum of medium SFR galaxies ($1 M_{\odot} \text{ yr}^{-1} > \text{SFR} > 0.1 M_{\odot} \text{ yr}^{-1}$) at $\tau = 10^{12} \text{ s cm}^{-3}$ from merged eRASS1 - eRASS4 surveys. See Figure 6.4 for more details.

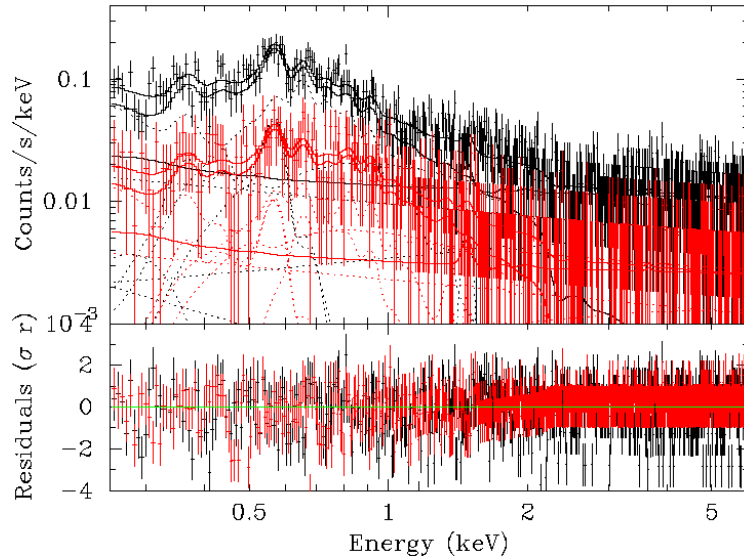


Fig. 6.26: Stacked X-ray spectrum of low SFR galaxies ($0.1 M_{\odot} \text{ yr}^{-1} > \text{SFR}$) at $\tau = 10^{12} \text{ s cm}^{-3}$ from merged eRASS1 - eRASS4 surveys. See Figure 6.4 for more details.

Introducing the X-ray binary component significantly improved the fit for the high SFR spectrum. For the medium and low SFR spectra, the normalizations of the power law model are approximately an order of magnitude smaller compared to the high SFR spectrum. This could be attributed to the fact, that the number of HMXBs and their collective luminosity scales with the SFR of the galaxy, as described by Mineo et al., 2012b. Hence, the spectra of galaxies with lower SFRs should naturally be less contaminated by X-ray binaries.

6.9 Properties and Distribution of Galaxies

In order to acquire a better understanding of the galaxies' properties and distribution in the sky, several parameters have been plotted over the distance. All plots have been color-coded to emphasize possible clustering within a SFR group.

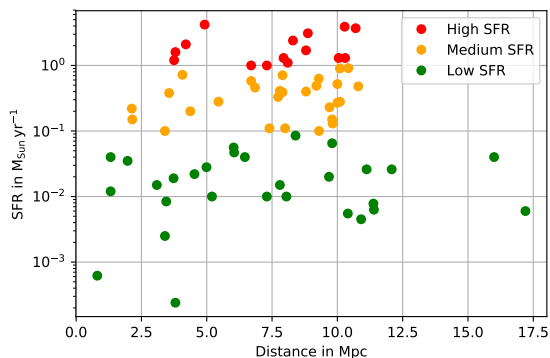


Fig. 6.27: SFR over distance plot. The distances were acquired from Karachentsev et al., 2013. See Table 6.5 for SFR references.

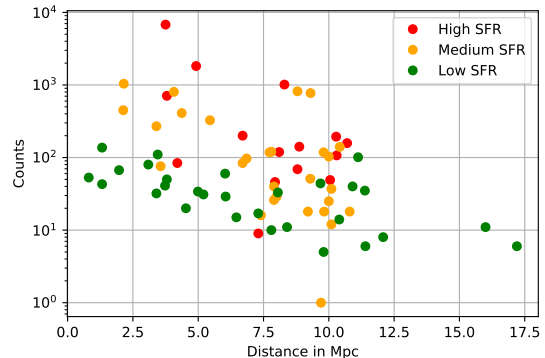


Fig. 6.28: eROSITA counts in 0.25 – 6 keV energy range over distance plot. The distances were acquired from Karachentsev et al., 2013.

Figure 6.27 displays the SFR over distance plot. It can be seen that the high SFR galaxies are all clustered at a distance of 3 – 11 Mpc, while some medium SFR galaxies are located at a distance of just ~ 2 Mpc. The low SFR galaxies exhibit much more scatter in a range of $\sim 0.82 - 17$ Mpc. The closest galaxy is the local group irregular galaxy Leo A, while the most distant one is the spiral galaxy UGC 7321 at a distance of 17.2 Mpc.

The amount of detected eROSITA counts decreases with the distance, as apparent from Figure 6.28. With 6782 detected counts in the 0.25 – 6 keV energy range, NGC 5128 is the brightest galaxy of the sample. For the bulk of the galaxies, between 10 and 1000 counts were detected (including background emission). High SFR galaxies tend to have the best photon statistics, while low SFR galaxies tend to have the lowest. This is consistent with a linear SFR- L_X relation.

Figure 6.29 shows the galaxy distribution based on their mass. The high SFR galaxies tend to have the highest masses with $10^{10} M_\odot < M < 10^{12} M_\odot$ for all but two galaxies. The medium SFR galaxies are mostly clustered between $10^9 M_\odot$ and $10^{11} M_\odot$, while the low SFR galaxies generally have masses $M < 10^{10} M_\odot$ (with only 2 exceptions). Leo A is the

least massive galaxy with a mass of $M \sim 10^6 M_{\odot}$. Only one galaxy with $M < 10^9 M_{\odot}$ is detected at a distance $d > 5$ Mpc.

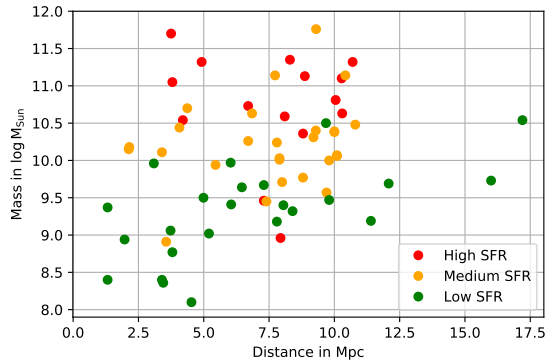


Fig. 6.29: Mass over distance plot. The masses and distances were acquired from Karachentsev et al., 2013.

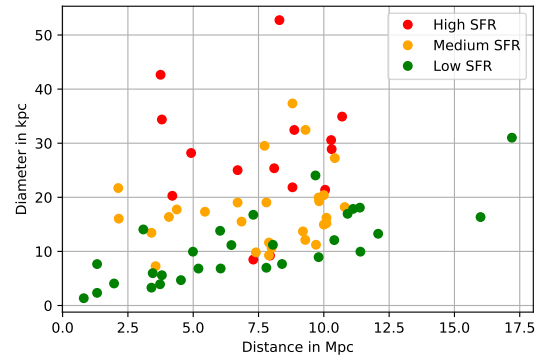


Fig. 6.30: Diameter over distance plot. The diameters and distances were acquired from Karachentsev et al., 2013.

Figure 6.30 shows the diameters of the galaxies based on the ~ 26.5 mag/arcsec² Holmberg isophote. It can be clearly seen that the high SFR galaxies tend to have the largest diameters, and the low SFR galaxies the smallest. This is expected, as larger galaxies are more massive and therefore contain a larger amount of star-forming gas. The largest galaxy of the sample is the spiral galaxy NGC 6744 with a diameter of 52.75 kpc. The lower end of the diagram illustrates the sensitivity limit for the detection of small galaxies at increasing distances. Above a distance of ~ 12 Mpc, no galaxies with a diameter $r < 10$ kpc are detected.

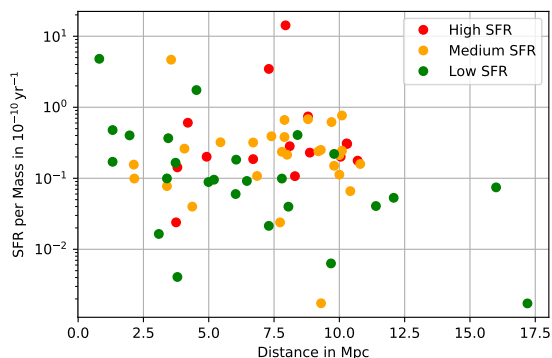


Fig. 6.31: SFR/ M over distance plot. The masses and distances were acquired from Karachentsev et al., 2013. See Table 6.5 for SFR references.

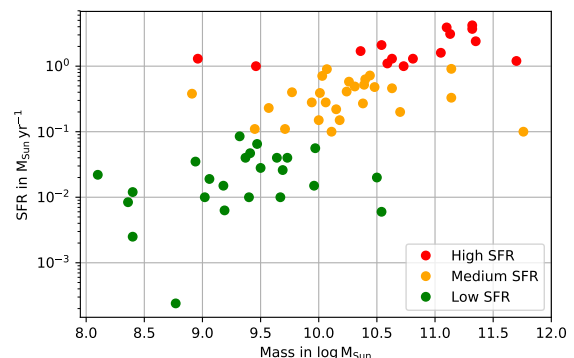


Fig. 6.32: SFR over Mass plot. The masses were acquired from Karachentsev et al., 2013. See Table 6.5 for SFR references.

Figure 6.31 displays the galaxies' SFR divided by their mass. This diagram shows that the SFR is strongly correlated with the mass, since no clear discrepancies can be seen for the different SFR groups. The bulk of the galaxy sample exhibits a SFR/ M value of

$10^{-11} - 10^{-10} \text{ yr}^{-1}$.

The SFR-mass relation can be seen in Figure 6.32. The high SFR galaxies tend to have the highest masses, while the low SFR galaxies tend to have the lowest. The SFR clearly increases with the mass. This is consistent with our expectations, as more massive galaxies can have a higher amount of star-forming gas.

6.10 Fluxes and Luminosities

0.25 – 6 keV	NGC 5128	NGC 5236	NGC 6744	NGC 1291	NGC 300
CR (s^{-1})	2.55 ± 0.04	1.106 ± 0.026	0.757 ± 0.024	0.315 ± 0.012	0.642 ± 0.020
F_{tot} ($\text{erg cm}^{-2} \text{s}^{-1}$)	$1.32^{+0.15}_{-0.19} \cdot 10^{-11}$	$4.11^{+0.16}_{-1.3} \cdot 10^{-12}$	$2.7^{+0.5}_{-0.7} \cdot 10^{-12}$	$1.02^{+0.8}_{-0.28} \cdot 10^{-12}$	$2.7^{+1.0}_{-0.4} \cdot 10^{-12}$
F_{VNEI} ($\text{erg cm}^{-2} \text{s}^{-1}$)	$2.25^{+0.26}_{-0.4} \cdot 10^{-12}$	$3.88^{+0.16}_{-1.3} \cdot 10^{-13}$	$2.2^{+0.5}_{-0.6} \cdot 10^{-13}$	$8.8^{+7}_{-2.5} \cdot 10^{-14}$	$3.0^{+1.1}_{-0.5} \cdot 10^{-13}$
$F_{\text{VNEI}}/F_{\text{tot}}$	17.0%	9.44%	8.19%	8.66%	11.0%
0.25 – 2 keV	NGC 5128	NGC 5236	NGC 6744	NGC 1291	NGC 300
CR (s^{-1})	2.140 ± 0.029	0.929 ± 0.024	0.581 ± 0.021	0.211 ± 0.010	0.409 ± 0.016
F_{tot} ($\text{erg cm}^{-2} \text{s}^{-1}$)	$9.6^{+2.4}_{-1.6} \cdot 10^{-12}$	$3.19^{+0.21}_{-1.2} \cdot 10^{-12}$	$2.0^{+0.8}_{-0.4} \cdot 10^{-12}$	$6.2^{+7.3}_{-0.8} \cdot 10^{-13}$	$1.6^{+0.7}_{-0.4} \cdot 10^{-12}$
F_{VNEI} ($\text{erg cm}^{-2} \text{s}^{-1}$)	$2.3^{+0.4}_{-0.4} \cdot 10^{-12}$	$3.88^{+0.26}_{-1.5} \cdot 10^{-13}$	$2.2^{+0.9}_{-0.5} \cdot 10^{-13}$	$9^{+11}_{-1.2} \cdot 10^{-14}$	$3.0^{+1.3}_{-0.8} \cdot 10^{-13}$
$F_{\text{VNEI}}/F_{\text{tot}}$	23.4%	12.2%	11.1%	14.0%	18.5%
0.25 – 6 keV keV	NGC 1313	NGC 4594	NGC 4945	NGC 4826	NGC 5068
CR (s^{-1})	0.275 ± 0.010	0.253 ± 0.016	0.331 ± 0.013	0.366 ± 0.019	0.254 ± 0.015
F_{tot} ($\text{erg cm}^{-2} \text{s}^{-1}$)	$8.2^{+2.4}_{-2.4} \cdot 10^{-13}$	$9.4^{+6}_{-0.4} \cdot 10^{-13}$	$1.0^{+1.5}_{-0.5} \cdot 10^{-12}$	$1.20^{+0.8}_{-0.05} \cdot 10^{-12}$	$7.35^{+0.24}_{-4} \cdot 10^{-13}$
F_{VNEI} ($\text{erg cm}^{-2} \text{s}^{-1}$)	$1.1^{+0.4}_{-0.4} \cdot 10^{-13}$	$1.65^{+1.1}_{-0.08} \cdot 10^{-13}$	$3^{+5}_{-1.5} \cdot 10^{-13}$	$1.41^{+1.0}_{-0.06} \cdot 10^{-13}$	$9.2^{+0.3}_{-5} \cdot 10^{-14}$
$F_{\text{VNEI}}/F_{\text{tot}}$	13.5%	17.6%	29.1%	11.8%	12.4%
0.25 – 2 keV keV	NGC 1313	NGC 4594	NGC 4945	NGC 4826	NGC 5068
CR (s^{-1})	0.203 ± 0.009	0.214 ± 0.015	0.248 ± 0.011	0.291 ± 0.017	0.193 ± 0.013
F_{tot} ($\text{erg cm}^{-2} \text{s}^{-1}$)	$5.0^{+1.9}_{-1.2} \cdot 10^{-13}$	$6.0^{+5}_{-0.7} \cdot 10^{-13}$	$7^{+12}_{-4} \cdot 10^{-13}$	$8.4^{+8}_{-0.4} \cdot 10^{-13}$	$5.2^{+0.5}_{-2.0} \cdot 10^{-13}$
F_{VNEI} ($\text{erg cm}^{-2} \text{s}^{-1}$)	$1.1^{+0.5}_{-0.3} \cdot 10^{-13}$	$1.65^{+1.4}_{-0.20} \cdot 10^{-13}$	$3^{+5}_{-1.7} \cdot 10^{-13}$	$1.41^{+1.4}_{-0.07} \cdot 10^{-13}$	$9.0^{+0.9}_{-4} \cdot 10^{-14}$
$F_{\text{VNEI}}/F_{\text{tot}}$	22.2%	27.5%	40.7%	16.8%	17.3%

Tab. 6.8: Count rates CR, total fluxes F_{tot} , and VNEI fluxes F_{VNEI} in the energy ranges 0.25 – 6 keV and 0.25 – 2 keV for the galaxies NGC 5128, NGC 5236, NGC 6744, NGC 1291, NGC 300, NGC 1313, NGC 4594, NGC 4945, NGC 4826 and NGC 5068.

In the next step, the X-ray fluxes and luminosities of the diffuse gas within our galaxies will be determined. This is done via the *calcflux* command in PyXspec. For the galaxies NGC 5128, NGC 5236, NGC 6744, NGC 1291, NGC 300, NGC 1313, NGC 4594, NGC 4945, NGC 4826 and NGC 5068, the fluxes can be directly determined from the model fitted to their spectra. For the remaining galaxies, the fluxes will be estimated from the model fitted to the stacked spectrum of their SFR group.

The *calcflux* command yields an energy flux F with errors at 90% confidence for a specified energy range. By running the command for the complete spectral model within the energy range 0.25 – 6 keV, we acquire the total flux F_{tot} (including background X-ray emission). The particle background (PB) is excluded via the FWC model. The contribution of the diffuse, X-ray emitting gas is given by the flux of the VNEI model component F_{VNEI} . They are acquired by running the *calcflux* command after setting the normalizations of all

other model components to zero. The diffuse gas mainly emits at energies below 2 keV. In addition, the PB contribution is smaller at these energies. Therefore the energy range 0.25 – 2 keV is considered for the diffuse gas flux. The results for the galaxies NGC 5128, NGC 5236, NGC 6744, NGC 1291, NGC 300, NGC 1313, NGC 4594, NGC 4945, NGC 4826 and NGC 5068 are listed in Table 6.8. The fraction of the diffuse gas flux F_{VNEI} compared to the total flux F_{tot} spans between 10.9% and 38.2% in the energy range 0.25 – 2 keV.

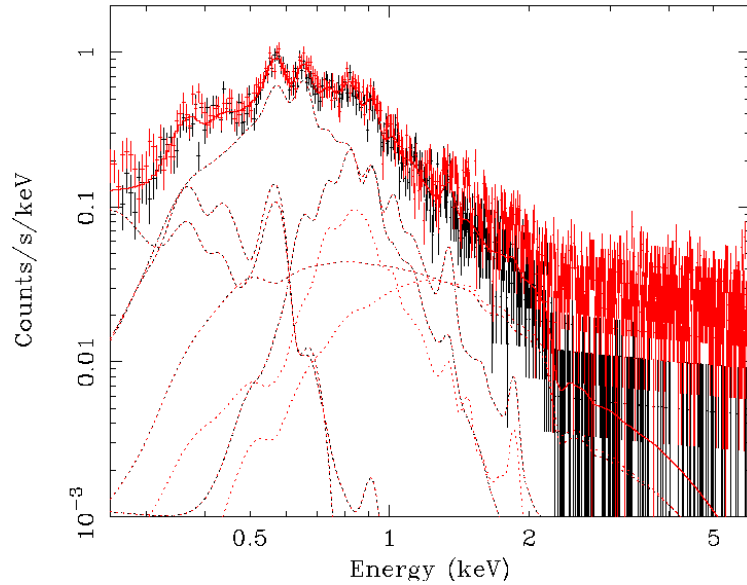


Fig. 6.33: This diagram illustrates the contribution of the particle background to the high SFR spectrum (red data points). The red line displays the spectral model at $\tau = 10^{12} \text{ s cm}^{-3}$, where contributions from the particle background have been excluded. The black data points represent a simulated spectrum to this model.

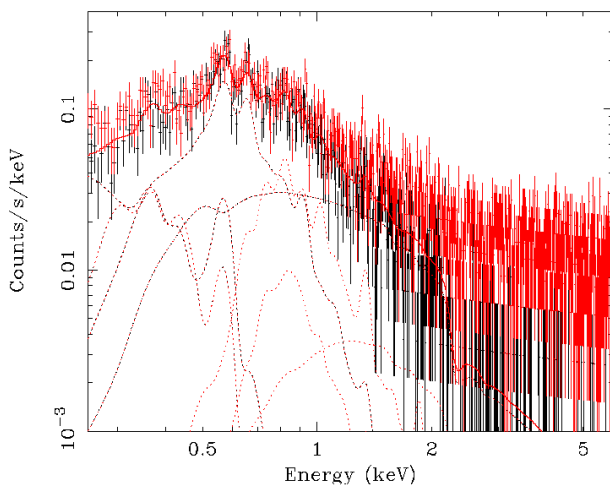


Fig. 6.34: Particle background contribution of medium SFR spectrum.

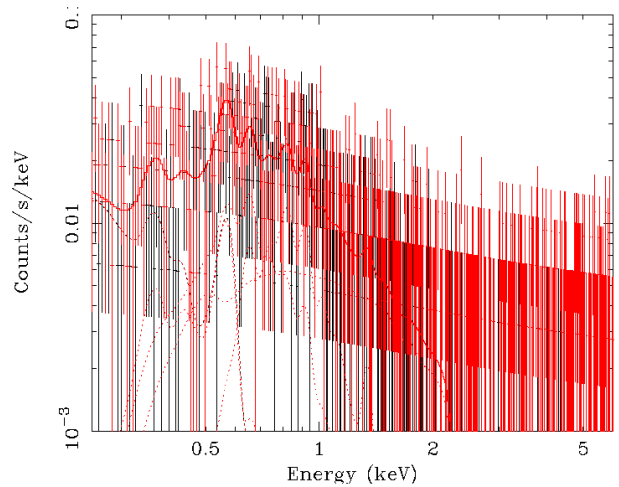


Fig. 6.35: Particle background contribution of low SFR spectrum.

The remaining galaxies are too faint for spectral modelling, and therefore their flux cannot be confidently determined. However, by investigating the properties of the stacked spectra, we can derive a count rate (CR) to flux relation and calculate rough flux estimates based on their CR. The total CR of each galaxy is acquired by summing the counts within an energy range of 0.25 – 6 keV and dividing it by the exposure time. For the diffuse gas emission, only energies up to 2 keV are considered. These counts include background emission, contamination from X-ray binaries, as well as contributions from the PB. The influence of the PB is illustrated in Figure 6.33, Figure 6.34 and Figure 6.35 for the high, medium and low SFR galaxies, respectively. The diagrams present the stacked spectra (red data points) and the spectral models at $\tau = 10^{12} \text{ s cm}^{-3}$ (red lines), which excluded PB contributions via the FWC model. The Xspec command *fakeit* was used to simulate PB-corrected spectra to the models (black data points) and calculate their CR. The CR and flux results for the stacked spectra are listed in Table 6.9.

0.25 – 6 keV	High SFR	Medium SFR	Low SFR
$\text{CR}_{\text{data}} (\text{s}^{-1})$	$(6.42 \pm 0.06) \cdot 10^{-1}$	$(1.960 \pm 0.025) \cdot 10^{-1}$	$(3.89 \pm 0.12) \cdot 10^{-2}$
$\text{CR}_{\text{fakeit}} (\text{s}^{-1})$	$(4.88 \pm 0.06) \cdot 10^{-1}$	$(1.180 \pm 0.020) \cdot 10^{-1}$	$(2.16 \pm 0.09) \cdot 10^{-2}$
$\Delta\text{CR}_{\text{PB}} (\text{s}^{-1})$	$(1.54 \pm 0.12) \cdot 10^{-1}$	$(7.8 \pm 0.5) \cdot 10^{-2}$	$(1.73 \pm 0.21) \cdot 10^{-2}$
$F_{\text{tot}} (\text{erg cm}^{-2} \text{s}^{-1})$	$2.1_{-0.6}^{+1.0} \cdot 10^{-12}$	$5.6_{-0.7}^{+4} \cdot 10^{-13}$	$1.01_{-0.020}^{+2.4} \cdot 10^{-13}$
$F_{\text{VNEI}} (\text{erg cm}^{-2} \text{s}^{-1})$	$2.3_{-0.7}^{+1.1} \cdot 10^{-13}$	$4.2_{-0.6}^{+3} \cdot 10^{-14}$	$9.8_{-0.2}^{+24} \cdot 10^{-15}$
$F_{\text{VNEI}}/F_{\text{tot}}$	11.0%	7.41%	9.66%
0.25 – 2 keV	High SFR	Medium SFR	Low SFR
$\text{CR}_{\text{data}} (\text{s}^{-1})$	$(5.26 \pm 0.06) \cdot 10^{-1}$	$(1.410 \pm 0.021) \cdot 10^{-1}$	$(2.70 \pm 0.10) \cdot 10^{-2}$
$\text{CR}_{\text{fakeit}} (\text{s}^{-1})$	$(4.71 \pm 0.06) \cdot 10^{-1}$	$(1.120 \pm 0.019) \cdot 10^{-1}$	$(2.05 \pm 0.09) \cdot 10^{-2}$
$\Delta\text{CR}_{\text{PB}} (\text{s}^{-1})$	$(5.5 \pm 1.2) \cdot 10^{-2}$	$(2.9 \pm 0.4) \cdot 10^{-2}$	$(6.5 \pm 1.9) \cdot 10^{-3}$
$F_{\text{tot}} (\text{erg cm}^{-2} \text{s}^{-1})$	$1.5_{-0.5}^{+0.5} \cdot 10^{-12}$	$3.5_{-0.5}^{+2.1} \cdot 10^{-13}$	$6.14_{-0.24}^{+11} \cdot 10^{-14}$
$F_{\text{VNEI}} (\text{erg cm}^{-2} \text{s}^{-1})$	$2.3_{-0.8}^{+0.8} \cdot 10^{-13}$	$4.1_{-0.6}^{+2.5} \cdot 10^{-14}$	$9.7_{-0.4}^{+18} \cdot 10^{-15}$
$F_{\text{VNEI}}/F_{\text{tot}}$	15.1%	11.6%	15.9%

Tab. 6.9: Count rates of spectra CR_{data} , count rates of simulated spectra to PB-corrected model $\text{CR}_{\text{fakeit}}$, count rate error caused by the particle background $\Delta\text{CR}_{\text{PB}}$, total fluxes F_{tot} , VNEI energy fluxes F_{VNEI} and flux fractions in the energy ranges 0.25 – 6 keV and 0.25 – 2 keV for the stacked spectra at $\tau = 10^{12} \text{ s cm}^{-3}$.

These values can now be converted to a CR-flux scaling factor, which is used to calculate the total luminosities in the energy range 0.25 – 6 keV:

$$\frac{L_{\text{tot}}}{L_{\odot}}(G) = \text{CR}(G) \cdot \frac{F_{\text{tot}}}{\text{CR}_{\text{data}}} \cdot \frac{4\pi d(G)^2}{L_{\odot}}, \quad (6.2)$$

where $\text{CR}(G)$ is the count rate and $d(G)$ the distance of the corresponding galaxy G . It is important to note, that the count rates include background emission. The resulting values therefore only pose upper limits to the actual luminosities of the galaxies.

By connecting the count rates of the stacked spectra CR_{data} to the flux of the PB-corrected model, we acquire a scaling factor $\frac{F_{\text{tot}}}{\text{CR}_{\text{data}}}$ that relates the PB-contaminated CR to a PB-corrected flux. The CR error caused by the particle background $\Delta\text{CR}_{\text{PB}}$ is given by the

difference of CR_{data} and the CR of the simulated, PB-corrected spectrum CR_{fakeit} (see Table 6.9). The results for the total luminosities L_{tot} were plotted over the galaxy distance (see Figure 6.36 and Figure 6.37).

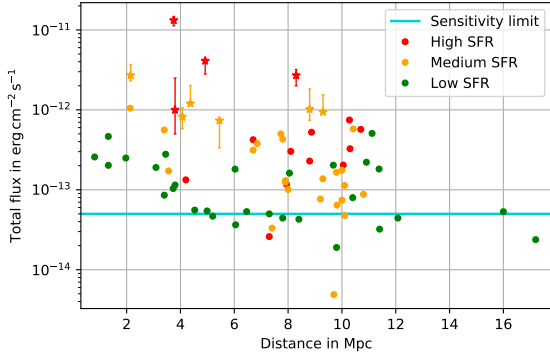


Fig. 6.36: Total eROSITA flux in 0.25 – 6 keV energy range over distance plot. Galaxies that were included in the single spectral analysis are marked by stars. The blue line illustrates the eROSITA flux sensitivity limit of $5 \cdot 10^{-14} \text{ erg cm}^{-2} \text{ s}^{-1}$ (Merloni et al., 2012). The distances were acquired from Karachentsev et al., 2013.

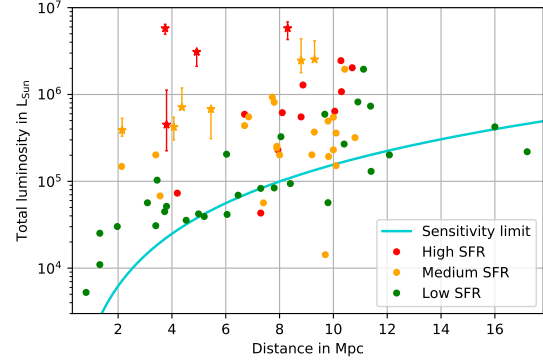


Fig. 6.37: Total luminosity in 0.25 – 6 keV energy range, calculated from the eROSITA energy flux, over distance plot. Galaxies that were included in the single spectral analysis are marked by stars. The blue line illustrates the eROSITA flux sensitivity limit of $5 \cdot 10^{-14} \text{ erg cm}^{-2} \text{ s}^{-1}$ (Merloni et al., 2012). The distances were acquired from Karachentsev et al., 2013.

Galaxies, for which the fluxes were directly determined (Table 6.8), are marked by stars. The luminosity diagram also displays the typical eROSITA flux sensitivity limit of $5 \cdot 10^{-14} \text{ erg cm}^{-2} \text{ s}^{-1}$ (Merloni et al., 2012). Most galaxies of the sample exceed this threshold. However, galaxies are extended sources, with angular diameters that are too large to be classified as a source by the eROSITA source detection. The acquired fluxes are average values for the whole extraction region. In reality, the X-ray flux is subject to strong variation, and is typically the highest in the central region of the galaxy, where the high stellar density is favorable for the formation of X-ray binaries. These bright central regions are, in many cases (e.g. Circinus and NGC 3621), marked by the eROSITA source detection. This can be seen in the image catalog in chapter 8.

In order to estimate the flux and luminosity fraction, that originates from the diffuse gas, only the flux of the vnei model component must be considered. The normalizations of the background and X-ray binary model components are therefore set to zero. The resulting models are visualized by the red line in Figure 6.38, Figure 6.39 and Figure 6.40 for the high, medium and low SFR galaxies, respectively. The red data points represent the spectra, the black data points display a simulated *fakeit*-spectrum to the vnei model component. For the calculation of the diffuse gas fluxes and luminosities, only energies up to 2 keV are considered. The errors for the diffuse gas fluxes and luminosities are propagated from the total flux and total luminosity 90% confidence errors.

The energy flux of the VNEI model component F_{VNEI} makes up 11.5% – 15.8% of the total energy flux in the 0.2 – 2 keV energy range. By implementing a second scaling factor $\frac{F_{\text{VNEI}}}{F_{\text{tot}}}$ into our equations, we can calculate the diffuse gas photon fluxes and luminosities of our galaxies in the energy range 0.25 – 2 keV:

$$\frac{L_{\text{VNEI}}(G)}{L_{\odot}} = \text{CR}(G) \cdot \frac{F_{\text{tot}}}{\text{CR}_{\text{data}}} \cdot \frac{F_{\text{VNEI}}}{F_{\text{tot}}} \cdot \frac{4\pi d(G)^2}{L_{\odot}}. \quad (6.3)$$

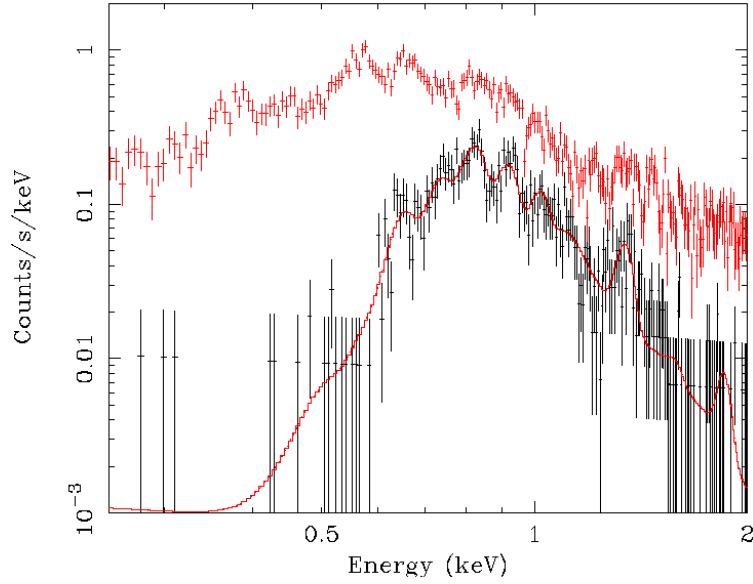


Fig. 6.38: This diagram visualizes the contribution of the VNEI component at $\tau = 10^{12} \text{ s cm}^{-3}$ (red line) to the spectral model. The red data points represent the high SFR spectrum, the black ones a simulated spectrum to the VNEI model component.

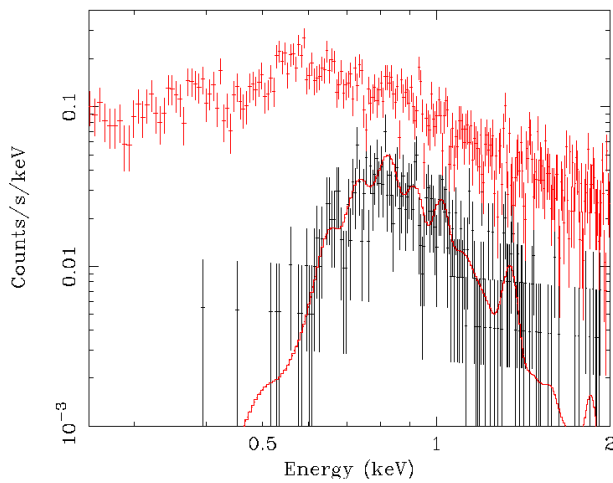


Fig. 6.39: VNEI component at $\tau = 10^{12} \text{ s cm}^{-3}$ of medium SFR spectrum.

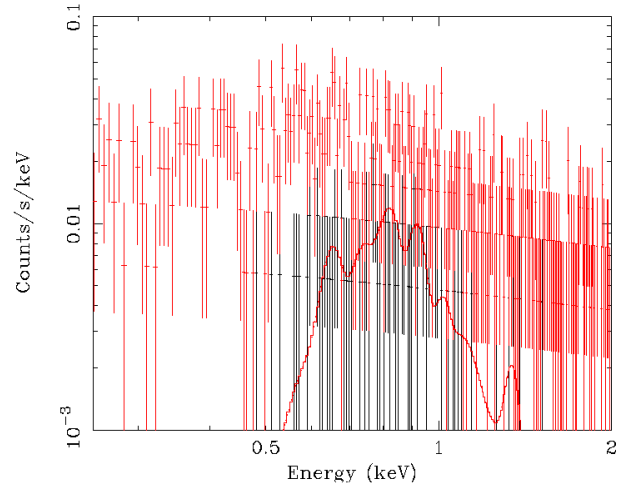


Fig. 6.40: VNEI component at $\tau = 10^{12} \text{ s cm}^{-3}$ of low SFR spectrum.

By doing so, we assume that the fraction of background and X-ray binary contamination of each galaxy is equivalent to the one of their respective stacked spectrum. The resulting values for the diffuse gas luminosities L_{VNEI} are listed in Table 6.3, Table 6.4 and Table 6.5 and plotted in Figure 6.41 and Figure 6.42. In contrast to the total luminosity, the diffuse gas luminosity is weaker than the eROSITA flux sensitivity limit for most galaxies. However all 10 galaxies, for which the photon statistics were sufficient for single spectral analysis (marked by stars in Figure 6.42) exceed this threshold.

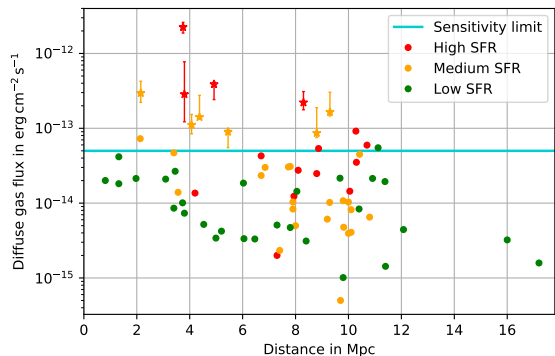


Fig. 6.41: VNEI flux in 0.25 – 2 keV energy range over distance plot. Galaxies that were included in the single spectral analysis are marked by stars. The blue line illustrates the eROSITA flux sensitivity limit of $5 \cdot 10^{-14} \text{ erg cm}^{-2} \text{ s}^{-1}$ (Merloni et al., 2012). The distances were acquired from Karachentsev et al., 2013.

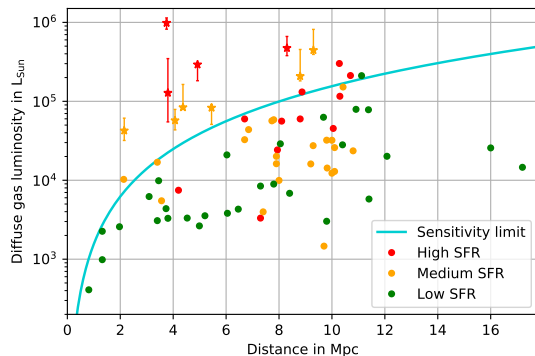


Fig. 6.42: VNEI luminosity in 0.25 – 2 keV energy range, calculated from the VNEI energy flux, over distance plot. Galaxies that were included in the single spectral analysis are marked by stars. The blue line illustrates the eROSITA flux sensitivity limit of $5 \cdot 10^{-14} \text{ erg cm}^{-2} \text{ s}^{-1}$ (Merloni et al., 2012). The distances were acquired from Karachentsev et al., 2013.

6.11 L_X – SFR Relation

Lastly, the acquired luminosities were plotted over the SFR to check if the distribution is consistent with a linear L_X – SFR relation, as proposed by e.g. Mineo et al., 2014. In their Chandra study of X-ray emission from star-forming galaxies, Mineo et al., 2014 investigated the relation between the total X-ray emission and the star-forming activity. They analyzed a sample of 66 galaxies with SFRs in the range $\sim 0.1 - 10^3 M_\odot \text{ yr}^{-1}$ and determined a linear scaling relation $L_X/\text{SFR} \approx (4.0 \pm 0.4) \cdot 10^{39} (\text{erg s}^{-1}) / (M_\odot \text{ yr}^{-1})$ within the energy range 0.5 – 8 keV.

In this work, the L_X/SFR scaling relation has been determined for both the total eROSITA flux (see Figure 6.43) and the VNEI fraction of the eROSITA flux (see Figure 6.44). It is important to note however, that the total luminosities are not background-corrected and therefore only pose an upper limit to the actual luminosities. The VNEI fraction provides a more reliable estimate (for the X-ray luminosity of the diffuse gas).

The diagrams display a clear tendency of the luminosity increasing with the SFR. The diffuse gas luminosities of the low SFR galaxies are mostly spread between $10^3 L_\odot$ and $10^5 L_\odot$, while the medium SFR galaxies are mostly concentrated in the $10^4 - 10^5 L_\odot$ range.

About half of the high SFR galaxies exceed $10^5 L_{\odot}$, with the brightest one being NGC 6744 at $4.47 \cdot 10^5 L_{\odot}$.

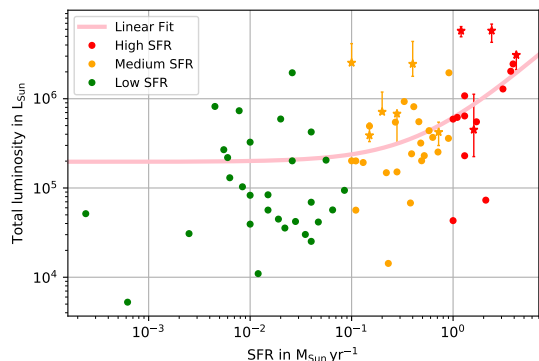


Fig. 6.43: Total luminosity in 0.25 – 6 keV energy range, calculated from the eROSITA flux, over SFR plot. Galaxies that were included in the single spectral analysis are marked by stars. Fit parameters: $m = (4.2 \pm 1.0) \cdot 10^5 L_{\odot} M_{\odot}^{-1} \text{ yr}$, $b = (2.0 \pm 1.0) \cdot 10^5 L_{\odot}$. See Table 6.5 for SFR references.

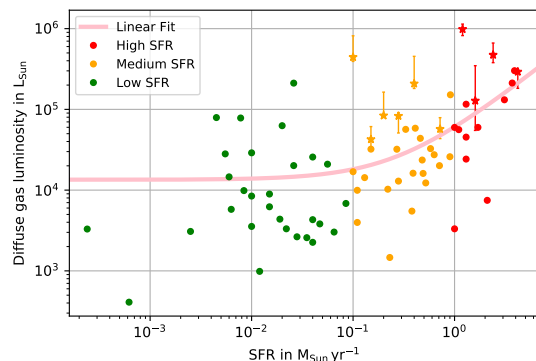


Fig. 6.44: vNEI luminosity in 0.25 – 2 keV energy range, calculated from the eROSITA flux, over SFR plot. Galaxies that were included in the single spectral analysis are marked by stars. Fit parameters: $m = (4.7 \pm 0.8) \cdot 10^4 L_{\odot} M_{\odot}^{-1} \text{ yr}$, $b = (1.3 \pm 0.8) \cdot 10^4 L_{\odot}$. See Table 6.5 for SFR references.

The data was fitted with a linear function of the form $f(x) = m \cdot x + b$, yielding the fit parameters $m = (4.2 \pm 1.0) \cdot 10^5 L_{\odot} M_{\odot}^{-1} \text{ yr}$, $b = (2.0 \pm 1.0) \cdot 10^5 L_{\odot}$ for the total luminosities and $m = (4.7 \pm 0.8) \cdot 10^4 L_{\odot} M_{\odot}^{-1} \text{ yr}$, $b = (1.3 \pm 0.8) \cdot 10^4 L_{\odot}$ for the diffuse gas luminosities. The scaling factors for the total X-ray luminosity $L_{X,\text{tot}}/\text{SFR}$ and the vNEI fraction of the X-ray luminosity $L_{X,\text{vNEI}}/\text{SFR}$ are therefore

$$L_{X,\text{tot}}/\text{SFR} = (1.6 \pm 0.4) \cdot 10^{39} (\text{erg s}^{-1})/(\text{M}_{\odot} \text{ yr}^{-1}) \quad (6.4)$$

$$L_{X,\text{vNEI}}/\text{SFR} = (1.8 \pm 0.4) \cdot 10^{38} (\text{erg s}^{-1})/(\text{M}_{\odot} \text{ yr}^{-1}) \quad (6.5)$$

The luminosities are, as expected, consistent with a linear $L_X - \text{SFR}$ relation. The large scatter around the fit and the accompanied errors can be explained by the fact, that the luminosity strongly depends on further parameters, such as the metallicity. The scaling factor for the X-ray emission of the diffuse gas $L_{X,\text{vNEI}}/\text{SFR}$ is roughly one order of magnitude smaller than the scaling factor of the total X-ray emission, while the scaling factor for the total X-ray emission $L_{X,\text{tot}}/\text{SFR}$ is $\sim 60\%$ smaller than the value derived by Mineo et al., 2014. This can be explained by multiple factors. Firstly, Mineo et al., 2014, analyzed Chandra data with a higher sensitivity in the X-ray band, which enables more precise analysis and background-correction. Secondly, Mineo et al., 2014, considered energies up to 8 keV. At these energies, X-ray binaries contribute significantly more to the total X-ray flux, especially in high SFR galaxies with a high abundance of HMXBs. This can lead to a sharper rise of the X-ray luminosity with increasing SFR. Thirdly, the data set chosen by Mineo et al., 2014, covers a wider range of SFR values, including galaxies that are experiencing intense

starbursts with SFRs up to $\sim 10^3 M_{\odot} \text{ yr}^{-1}$, while our sample is focused on the low-SFR end of galaxies. Our results therefore indicate, that the L_X/SFR scaling factor decreases at the low-SFR tail of galaxies.

7 Summary and Conclusion

With the most sensitive X-ray All-Sky-Survey to date, eROSITA has given us the opportunity to explore the vastness of the local X-ray Universe. While GCs produce point-like emission through X-ray binaries, galaxies often host a huge amount of hot gas that enlightens the soft X-ray band via diffuse, thermal emission. By investigating the collective data of the first four eROSITA All-Sky-Surveys eRASS1 - eRASS4, an X-ray image catalog has been created for 72 galaxies within a distance of $d \lesssim 17$ Mpc. The images display the distribution of the hot gas and the position of X-ray point sources in the field of view. While many galaxies exhibit little to no X-ray emission, others are particularly bright, e.g. Centaurus A. The heating of the gas can be induced by various processes, e.g. recent interactions and mergers with other galaxies. In the case of Centaurus A, a recent merger might have led to an increase in AGN feedback and jet-induced star-forming activity. The spectra of the galaxies NGC 5128, NGC 5236, NGC 6744, NGC 1291, NGC 300, NGC 1313, NGC 4594, NGC 4945, NGC 4826 and NGC 5068 have been analyzed in Xspec with a five-component background model and a VNEI source component. The VNEI component is a frequently used plasma model for SNRs, which describes the equilibration of a constant-temperature, impulsively heated postshock gas. According to Chandra, XMM-Newton or Suzaku studies (e.g., Kavanagh et al., 2020; Kuntz et al., 2010, and references therein) of diffuse X-ray emission in nearby galaxies, most galaxies exhibit a thermal plasma component at temperatures of $kT \sim 0.2$ keV, and sometimes an additional, hotter component at $kT > 0.5$ keV. Due to the low eROSITA photon statistics, our galaxy sample has been modelled by only one thermal component for three different values of the ionization timescale $\tau = 10^{11}, 10^{12}, 10^{13} \text{ s cm}^{-2}$. The results for $\tau = 10^{12} \text{ s cm}^{-2}$ and $\tau = 10^{13} \text{ s cm}^{-2}$ are generally better constrained and more consistent, implying that the gas is in collisional ionization equilibrium. For 8 out of 10 galaxies, the results are consistent with a $\sim 0.2 - 0.3$ keV thermal component, which is in agreement with the previous studies of e.g. Kavanagh et al., 2020; Kuntz et al., 2010, and references therein. The hot ISM in equilibrium is expected to reach temperatures of ~ 0.2 keV, whereas contributions from SNRs, H II regions and superbubbles likely increase the average plasma temperature to ~ 0.3 keV in e.g. NGC 4826. For NGC 1291, the plasma temperature is slightly higher (~ 0.47 keV for $\tau = 10^{12} \text{ s cm}^{-2}$), and for NGC 4945 it is the highest with ~ 0.63 keV at $\tau = 10^{12} \text{ s cm}^{-2}$. In the case of NGC 1291, the high plasma temperature can be explained by gas infall onto the galactic center, during which the gas is accelerated and heated to X-ray temperatures (Pérez et al., 2006). NGC 4945, on the other hand, hosts a Seyfert 2 AGN and a central starburst, which generate a large-scale outflow of warm, ionized gas along its minor axis (e.g. Mingozzi et al., 2019). According to Bellocchi et al., 2020, the ISM in NGC 4945 is heated via shocks and turbulence generated by this outflow. Further studies of NGC 1291 and NGC 4945 need to be conducted to determine if the emission is better described by multiple thermal components at different temperatures. On average, the X-ray emitting gas had a temperature of $0.29_{-0.16}^{+0.16}$ keV (at $\tau = 10^{12} \text{ s cm}^{-2}$) in our sample of 10 galaxies. It can be concluded, that most normal galaxies exhibit a thermal plasma component at $kT \sim 0.2 - 0.3$ keV, whereas galaxies that experienced recent heating, e.g. through mergers, dynamical interactions or AGN feedback, can contain hotter gas with $kT \gtrsim 0.47$ keV.

The spectra of the fainter galaxies were stacked in order to acquire average spectra for high, medium and low SFR galaxies. The analysis yielded average plasma temperatures of $0.30_{-0.03}^{+0.04}$, $0.34_{-0.06}^{+0.08}$ and $0.26_{-0.11}^{+0.06}$ keV at $\tau = 10^{12} \text{ s cm}^{-2}$, for the high, medium and low SFR galaxies, respectively. The intrinsic absorption is, at hydrogen column densities of $\sim 0.5 - 0.7 \cdot 10^{22} \text{ cm}^{-2}$, roughly the same for all samples. These results are accompanied by large uncertainties due to the high background contamination and low source emission of fainter galaxies, and need to be improved by higher-sensitivity studies of a larger sample of galaxies in the future.

The total X-ray and diffuse gas fluxes of our galaxies were compared to the eROSITA sensitivity limit. It was found that, while the total flux typically exceeds the sensitivity limit, the diffuse gas flux is below this threshold for all but 15 galaxies. This explains why only 10 galaxies of our sample were successfully fitted with the VNEI component and stresses the need of more sensitive X-ray surveys in the future.

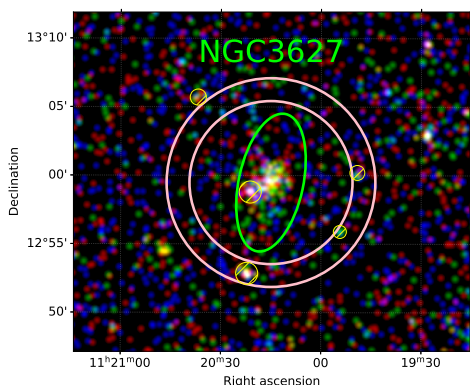
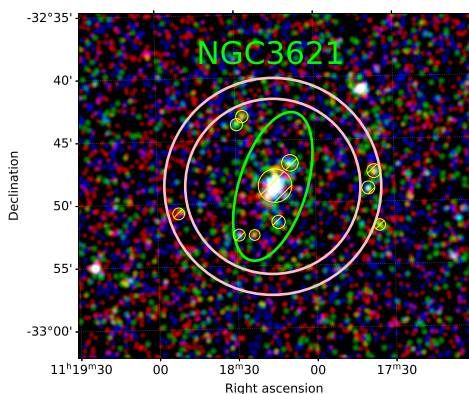
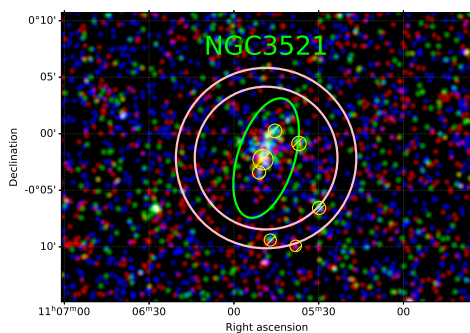
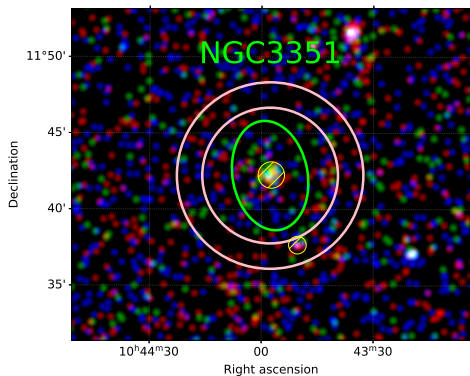
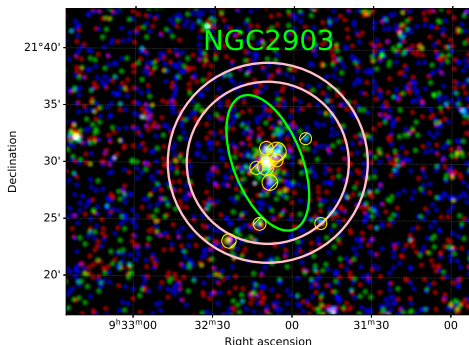
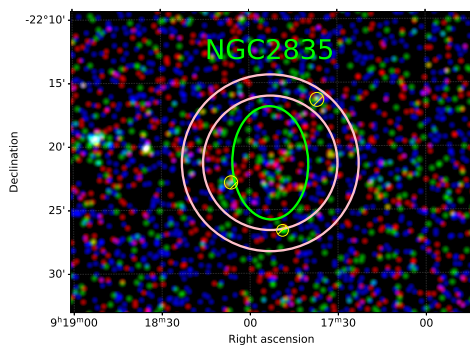
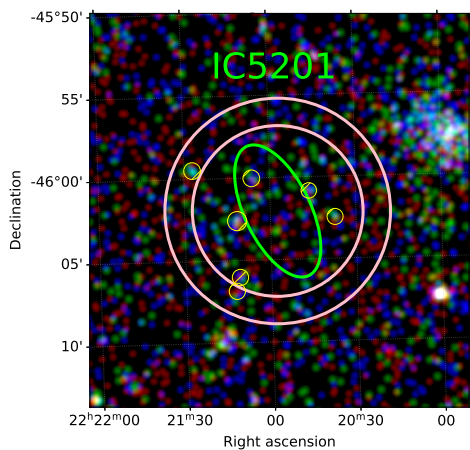
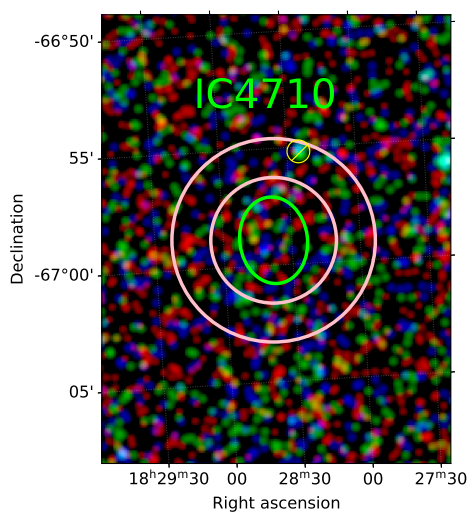
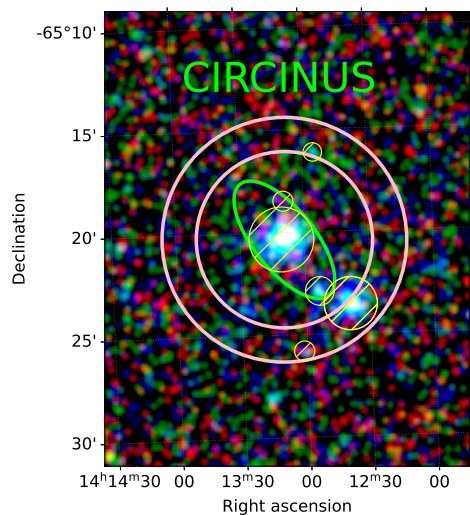
The spectral models were further used to estimate the total X-ray luminosities $L_{X,\text{tot}}$ and the diffuse gas X-ray luminosities $L_{X,\text{VNEI}}$ for the selected galaxies. Due to contributions of the X-ray background, the $L_{X,\text{tot}}$ values only pose upper limits to the actual luminosities. However, they can still be used to estimate the $L_{X,\text{tot}} - \text{SFR}$ scaling factor if a uniform X-ray background is assumed. We acquire a $L_{X,\text{tot}} - \text{SFR}$ value of $(1.6 \pm 0.4) \cdot 10^{39} \text{ (erg s}^{-1}\text{)}/(\text{M}_{\odot} \text{ yr}^{-1})$, which is $\sim 60\%$ smaller compared to the value derived by Mineo et al., 2014, and indicates that the scaling factor decreases at the low-SFR tail of galaxies. For the diffuse gas emission, we derive a scaling factor of $L_{X,\text{VNEI}}/\text{SFR} = (1.8 \pm 0.4) \cdot 10^{38} \text{ (erg s}^{-1}\text{)}/(\text{M}_{\odot} \text{ yr}^{-1})$.

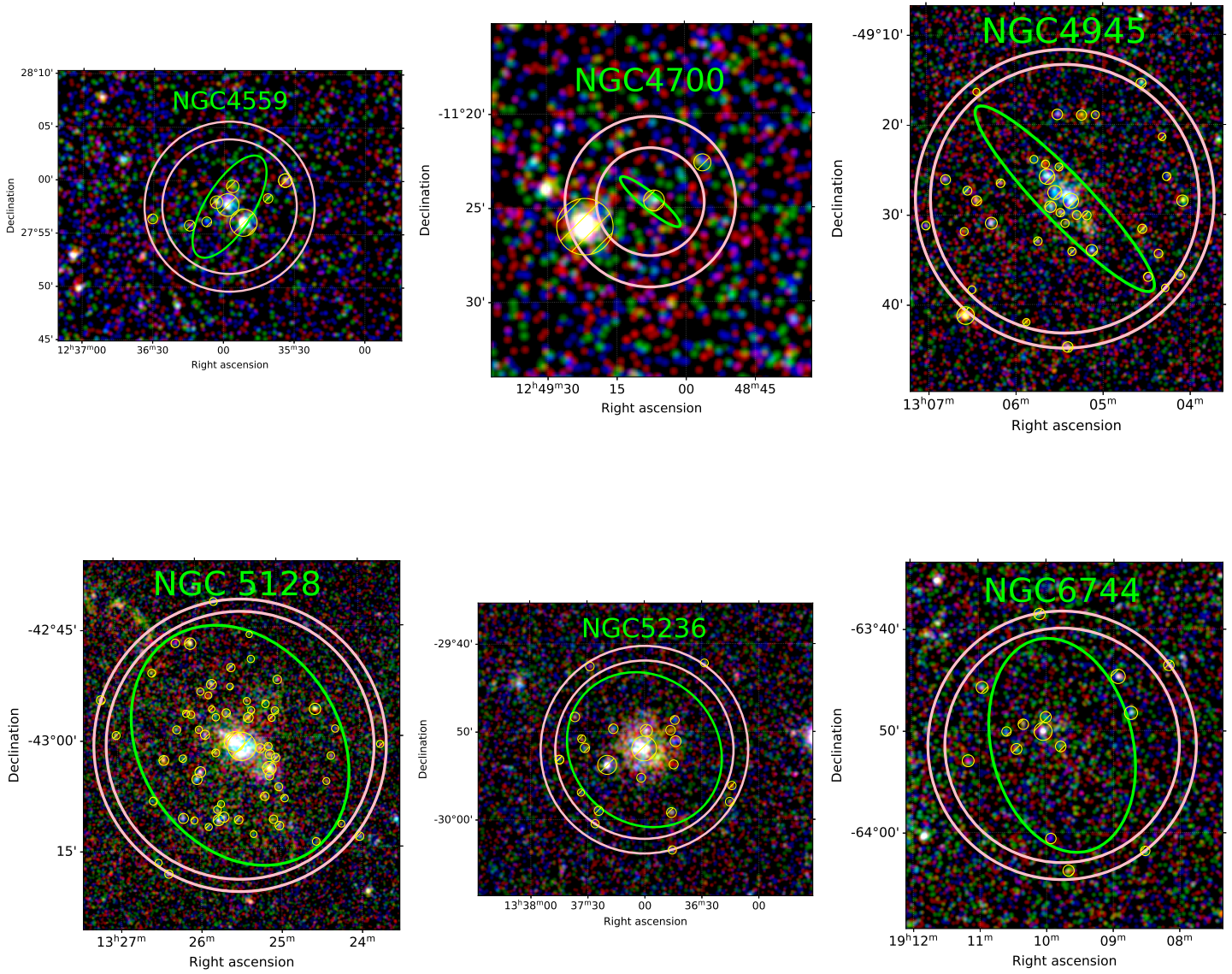
In conclusion, this study provided a solid overview on the abundance and properties of X-ray emitting gas in nearby galaxies. However, a more accurate picture can be achieved through follow-up observations and studies, which is required to truly constrain the processes of galactic evolution, and ultimately, to improve our understanding of the Universe.

8 Appendix

High SFR Galaxies

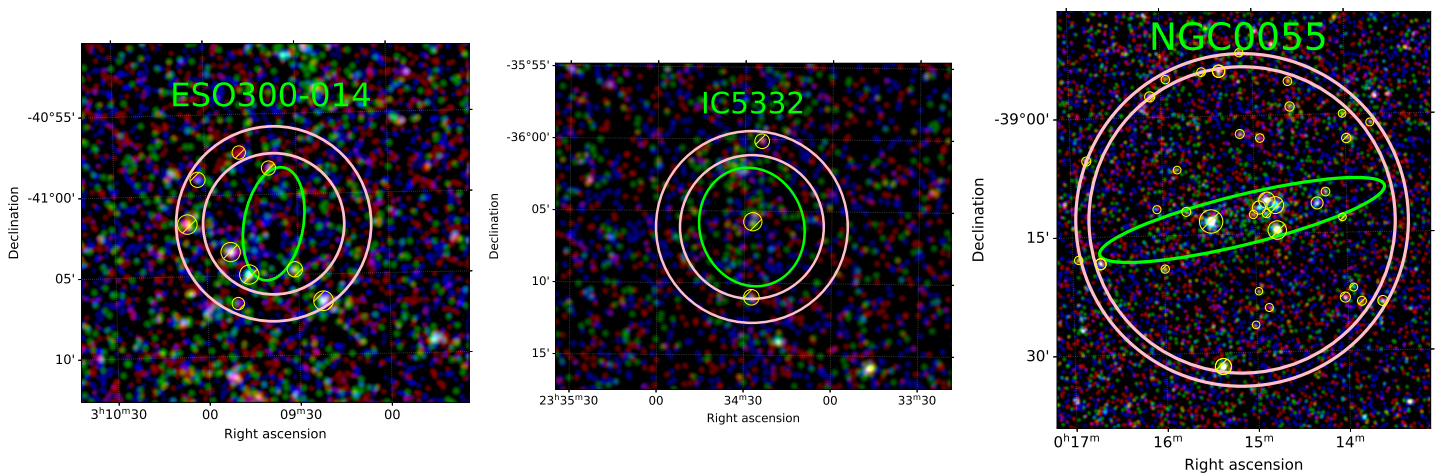
This section displays the eROSITA images of all galaxies in the $\text{SFR} \geq 1.0 M_{\odot} \text{ yr}^{-1}$ range. See Figure 5.1 for more details.

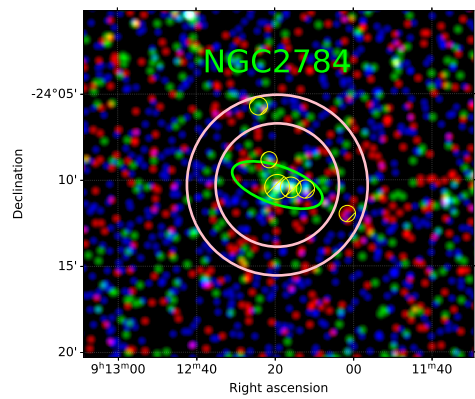
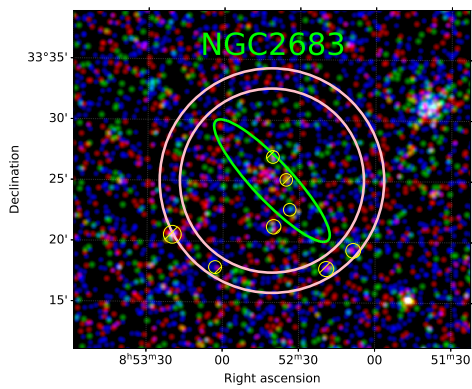
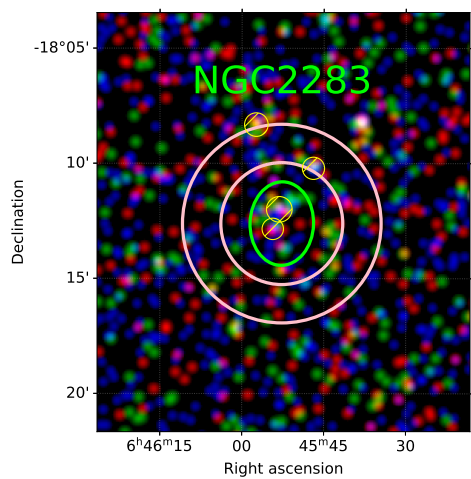
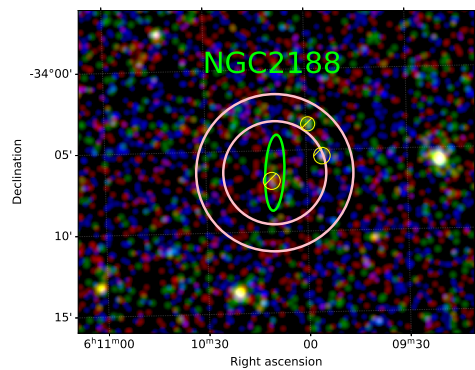
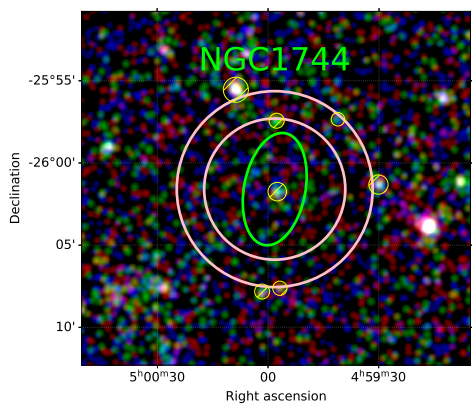
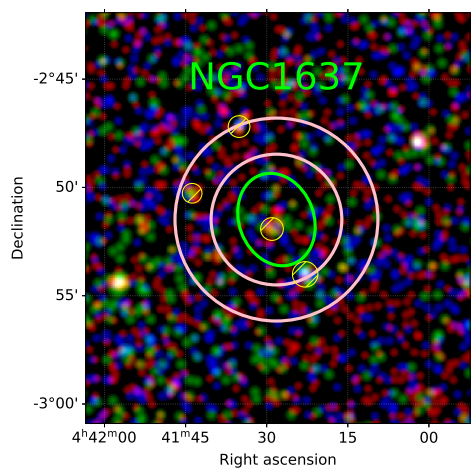
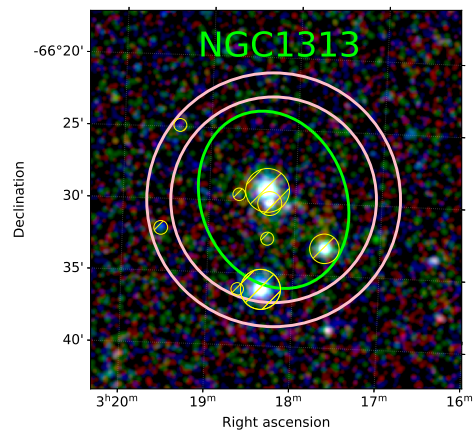
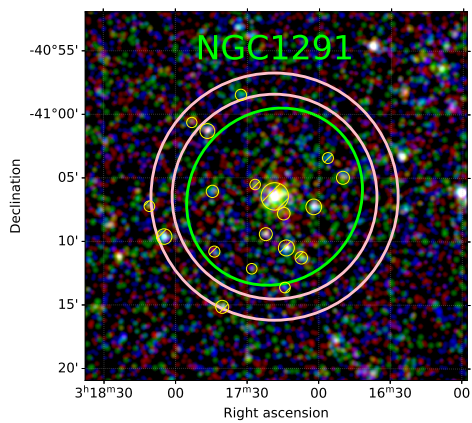
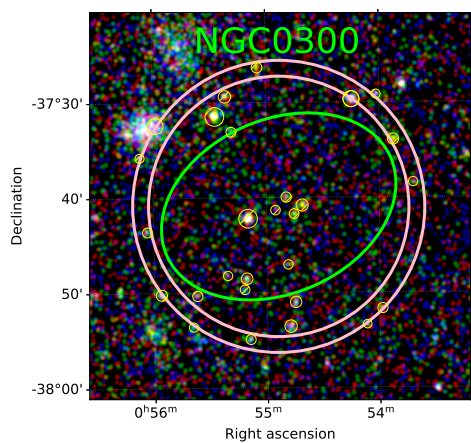


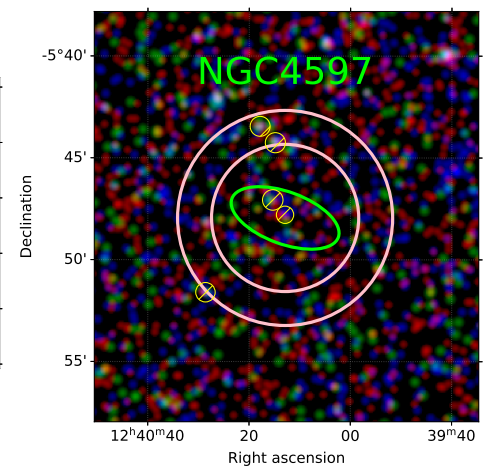
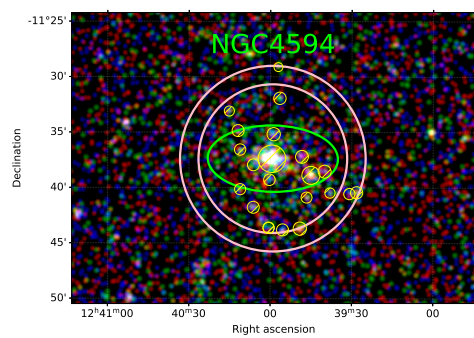
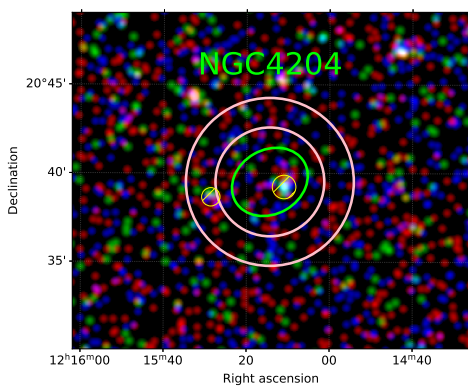
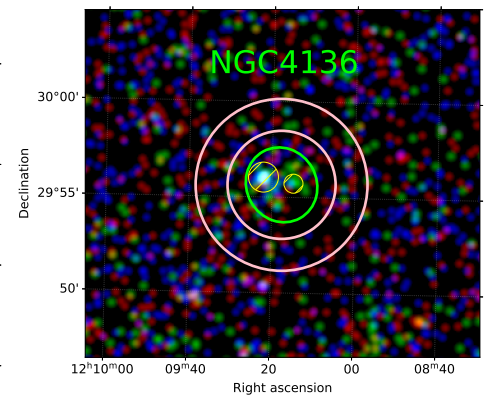
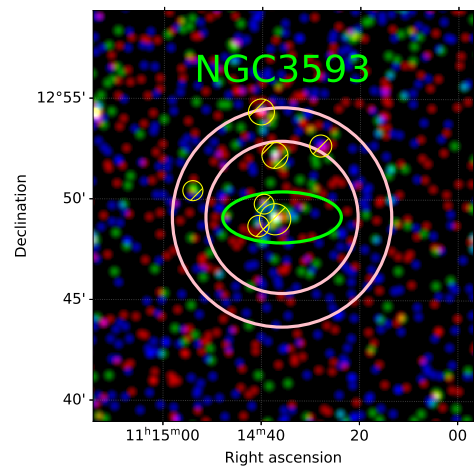
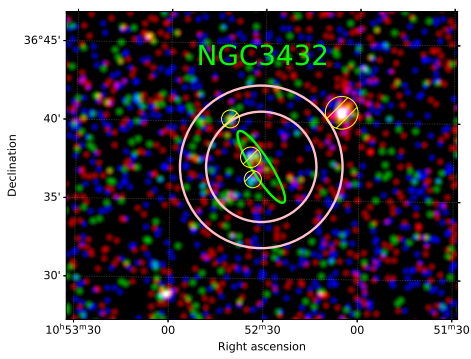
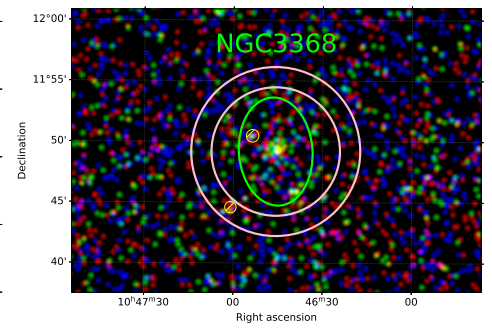
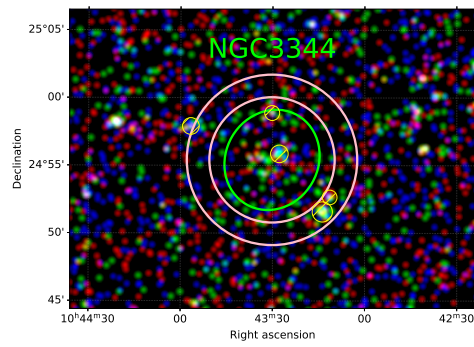
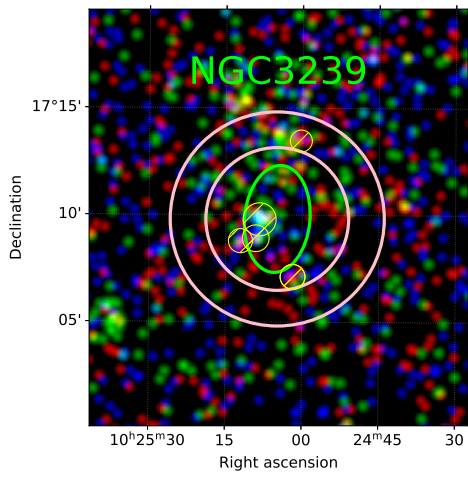


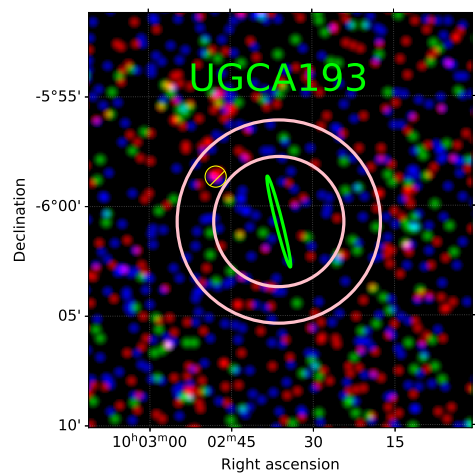
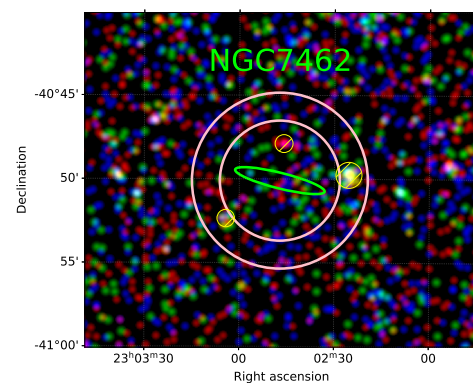
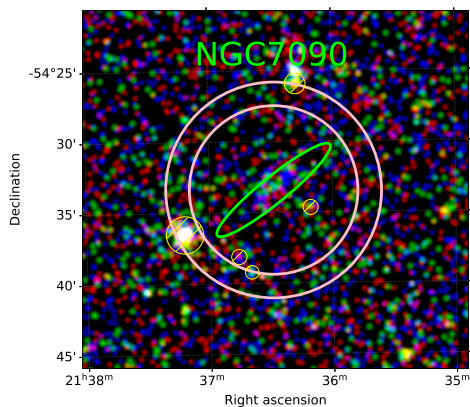
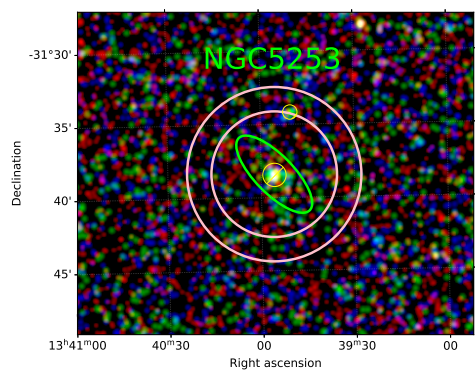
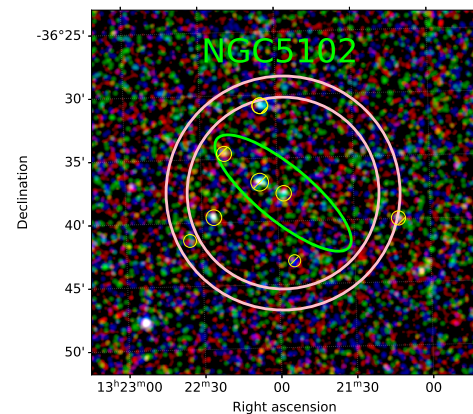
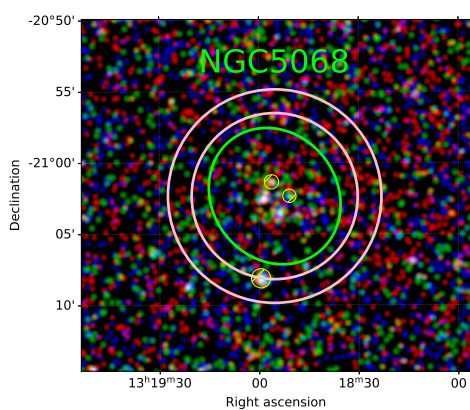
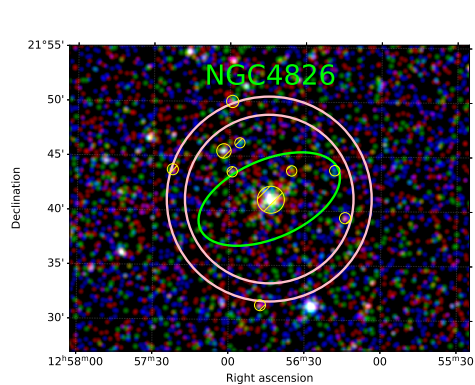
Medium SFR Galaxies

This section displays the eROSITA images of all galaxies in the $1.0 M_{\odot} \text{ yr}^{-1} > \text{SFR} \geq 0.1 M_{\odot} \text{ yr}^{-1}$ range. See Figure 5.1 for more details.



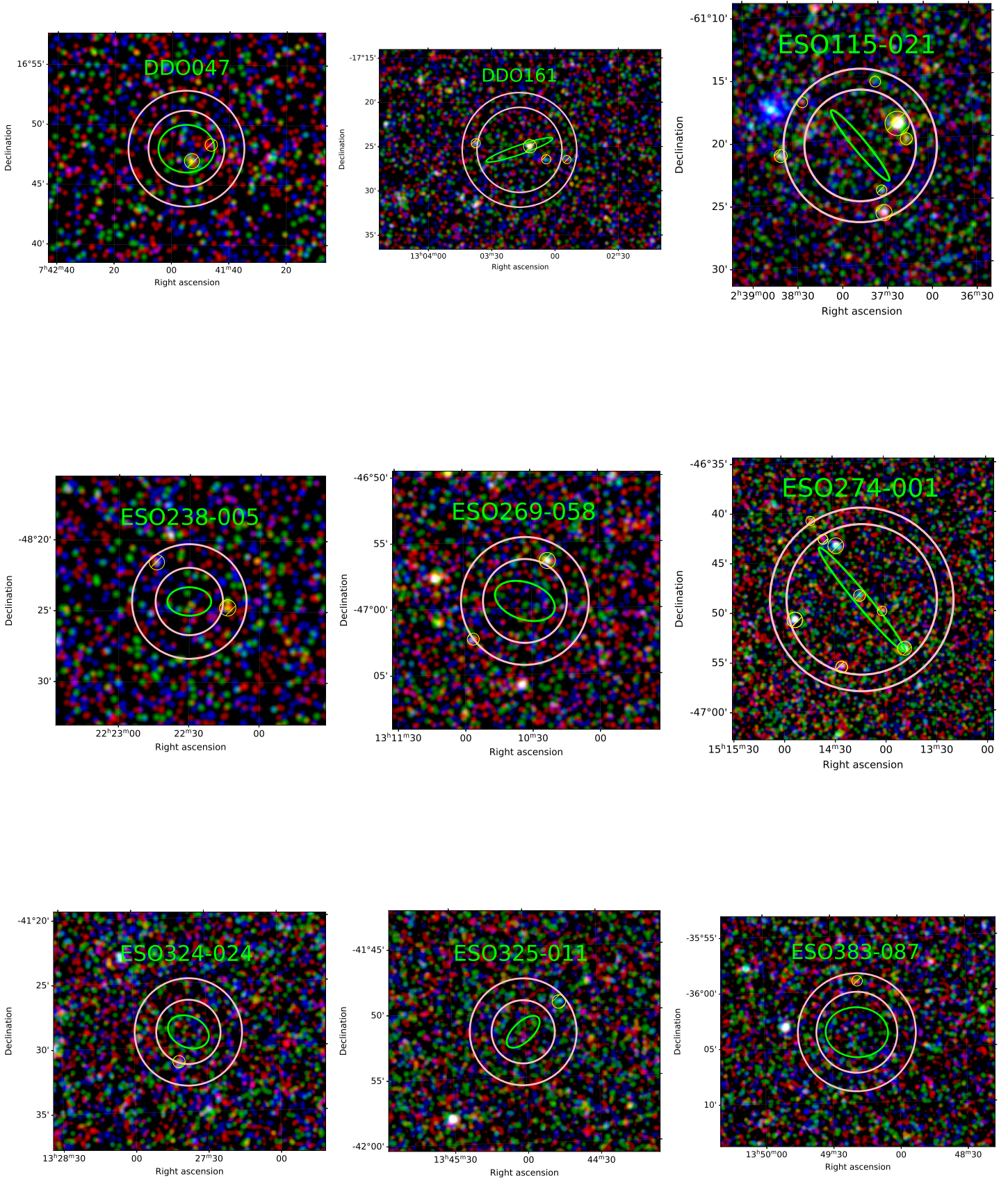


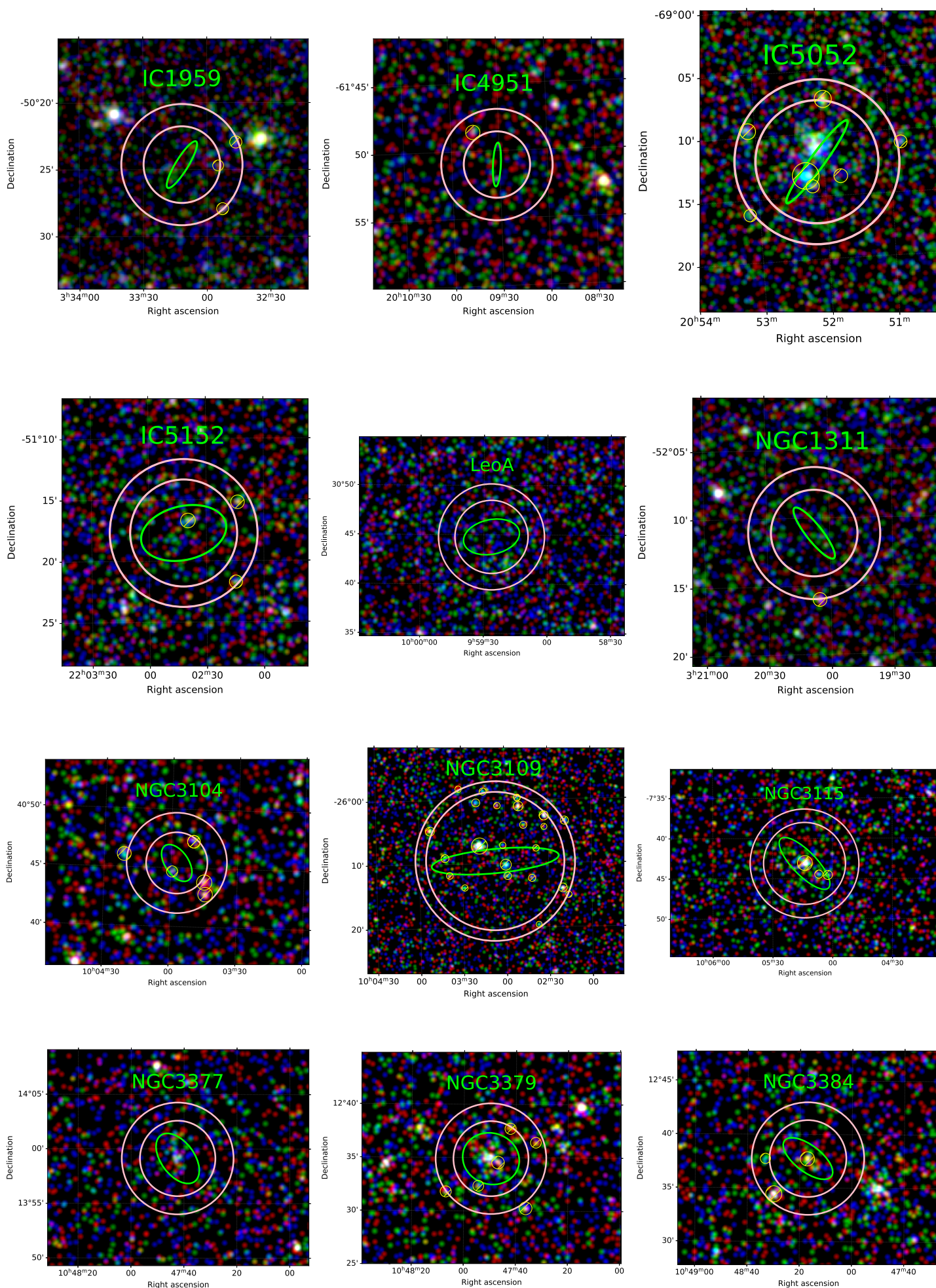


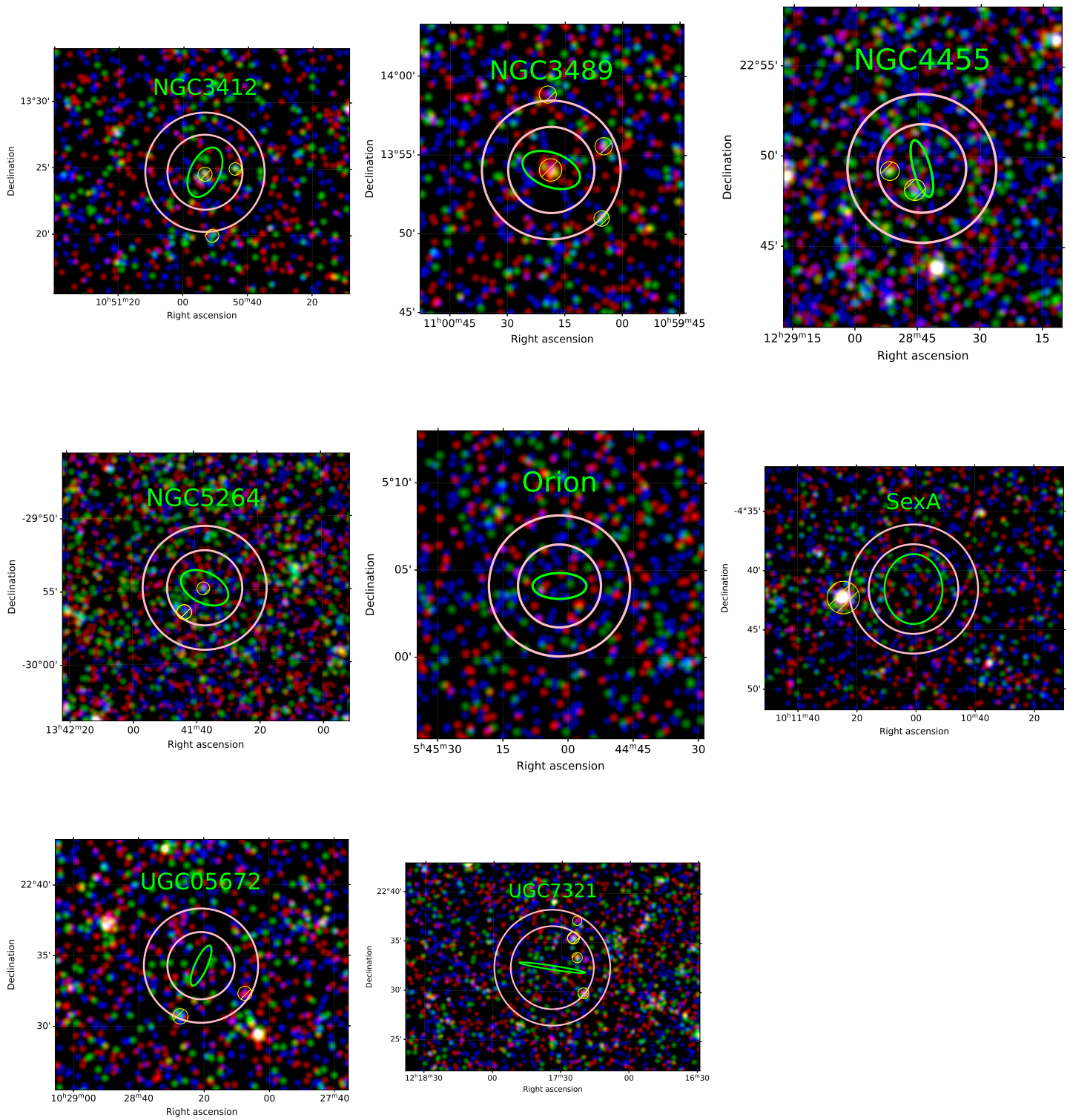


Low SFR Galaxies

This section displays the eROSITA images of all galaxies in the $\text{SFR} < 0.1 M_{\odot} \text{yr}^{-1}$ range. See Figure 5.1 for more details.







Acknowledgements

Many thanks to everyone who supported me during the work on this thesis! Without the help of my supervisor Manami Sasaki and the assistance of Jonathan Knies, Martin Meyer, Steven Hämmerich, Aafia Zainab and Phillip Weber it would not have been possible to conduct this study. Thank you Manami for providing the interesting topic, your continuous support and your patience. Thank you Jonathan for providing the background model and the image script, and thanks to Jonathan and Martin for the assistance with the PyXspec code. Thank you Steven for introducing me to the REMEIS EROPIPELINE and its applicability to my project, and thanks to Steven, Aafia and Phillip Weber for coding such a useful software for all future eROSITA science projects.

This work is based on data from eROSITA, the primary instrument aboard SRG, a joint Russian-German science mission supported by the Russian Space Agency (Roskosmos), in the interests of the Russian Academy of Sciences represented by its Space Research Institute (IKI), and the Deutsches Zentrum für Luft- und Raumfahrt (DLR). The SRG spacecraft was built by Lavochkin Association (NPOL) and its subcontractors, and is operated by NPOL with support from the Max-Planck Institute for Extraterrestrial Physics (MPE).

The development and construction of the eROSITA X-ray instrument was led by the Max Planck Institute for Extraterrestrial Physics (MPE), with contributions from the Dr. Karl Remeis-Observatory of the Friedrich-Alexander-University Erlangen Nuremberg, the University of Hamburg Observatory, the Leibniz Institute for Astrophysics Potsdam (AIP), and the Institute for Astronomy and Astrophysics of the University of Tübingen, with the support of DLR and the Max Planck Society. The Argelander Institute for Astronomy of the University of Bonn and the Ludwig-Maximilians-Universität Munich also participated in the science preparation for eROSITA.

The eROSITA data shown here were processed using the eSASS software system developed by the German eROSITA consortium.

Bibliography

- Ackermann, M. et al. (2012). In: *ApJ* 755.164.
- Aghdam, S. T. et al. (2023). In: *Proceedings of the International Astronomical Union* 373.pp. 306-309.
- Alonso-Herrero, A. et al. (2000). In: *ApJ* 530.688.
- Amblard, A. et al. (2014). In: *ApJ* 783.135.
- Anand, G. S. et al. (2021). In: *MNRAS* 501.3621.
- Arnason, R. M. et al. (2021). In: *MNRAS* 502.pp. 5455–5470.
- Avillez, M. A. de et al. (2000). In: *ApSS* 272.23.
- Baade, W. et al. (1954). In: *ApJ* 119.215.
- Bahramian, A. et al. (2023). “ Low-Mass X-ray Binaries ”. In: *Handbook of X-ray and Gamma-ray Astrophysics*.
- Barrera, N. P. et al. (2023). “Hot Gas Outflow Properties of the Starburst Galaxy NGC 4945”. In:
- Bassa, C. et al. (2004). In: *The Astrophysical Journal* 609.2.
- Beaulieu, S. F. et al. (2010). In: *AJ* 139.984.
- Beckwith, S. et al. (2005). *M51: Cosmic Whirlpool*. URL: <https://apod.nasa.gov/apod/ap050428.html> (visited on 02/01/2024).
- Bekki, K. et al. (2009). In: *MNRAS* 395.342-350.
- Bellocchi, E. et al. (2020). In: *AA* 642.A166.
- Bellochi, E. et al. (2020). In: *AA* 642.A166.
- Bergh, S. van den (1980). In: *PASP* 92.122.
- Bhattacharya, S. et al. (2017). In: *Monthly Notices of the Royal Astronomical Society* 472.3.
- Bibby, J. L. et al. (2012). In: *MNRAS* 420, Issue 4.pp. 3091-3107.
- Binder, B. et al. (2012). In: *ApJ* 758.15.
- (2017). In: *ApJ* 834.128.
- Bohlin, R. C. et al. (1983). In: *ApJ* 274.L53.
- Böker, T. et al. (1999). In: *ApJS* 124.95.
- Bolatto, A. D. et al. (2021). In: *ApJ* 923.83.
- Borkowski, K. J. et al. (2001a). In: *ApJ* 548.820-835.
- (2001b). In: *ApJ* 548, Issue 2.pp. 820-835.

- Bosma, A. et al. (2010). “Kinematics of the Barred Spiral Galaxy NGC 1291”. In: *ASP Conference Series* 421.
- Botticella, M. T. et al. (2012). In: *Memorie della Societa Astronomica Italiana Supplementi* 19.158.
- Brandt, W. N. et al. (2022). “Surveys of the Cosmic X-Ray Background”. In: *Handbook of X-ray and Gamma-ray Astrophysics*.
- Braun, R. et al. (1992). In: *Natur* 360.442.
- Bregman, J. N. et al. (1995). In: *ApJ* 441.561.
- Bresolin, F. et al. (2009). In: *ApJ* 700.309.
- Brunker, S. W. et al. (2019). In: *AJ* 157.76.
- Brunner, H. et al. (2022). In: *AA* 661.id.A1, 25 pp.
- Buta, R. J. et al. (2015). In: *ApJS* 217.32.
- Butler, D. J. et al. (2004). In: *AJ* 127.3.
- Cannon, J. M. et al. (2010). In: *AJ* 139.2170.
- Carlsten, S. G. et al. (2020). In: *ApJ* 891.144.
- Carpano, S. et al. (2005). In: *AA* 443.pp. 103-114.
- (2018a). In: *MNRAS* 476.L45.
- (2018b). In: *MNRAS* 476, Issue 1.p.L45-L49.
- Casoli, F. et al. (1993). In: *AA* 279.L41.
- Castor, J. I. et al. (1975). In: *ApJ* 195.157-174.
- Charmandaris, V. et al. (2000). In: *AA* 356.L1.
- Ciccolella, A. (2011). *Sequenza Hubble-Vaucouleurs*. URL: <https://en.wikipedia.org/wiki/File:Hubble-Vaucouleurs.png> (visited on 09/06/2021).
- Cohen, R. E. et al. (2020). In: *ApJ* 890.52.
- Coleman, M. G. et al. (2008). In: *ApJ* 685.pp. 933-946.
- Conselice, C. J. et al. (1999). In: *ApJ* 118.797-816.
- Côté, S. et al. (2009). In: *AJ* 138.1036-1061.
- Cox, D. P. et al. (2005). In: *ARAA* 43.337.
- Crosby, E. et al. (2024). In: *MNRAS* 527, Issue 3.pp.9918-9131.
- Croswell, K. (1996). *Alchemy of the Heavens*. ISBN: 9780385472142.
- Cui, W. et al. (1996). In: *ApJ* 468.102.
- Davidge, T. J. et al. (1998). In: *ApJ* 497.650.

- Diaz, J. et al. (2018). In: *MNRAS* 477.2030.
- Domgorgen, H. et al. (1997). In: *AA* 322.391-399.
- Driel, W. van et al. (1988). In: *AA* 204.39.
- DSS (1994). Association of Universities for Research in Astronomy. URL: https://archive.stsci.edu/cgi-bin/dss_form (visited on 09/26/2023).
- Dumont, A. et al. (2023). “Investigating the Dark Matter Halo of NGC 5128 using a Discrete Dynamical Model”. In: *AA*.
- Edmunds, M. G. (1990). In: *MNRAS* 246.678.
- Eibensteiner, C. et al. (2023). In: *AA* 675.id.A37.
- Elmegreen, B. G. et al. (2020). In: *ApJ* 895.71.
- Emig, K. L. et al. (2020). In: *ApJ* 903.50.
- Eskridge, P. B. et al. (2010). In: *AJ* 140, Issue 5.pp. 1137-1149.
- ESO-Images (2009). ESO/WFI (Optical); MPIfR/ESO/APEX/A.Weiss et al. (Submillimetre); NASA/CXC/CfA/R.Kraft et al. (X-ray). URL: <https://www.eso.org/public/images/eso0903a/> (visited on 02/01/2024).
- Espada, D. et al. (2019). In: *ApJ* 887.88.
- Fabbiano, G. et al. (1992). In: *ApJS* 80.531.
- Foster, A. et al. (2020). In: *AAS* 52.1.
- Friedrich, P. (2019). *German–Russian X-ray telescope takes off to study the dark universe*. URL: <https://physicsworld.com/a/german-russian-x-ray-telescope-takes-off-to-study-the-dark-universe/> (visited on 03/23/2021).
- Fulbright, J. P. (2000). In: *AJ* 120.1841.
- Gadotti, D. A. et al. (2012). In: *MNRAS* 423.877.
- Gallais, P. et al. (1991). In: *AA* 243.309.
- García-Burillo, S. et al. (2003). In: *AA* 407.p.485-502.
- Gazak, J. Z. et al. (2014). In: *ApJ* 787.142.
- Gieren, W. et al. (2005). In: *ApJ* 628.695.
- Gil, L. et al. (2023). “Unveiling the origin of the outer ring in NGC 1291”. In:
- Gilli, R. et al. (2007). In: *AA* 463.79.
- Greenhill, L. J. et al. (1997). In: *ApJ* 481.L23.
- Grimm, H. J. et al. (2002). In: *AA* 391.pp. 923–944.
- Guo, X.-L. et al. (2019). In: *ApJ* 885.117.
- Gúrpide, A. et al. (2022). In: *AA* 666.id.A100,22 pp.

-
- H. Mo, F. V. d. B. (2010). “Galaxy formation and evolution”. In: *Cambridge University Press*.
- Hada, K. et al. (2013). In: *ApJ* 779.6.
- Hamilton, A. J. S. et al. (1983). In: *ApJS* 51.115-148.
- Harris, G. L. H. et al. (2010). In: *PASA* 27.457.
- Hawarden, T. G. et al. (1993). In: *MNRAS* 260.844.
- Healy, J. et al. (2023). In: *Proceedings of the International Astronomical Union* 373.pp. 124-127.
- Heckman, T. M. (1980). In: *AA* 87.152.
- Heckman, T. M. et al. (1989). In: *AA* 87.152.
- (1990). In: *ApJS* 74.833.
- Heesen, V. et al. (2018). In: *MNRAS* 476.pp. 158-183.
- Hernandez, S. et al. (2022). In: *AJ* 164.89.
- HI4PI (2016). In: *AA* 594.A116.
- Higgins, E. R. et al. (2023). In: *MNRAS* 526.534-547.
- Hinz, J. L. et al. (2012). In: *ApJ* 756.75.
- Hogg, D. et al. (2001). In: *AJ* 121.1336.
- Hubble, E. P. (1926). In: *ApJ* 64.pp. 321-369.
- Huchtmeier, W. K. et al. (1981). In: *AAP* 100.72.
- Hunter, D. A. et al. (2004). In: *AJ* 128.2170-2205.
- Ianjamasimanana, R. et al. (2022). In: *MNRAS* 513, Issue 2.pp.2019-2038.
- Irwin, J. et al. (2002). In: *ApJ* 570.152.
- Itoh, T. et al. (2008). In: *PASJ* 60.S251.
- Iwasawa, K. et al. (1993). In: *ApJ* 409.155.
- J. H. van Gorkom, D. S. and. (1994). In: *ApJ* 423.L101.
- J.Kang et al. (2022). In: *ApJ* 939.74.
- Jacobs, B. et al. (2009). In: *AJ* 138.332.
- Jardel, J. R. et al. (2011). In: *ApJ* 739.21.
- Jiang, Y. et al. (2023). “CO-CHANGES I: IRAM 30m CO Observations of Molecular Gas in the Sombrero Galaxy”. In: *MNRAS*.
- Johnstone, C. P. et al. (2015). In: *AA* 577.A27.
- Kaisin, S. S. et al. (2019). In: *Astrophysical Bulletin* 74.pp. 1-11.

- Kalberla, P. M. W. et al. (2015). In: *AA* 578.A78.
- Kang, J. et al. (2020). In: *ApJ* 897.106.
- (2022). In: *ApJ* 939, Issue 2.74.
- Karachentsev, I. D. et al. (2007). In: *ApJ* 133.504.
- (2020). In: *AA* 643.A124.
- Karachentsev, I. D. et al. (2004). In: *AJ* 127.2031.
- Karachentsev, I. D. et al. (2013). In: *AJ* 145.101.
- Kavanagh, P. J. et al. (2020). In: *AA* 637.A12.
- Kennicutt R. C., J. (1983). In: *ApJ* 272.p. 54-67.
- Kennicutt, R. C. et al. (2008). In: *ApJS* 178.247.
- Kennicutt, R. C. et al. (2003). In: *PASP* 115.810.
- Kewley, L. J. et al. (2002). In: *AJ* 124.3135.
- Kiar, A. K. et al. (2017). In: *MNRAS* 472.p.1074-1087.
- Knapen, J. H. et al. (2010). In: *MNRAS* 408.797.
- Koda, J. et al. (2023). In: *ApJ* 949.Issue 2, id. 108.
- Kouroumpatzakis, K. et al. (2020). In: *MNRAS* 494.5967.
- Kovlakas, K. et al. (2021). In: *MNRAS* 506, Issue 2.pp.1896-1915.
- Kudritzki, R.-P. et al. (2008). In: *ApJ* 681.269-289.
- Kuntz, K. D. et al. (2003). In: *ApJ* 588.264.
- (2010). In: *ApJS* 188.46.
- (2019). In: *AA Rev.* 27.1.
- Laktionov, R. (2021). *Study of Globular Cluster Sources using eRASS1 data*. URL: <https://www.sternwarte.uni-erlangen.de/remeis-start/publications/theses/> (visited on 02/01/2024).
- Larsen, S. et al. (2011). In: *AA* 532.A147.
- Lee, J. C. et al. (2009a). In: *ApJ* 706.599-613.
- Lee, M. G. et al. (2009b). In: *ApJ* 703.pp. 692-701.
- Leroy, A. K. et al. (2008). In: *AJ* 136.2782-2845.
- (2021). In: *ApJS* 257.43.
- Leščinskaitė, A. et al. (2022). In: *AA* 660.A79.
- Lewin, W. H. G. et al. (1993). In: *Space Science Reviews* 62.3-4.
- Li, J.-T. et al. (2011). In: *ApJ* 737.41.

- Lianou, S. et al. (2012). In: *AA* 549.A47.
- Licquia, T. et al. (2013). “Improved Constraints on the Total Stellar Mass, Color, and Luminosity of the Milky Way”. In: *AAS*.
- Liu, W. et al. (2017). In: *ApJ* 834.33.
- Lundgren, A. A. et al. (2008). In: *Astronomical Society of the Pacific Conference Series* 390.144.
- Luo, B. et al. (2017). In: *ApJS* 228.2.
- Mahajan, S. et al. (2019). In: *MNRAS* 482.pp. 560-577.
- Manna, S. et al. (2023). In: *ApJ* 944.86.
- Marcelin, M. et al. (1982). In: *AA* 105.76.
- Marcelin, M. et al. (1983). In: *AAS* 51.353.
- Marchesi, S. et al. (2018). In: *ApJ* 854.49.
- Marconi, A. et al. (2000). In: *AA* 357.24.
- Marinucci, A. et al. (2012). In: *MNRAS* 423.L6.
- (2017). In: *MNRAS* 470.4039.
- Martin, C. L. et al. (2002). In: *ApJ* 574.663.
- Masters, K. L. (2005). In: *PhD thesis, Cornell Univ.*
- Matthews, L. D. et al. (2003). In: *ApJ* 593.p. 721-732.
- McQuinn, K. B. W. et al. (2016). In: *AJ* 152.144.
- Méndez-Abreu, J. et al. (2019). In: *MNRAS* 482.p. L118-122.
- Méndez-Abreu, J. et al. (2020). In: *Proceedings of the International Astronomical Union* 353.pp. 168-171.
- Merloni, A. et al. (2012). “eROSITA Science Book: Mapping the Structure of the Energetic Universe”. In: *MPE*.
- Messa, M. et al. (2021). In: *ApJ* 909, Issue 2.id.121, 26 pp.
- Meurer, G. et al. (2006). In: *ApJS* 165.307.
- Mineo, S. et al. (2012a). In: *MNRAS* 419.Issue 3.
- (2012b). In: *MNRAS* 426.Issue 3.
- (2012c). In: *MNRAS* 419, Issue 3.p. 2095-2115.
- (2014). In: *MNRAS* 437, Issue 2.pp. 1698-1707.
- Mingozzi, M. et al. (2019). In: *AA* 622.A146.
- Mirabel, I. F. et al. (1999). In: *AA* 341.667.

- Mitchell, A. (2023). In: *Physics of Stars Lecture*.
- Morganti, R. et al. (1991). In: *MNRAS* 249.91.
- Mould, J. R. et al. (2000). In: *ApJ* 536.266.
- MPE (2023a). URL: <https://erosita.mpe.mpg.de/edr/DataAnalysis/> (visited on 09/12/2023).
- (2023b). Max Planck Institute for Extraterrestrial Physics. URL: <https://erosita.mpe.mpg.de/edr/eROSITAobservations/Catalogues/> (visited on 09/26/2023).
- NASA (2009). *Messier 87*. URL: https://commons.wikimedia.org/wiki/File:Messier_87_Hubble_WikiSky.jpg (visited on 02/19/2024).
- NASA/CXC/U.Leicester/U.London/R.Soria/K.Wu (2003). URL: <https://chandra.harvard.edu/photo/2003/1154/index.html> (visited on 09/26/2023).
- NASA/ESA (2007). *Stellar nursery in the arms of NGC 1672*. URL: <https://esahubble.org/images/heic0706a/> (visited on 02/01/2024).
- NASA/IPAC (2018). *NASA/IPAC Extragalactic Database*. URL: <https://ned.ipac.caltech.edu/> (visited on 09/05/2023).
- Nicholson, R. A. et al. (1992). In: *ApJ* 387.503.
- Ochsenbein, F. et al. (2014). *The VizieR database of astronomical catalogues*. URL: <https://vizier.cds.unistra.fr/viz-bin/VizieR-3?-source=J/AJ/145/101/catalog> (visited on 09/05/2023).
- Padave, M. et al. (2021). In: *ApJ* 923.199.
- Palit, B. et al. (2023). In: *PASP* 135.054101.
- Pellegrini, S. et al. (2003). In: *ApJ* 597.175.
- Peng, E. W. et al. (2002). In: *Astron. J* 124.3144.
- Perez, I. et al. (2006). In: *AA* 454.165.
- Pérez, I. et al. (2006). In: *AA* 454.165-169.
- Perrine, C. D. et al. (1922). In: *MNRAS* 82.486.
- Peters, W. L. et al. (1994). In: *MNRAS* 269, Issue 4, pp. 1025-1034.
- Petitpas, G. R. et al. (1998). In: *ApJ* 503.219.
- Pierini, D. et al. (2002). In: *ApJ* 569, pp. 184-203.
- Ponti, G. et al. (2023). In: *AA* 674.A195.
- Predehl, P. (2014). In: *AN* 335.5.
- Predehl, P. et al. (2020). In: *Astronomy and Astrophysics* 647.A1.
- Prescott, M. K. M. et al. (2007). In: *ApJ* 668.182.
- Quillen, A. C. et al. (1993). In: *ApJ* 412.550.

- Randall, S. W. et al. (2006). In: *ApJ* 636.200.
- Read, A. M. et al. (1997). In: *MNRAS* 286.626.
- Read, A. M. et al. (2001). In: *AA* 373.pp. 473-484.
- Rhode, K. L. et al. (2004). In: *AJ* 127.302.
- Rix, H.-W. R. et al. (1995). In: *ApJ* 438.155.
- Rix, H.-W. et al. (2013). In: *Astron Astrophys Rev* 21.61.
- Roas, M. et al. (1986). In: *Proc. IAU Symp. 116, Luminous Stars and Associations in Galaxies*. p. 355.
- Rosolowsky, E. et al. (2005). In: *ApJ* 623, Issue 2.pp. 826-845.
- Rossa, J. et al. (2008). “HST/ACS Observations of Star Formation Driven Outflows in Nearby Edge-on Spiral Galaxies: Dependence of Halo Morphology on Star Formation Activity”. In:
- Rouan, D. et al. (1996). In: *AA* 315.L141.
- Roussel, H. et al. (2001). In: *AA* 372.406.
- Rubin, V. C. et al. (1994a). In: *AJ* 107.173.
- Rubin, V. C. et al. (1994b). In: *AJ* 107.p. 173.
- Ryder, S. D. (1995). In: *ApJ* 444.610.
- Ryder, S. D. et al. (1995). In: *ApJ* 109.1592.
- Ryder, S. D. et al. (1994). In: *ApJ* 430.142-162.
- Ryder, S. D. et al. (1999). In: *PASA* 16.84.
- Sacchi, A. et al. (2023). “A soft and transient ultraluminous X-ray source with 6-h modulation in the NGC 300 galaxy”. In: *AA manuscript*.
- Salomé, Q. et al. (2016). In: *AA* 586.A45.
- Sandage, A. et al. (1979). In: *AJ* 84.472.
- Sanders, J. et al. (2020). MPE. URL: <https://www.mpe.mpg.de/7461761/news20200619> (visited on 09/11/2023).
- Saniga, M. et al. (1995). In: *Astrophysics and Space Science* 225.pp. 17-20.
- Sasaki, M. et al. (2022). In: *AA* 661.A37.
- Schruba, A. et al. (2012). In: *AJ* 143.138.
- Schurch, N. J. et al. (2002). In: *MNRAS* 335.241.
- Servillat, M. et al. (2008). In: *Astronomy and Astrophysics* 480.2.
- Sil’chenko, O. K. (1996). In: *Astronomy Letters* Volume 22.pp. 108-115.
- Silk, J. et al. (2013). “Galaxy formation”. In:

- Silva-Villa, E. et al. (2012a). In: *MNRAS* 423, Issue 1.pp. 213-221.
- Silva-Villa, E. et al. (2012b). In: *AA* 537.A145.
- Silva, P. da et al. (2018). In: *ApJ* 861.83.
- Smercina, A. et al. (2023). In: *ApJL* 949, Issue 2.L37.
- Smith, R. K. et al. (2001). In: *ApJ* 556, Issue 2.pp. L91-L95.
- Snowden, S. L. et al. (1997). In: *ApJ* 485.125.
- Strickland, D. K. et al. (2004a). In: *ApJS* 151.193.
- (2004b). In: *ApJ* 606.829.
- Struve, C. et al. (2010). In: *AA* 515.A67.
- Talent, D. L. (1982). In: *ApJ* 252.594-600.
- Tan, C. (2012). “High-Mass X-ray binary: Classification, Formation, and Evolution”. In: *Journal of Physics: Conference Series*.
- Tauris, T. M. et al. (2000). In: *ApJ* 530.L93-L96.
- Tauris, T. M. et al. (2006). In: *In Lewin, Walter; van der Klis, Michiel (eds.). Compact Stellar X-ray Sources* Cambridge Astrophysics Series. 39.Chapter 16.
- Telesco, C. M. et al. (1993). In: *Apj* 414.120.
- Terlevich, R. et al. (1981). In: *MNRAS* 196.381.
- Thilker, D. A. et al. (2007). In: *ApJS* 173.538.
- Thim, F. et al. (2003). In: *ApJ* 590.256.
- Trinchieri, G. et al. (1985). In: *ApJ* 290.96.
- Tully, R. B. et al. (1982). In: *ApJ* 257.389.
- (2013). In: *AJ* 146.86.
- (2016). In: *AJ* 152.50.
- Turner, J. L. et al. (1994). In: *ApJ* 421.122.
- Tyler, K. et al. (2004). In: *ApJ* 610.213–225.
- Urquhart, R. et al. (2019). In: *MNRAS* 482.2389.
- Vargas, C. J. et al. (2017). In: *ApJ* 839.118.
- Vaucouleurs, G. de (1959). In: *Handbuch der Physik* 53.pp. 275.
- (1963). In: *ApJ* 138.934.
- (1975). In: *ApJS* 29.p. 193-218.
- Vaucouleurs, G. de et al. (1963). In: *ApJ* 137.720.

- Vaucouleurs, G. de et al. (1991). “Third Reference Catalogue of Bright Galaxies”. In: *Springer, New York*.
- Venturi, G. et al. (2017). In: *Front. Astron. Space Sci.* 4.46.
- Walsh, J. R. et al. (2012). In: *AA* 544.A70.
- Wang, J. et al. (2020). In: *MNRAS* 498.2766.
- Wang, Q. et al. (1991). In: *ApJ* 374.475.
- Wang, S. et al. (2016). In: *ApJ* 829.20.
- Watkins, A. E. et al. (2016). In: *ApJ* 826.59.
- Wilms, J. et al. (2000). In: *ApJ* 542.914.
- Winkel, B. et al. (2016). In: *AA* 585.A41.
- Yew, M. et al. (2018). In: *PASA* 35.id.e015 14 pp.
- Yi, S. K. et al. (2005). In: *ApJ* 619.L111-L114.
- Zhong, J. et al. (2011). In: *ApJ* 729.pp. 8.
- Zinn, P. et al. (2013). In: *ApJ* 774.66.
- Zurek, D. R. et al. (2009). In: *The Astrophysical Journal* 699.1113-1118.

Eigenständigkeitserklärung

Hiermit erkläre ich, dass ich die vorliegende Arbeit selbstständig verfasst und dabei keine anderen als die angegebenen Quellen und Hilfsmittel verwendet habe.

.....
Ort, Datum

.....
Roman Laktionov